CRANFIELD UNIVERSITY

CRANFIELD DEFENCE AND SECURITY

Department of Engineering and Applied Science

PhD THESIS

Academic Year 2008 - 2012

Kyle James Hutchings

High throughput combinatorial screening of Cu-Zn-Sn-S thin film libraries for the application of Cu_2ZnSnS_4 photovoltaic cells

Supervisor: Dr. David W. Lane

This thesis is submitted in partial fulfillment of the requirements for the degree of Doctor of Philosophy

Abstract

The naturally occurring mineral of Cu_2ZnSnS_4 (CZTS) is a promising alternative absorber layer for thin film based photovoltaic devices. It has the remarkable advantage that it consists of abundant, inexpensive and non-toxic elements compared to its crystallographically related and highly successful counterparts: the Cu(In,Ga)(S,Se)$_2$ (CIGSSe) and CuIn(S, Se)$_2$ (CISSe) material systems. Therefore, there is real commercial potential for reduced material costs and improved device efficiencies. A two-stage high throughput combinatorial process for the fabrication of Cu-Zn-Sn-S thin film libraries is presented, which consists of either sequentially stacking or co-depositing Cu, Sn and Zn precursor layers by DC magnetron sputtering followed by a sulphurisation process. Sputtering conditions and target-substrate geometry are developed to give compositionally graded Cu-Zn-Sn precursor layers spanning a wide spatial region around the point of stoichiometry. Conversion into Cu-Zn-Sn-S libraries is achieved by thermally evaporating a uniform layer of sulphur directly onto the metal alloy and annealing the sample at 500 °C in a furnace.

Effects of the precursor composition on the structural properties of the films prior to the incorporation of sulphur are investigated. The sulphurised libraries are then studied by Scanning electron microscopy (SEM), X-ray diffraction (XRD) and Raman spectroscopy as a function of composition, to assess the effects on morphology and phase formation. Observations of changes in lattice parameters and crystallinity are clear. The opto-electronic and electrical properties of the CZTS film libraries are measured using photoconductivity and hot point probe techniques, respectively. Changes in the band gap and conductivity type are studied as a function of atomic ratios. Based on high performing compositions, devices have been fabricated with the highest achieving cell at 1.26 %. The observations are discussed in the context of the particular compositions and synthesis conditions, and recommendations are made for further work.

Acknowledgements

It is a pleasure to thank the many people who made this thesis possible. It is difficult to overstate my gratitude to my Ph.D. supervisor, Dr. David W. Lane, who throughout the academic period had great encouragement, ideas and enthusiasm which allowed this study to nurture and move forward. It is fair to say there have been many great challenges along the way. Also, a special thanks goes to Professor Keith Rogers, for his advice and support on XRD and project work (but generally more so on motorbikes).

I am indebted to my many student colleagues over the years for providing a stimulating and enjoyable environment in which to learn and develop. I am especially grateful to Michael Sellwood for his advice, assistance and patience (and many interesting stories that always involved a Swiss guy!) when working on the vacuum coaters and accelerator; Richard Hall for his time and efforts into making the sulphurisation process possible and relatively pain-free; Dr Scilla Roncallo for useful chemistry-related advice and discussions. I would also like to thank Dr. Jonathan Painter and Dr. John Rock for patiently teaching me everything I need to know about SEM and EDS. A further thanks goes to Adrian Mustey, Dr. Sophie Beckett and Charlene Greenwood for their general technical assistance and advice.

I would like to thank my girlfriend Laura for her continual support and patience during the whole writing up period. It could not have been easy getting the brunt of it at home!

Lastly, and most importantly, I wish to thank my parents, Andy and Julie. They have taught me everything I need to know and supported me the whole way right from primary school to the completion of my PhD. It has been a long educational journey, so I'm sure they will be glad to see me outside of full time education! To them I dedicate this thesis.

This work was funded by the Engineering and Physical Sciences Research Council (EPSRC) as part of the Supergen PV-21 Consortium.

Collaborative work

All of the work carried out in this thesis was conducted by the author, with additional help from several academic partners of which I would like to thank as follows:

1. Dr. Diego Colombara and Dr. Charles Cummings for chemistry-related discussions and assistance with KCN chemical etching treatment at the department of Chemistry, Bath University.

2. Dr. Daniel Wolverson and Ian Thompson for carrying out invaluable Raman spectroscopy measurements on CZTS samples at the department of Physics, Bath University.

3. Dr. Ian Forbes, Dr. Guillaume Zoppi, Pietro Maiello, Matthew Moynihan and Philip Manley for advice and assistance on CZTS device fabrication and measurements at NPAC, Northumbria University.

List of Publications

1. K. Hutchings, D.W. Lane, K.D. Rogers, D. Wolverson, I. Thompson, D. Colombara, Influence of metallic precursor content on the structural and morphological properties of thin film Cu-Zn-Sn-S composition-spread libraries, *in preparation* for the submission to Journal of Alloys and Compounds (2012).

2. R. E. Treharne, K. Hutchings, D. A. Lamb, S. J. C. Irvine, D. W. Lane, K. Durose, Combinatorial optimization of Al-doped ZnO films for thin-film photovoltaics, J*ournal of Physics D: Applied Physics*, 2012, **45**, 33, 335102-335109(8)

3. D. Colombara, L. M. Peter, K. Rogers and K. Hutchings, Thermochemical and kinestic aspects of the sulfurization of Cu-Sb and Cu-Bi thin films, *J. Solid State Chem.*, 2012, **186**, 36–46.

4. D. Colombara, L. M. Peter, K. Hutchings, K. D. Rogers, S. Schäfer, J. T. R. Dufton, M. S. Islam, Formation of Cu_3BiS_3 thin films via sulfurization of Bi–Cu metal precursors, *Thin Solid Films*, 2012, **520**, 5165-5171.

5. A.J. Clayton, S.J.C Irvine, V. Barrioz, W.S.M. Brooks, G. Zoppi, I. Forbes, K.D. Rogers, D.W. Lane, K. Hutchings, S. Roncallo, Metal-organic chemical vapor deposition of ultra-thin photovoltaic devices using a pyrite p-i-n structure, *Thin Solid Films*, 2011, **519**, 7360-7363.

6. R.E. Treharne, A. Seymour-Pierce, K. Durose, D.W. Lane, K. Hutchings, S. Roncallo, Optical Design and Fabrication of Fully Sputtered CdTe/CdS Solar Cells, *Journal of Physics: Conference Series,* 2011, **286**, 012038.

Conference Proceedings

1. R.E. Treharne, K. Durose, K. Hutchings, D.W. Lane, D.A. Lamb, S.J.C. Irvine, Combinatorial Optimisation of Al doped ZnO films for use in thin film solar cells, *8th Photovoltaic Science Application and Technology (PVSAT-8) Conference and Exhibition,* Northumbria University, Newcastle, 2012.

2. P. Maiello, G. Zoppi, R.W. Miles, N. Pearsall, I. Forbes, K.D. Rogers, D.W. Lane, K. Hutchings, S. Roncallo, Deposition and characterisation of combinatorial libraries of sulphurised Cu-Sb metallic precursors, *8th Photovoltaic Science Application and Technology (PVSAT-8) Conference and Exhibition,* Northumbria University, Newcastle, 2012.

3. K. Hutchings, D.W. Lane, K.D. Rogers, D. Wolverson, I. Thompson, D. Colombara, Preparation and evaluation of combinatorial sputtered Cu_2ZnSnS_4 thin film libraries, *E-MRS Spring Meeting*, Nice, France, 2011.

4. K. Hutchings, D.W. Lane, K.D. Rogers, D. Wolverson, I. Thompson, D. Colombara, Preparation and evaluation of combinatorial sputtered Cu_2ZnSnS_4 thin film libraries, *7th Photovoltaic Science Application and Technology (PVSAT-7) Conference and Exhibition,* Heriot-Watt University, Edinburgh, 2011.

5. R. McCracken, K. Hutchings, D.W Lane, K.D. Rogers, Combinatorial approach for the synthesis of Cu-Sb-S and Cu-Bi-S chalcogenide systems, *7th Photovoltaic Science Application and Technology (PVSAT-7) Conference and Exhibition,* Heriot-Watt University, Edinburgh, 2011.

6. K. Hutchings, D.W. Lane, K.D. Rogers, E. Antolin, D.F. Marron, A. Marti, $Zn_{1-x}MS_x$ (M = Cr, Ni, Fe) alloy semiconductor thin films: experimentally realising intermediate band potential using a novel high throughput combinatorial approach, *7th Photovoltaic Science Application and Technology (PVSAT-7) Conference and Exhibition,* Heriot-Watt University, Edinburgh, 2011.

Contents

List of abbreviations

PV - Photovoltaics

CZTS - Cu_2ZnSnS_4

CZTSSe - $Cu_2ZnSn(S, Se)_4$

CISSe - $CuIn(S,Se)_2$

CIGSSe - $Cu(In,Ga)(S,Se)_2$

c-Si - Crystalline silicon

a-Si - Amorphous silicon

TFSC - Thin film solar cells

OPV - Organic photovoltaics

XRD - X-ray diffraction

PLD - Pulsed laser deposition

PVD - Physical vapour depositon

CVD - Chemical vapour deposition

DC - Direct current

AC - Alternating current

RF - Radio frequency

AM - Air mass coefficient

KCN - Potassium cyanide etchant

HTS - High throughput screening

TCO - Transparent conducting oxide

ITO - Indium tin oxide

FCC - Face-centred cubic

QCM - Quartz crystal monitor

SLG - Soda lime glass

RBS - Rutherford backscattering spectrometry

EDS - Energy-dispersive X-ray spectroscopy

SEM - Scanning electron microscope

GADDS - General area detector diffraction system

FWHM - Full width half maxium

CCD - Charged-couple device

PC - Photoconductivity

I-V - Current voltage curve

FF - Fill Factor

CBD - Chemical bath deposition

SSD - Solid State Detector

List of Figures

List of Tables

1 Introduction

> *"We are like tenant farmers chopping down the fence around our house for fuel, when we should be using nature's inexhaustible sources of energy - sun, wind and tide. I would put my money on the sun and solar energy. What a source of power! I hope we don't have to wait until oil and coal run out before we tackle that."* - Thomas Edison (1931)

With the world population having already approached seven billion inhabitants [1], the demand for energy on a global scale has now reached unprecedented levels with a growing belief that non-renewable fossil fuel usage is unsustainable. Utilisation of many or all of the renewable energy resources available will help alleviate these long term issues, with one of the most promising being the exploitation of solar energy. Harnessing the energy from the sun by using a range of photovoltaic (PV) cell technologies has the potential to become a major and viable carbon-free energy source, particularly when the industry approaches "grid parity": in other words, when solar electricity production costs are equal to or ideally less than the current price of purchasing electricity from the grid. Approximately 1.2×10^{17} W of solar energy is received by our planet's surface at any one point in time, which is almost 10,000 times larger than the average current annual rate of worldwide power consumption at around 15×10^{12} W [2, 3]. To put these figures into context, more energy from the sun is incident on the earth's surface in a single hour of the day than all of the energy consumed on the planet annually, so it would seem almost inconceivable for modern civilisation not to take advantage of this unconditionally free and abundant source of power.

The first chapter of this thesis begins by presenting a brief overview of the current commercialised solar technologies as well as the fundamental drawbacks in terms of materials availability and device performance. The focus then moves onto new, low-cost and sustainable thin film chalcogenide material systems with the potential capability of enhanced efficiencies and the hope of one day replacing existing and well established technologies such as silicon. One of the many interesting materials that is growing in popularity within the materials science research community

and which stimulates the motivation behind this research, is Cu_2ZnSnS_4(CZTS) - a new quarternary absorber compound that has demonstrated desirable semiconductor properties for terrestrial PV.

1.1 An overview of the PV industry

It is estimated that the average power consumption is now approaching 15 TW as previously mentioned, and based on the current trends it is expected to increase exorbitantly to approximately 30 TW over the next few decades. Of this figure, an estimated 80% of it is supplied from fossil fuels: oil (34%), coal (25%), and gas (21%). Nuclear, biomass, hydropower, wind and solar collectively account for the final 20% [4]. The use of solar power alone, therefore, still falls significantly short by some magnitude of the required "terawatt threshold" in order to meet global energy demand. In fact, solar energy contributes to less than one percent of the world's energy needs [3].

Despite the current figures, the PV industry has experienced an encouraging year of growth globally with an estimated 27.7 GW of capacity being implemented in 2011 (60% greater than the 16.6 GW installed back in 2010) bringing the worldwide total to approximately 67.4 GW [5]. This is an outstanding achievement even during times of economic and financial crisis. Since 2009, over 80% of the PV market share was dominated by the relatively well established silicon-based technologies, including multi-crystalline silicon (c-Si), mono c-Si, and amorphous silicon (a-Si). The growing material systems utilising thin films including CdTe, $CuIn(S,Se)_2$(CIS) and $Cu(In,Ga)(S,Se)_2$(CIGS) along with other niche technologies, account for the remaining 20% of the total market [6]. The likelihood of energy demand relying solely on PV is somewhat improbable, but in order to make solar a viable option combined with other renewable sources, one ultimate challenge lays ahead that needs to be resolved: the requirement for PV technology to be fully integrated in order to utilise, store and distribute solar energy in the most efficient and cost-effective manner possible on a global scale.

1.2 Thin film solar cells

Solar cell technology has gone through three main transitional phases. The first stage, which is generally termed "first generation," involved developing and using c-Si based solar cells. Even today, most solar cells rely on either mono- or multicrystalline technology as it has proved to exhibit desirable electronic and structural properties. In addition, and perhaps one of the main factors for growth, is the successful application of highly abundant silicon in the electronics industry which has led to the economies of scale acting as a driving force to the PV industry. There still remain, however, fundamental drawbacks to this technology as it is reliant on substantial amounts of material to absorb incident photon energy due to its indirect band gap. Additionally, the high cost and energy required for material extraction and the fabrication of c-Si wafers has prompted the PV industry to seek and develop inexpensive materials and processing techniques using thin film solar cell (TFSC) technology [7]. This led to a second phase known as "second generation" which initially rose to prominence back in the 1970's when the first GaAs cell was realised [8]. These technologies primarily encompass the successful absorber layers of CdTe, CIS and CIGS, and have notably demonstrated the ability to act as potential alternatives to c-Si. All of these materials have direct band gaps (as opposed to silicon which is indirect thus requiring thicker material) with high absorption coefficients between 10^4- 10^5 cm^{-1}, which is advantageous in the fact that relatively less material is required (typically 2 μm) to absorb the majority of the incident solar irradiation [9]. Both CdTe and CIGSSe yield record-achieving laboratory-based cell efficiencies of 17.3% [10] recently attained by Fist Solar in 2011 and 20.1% [11], respectively, which is close to that of c-Si cells. However, thin films still trail far behind with respect to module technology as that of commercialised c-Si modules which are now fast approaching a milestone efficiency of 25% [12, 13]. It is also worth mentioning the concept and direction of "third generation" device structures, with the overall objective of substantially reducing material extraction and synthesis costs (although this is still some way off) while crucially improving device efficiencies. These include the record-breaking multi-junction cells surpassing 40% efficiencies [14], hot carrier collection [15], intermediate band devices [16] and organics (OPV) [17].

1.3 Materials availability

Although TFSC technology is currently very encouraging, there is a growing demand for alternative materials to the well-established CdTe, CIGS and Si-variants. The abundance of indium and tellurium in the Earth's crust is estimated to be 0.05 ppm and 0.001 ppm, respectively. This is significantly lower when compared to copper, zinc and tin with respective values estimated to be 25, 71 and 5.5 ppm [18]. Furthermore, due to toxicity issues the heavy metal cadmium has experienced legislative action in some countries causing industries to restrict or completely refrain from its use [19]. Thus, there is a need to search for and identify new thin film material compounds and structures, which utilise more sustainable and non-toxic elements in conjunction to excellent device performance. It is important to realise that the latter reason is significant in reinforcing the development and commercial viability of these new technologies.

1.4 The need for new technologies and materials

With the growing need to address and meet the above criteria, extensive research has been carried out on seeking alternative thin film materials to potentially substitute current technologies. One class of multinary semiconductor compound that has ascended to prominence and offers the promise across a broad range of applications are the family of chalcogenide thin film materials. Chalcogenide compounds in their simplest form are based predominantly on a combination of metal alloys with sulphur, selenium and/or tellurium. Structural and electronic properties of these materials are particularly suitable for sustainable thin film photovoltaics and have further been used for a diverse range of technological applications such as non-volatile phase change memory devices [20]. Many promising copper-based compound candidates with *p*-type conductivity constituting of partially abundant and non-toxic elements are being studied to act as absorber layers in PV devices. Three prime examples include: $Cu_2ZnSnS(Se)_4$ (CZTS - *kesterite*) and, more recently, $CuSbS_2$ (*chalcostibite*) and Cu_3BiS_3 (*wittichenite*). CZTS material is discussed in much greater detail in the next chapter. Nair et al. first reported on the desirable properties of

p-type Cu_3BiS_3 sulphosalts [21]. It should be noted however that bismuth is not a common element with its abundance only being slightly higher than indium (0.05 ppm). A recent study by Colombara et al. investigated the complex thermochemical and kinetic aspects of the chalcogenisation of electrodeposited precursor layers Cu-Bi and Cu-Sb [22]. Photovoltaic devices incorporating $CuSbS_2$ or Cu_3BiS_3 absorber layers have not yet been fabricated to the authors knowledge but offer much promise for the future.

1.5 Overview of thesis structure

This thesis consists of ten chapters. Chapter 2 will next begin by describing the suitability of the CZTS(Se) compound for PV applications and the many ways it can be synthesised. It then focuses on giving a brief background on the underlying physics behind solar cell operation, before moving onto CZTS(Se)-based device structures and efficiencies'. Section 2.3 and 2.4 review the compositional effect on CZTS(Se) device performance and the high throughput combinatorial screening concept, respectively, which very much forms the basis behind this research. This then importantly leads onto the primary objectives of this study. The final section of the chapter then discusses the ternary precursor metal system, Cu-Zn-Sn, and which phases are expected to precipitate when deposited at low temperatures.

Chapter 3 then describes the different deposition techniques that will be used in this study, notable sputtering and thermal evaporation, before moving onto how the materials and system geometry are calibrated in order to successfully grow combinatorial CZTS libraries. Chapter 4 gives a brief overview of the characterisation techniques using during this study principally foucussing on the compositional and structural analysis of thin films which include: Energy-dispersive Spectroscopy (EDS), X-ray diffraction (XRD, Raman spectroscopy and Rutherford Backscattering spectrometry (RBS). Chapter 5 and 6 then presents compositional and structural results based on the metallic precursor libraries for both co-sputtered and stacked configurations.

Chapter's 7 and 8 predominantly address the sulphurisation process by outlining which extraneous composition-dependent phases are expected to be present

alongside the kesterite phase; the difficulties in identifying the phases with X-ray diffraction (XRD) alone, the benefits of using Raman as a complementary technique before finally moving onto the results and discussion section.

Chapter 9 discusses and analyses the opto-electronic and electrical properties associated with the CZTS libraries by using photoconductivity and the hot point probe method to obtain the band gap and conductivity-type, respectively. Based on the results in this chapter, it then proceeds onto Chapter 10 which focusses on CZTS-based device structures and efficiencies based on selected promising compositions as obtained from the photoconductivity results.

Finally, Chapter 11 concludes this thesis and further presents recommendations for future work on this promising compound material.

2 $Cu_2ZnSnS(Se)_4$ (CZTSSe) absorber thin films

In this section, a brief outline of the chemistry and history related to the CZTS(Se) material is given as well justifying why this compound is an ideal alternative absorber layer. Following subsections focus on CZTS(Se) fabrication techniques, device structures/efficiencies' and potential limitations. Finally, the influence of elemental composition is discussed and how this ultimately influences the quality and performance of the material.

2.1 Introduction and history of CZTS

Among the many In-free thin film material systems available are the naturally occurring adamantine minerals Cu_2ZnSnS_4(CZTS) and $Cu_2ZnSnSe_4$(CZTSSe). The elements used in the new cell are copper, zinc, tin, and sulphur (although $Cu_2ZnSn(S, Se)_4$ is formed with the incorporation of both sulphur and selenium). The use of all of these constituent materials bypasses the many problems inherent in the more common components of solar cells as previously mentioned in Sections 1.2 and 1.3. The use of highly-abundant, low-cost and non-toxic elements is a major attraction and a dominant driving force behind the current research into CZTS (only for Se-free compounds). It is regarded as a highly promising absorber layer and has become the subject of much interest owing to the fact it has desirable characteristics applicable to PV, with a reported optimal direct band gap in the range 1.45 - 1.6 eV and a high absorption coefficient ($> 10^4$ cm^{-1}) [23 - 25]. CZTS(Se) is akin to the chalcopyrite material CIS with half of the In(III) being substituted iso-electronically by Zn(II) and the other half with Sn(IV), which are notably sustainable replacements. CZTS(Se) is a quaternary material system and with the greater number of consitituent elements, the greater the potential for a large number of crystal structures forming which inherently makes it very difficult to synthesize the desired composition and/or structure. It is known that CZTS(Se) can form into one of two main crystallographic polymorph structures classified as stannite-type (space group $I\bar{4}2m$) and kesterite-type (space group $I\bar{4}$) [26] with a tetragonal structure. The distinguishing factors are associated with how the substitution of the Zn and

Cu metals are arranged on the structural sites of the unit cell, as illustrated in the two-dimensional schematic in Figure 1.

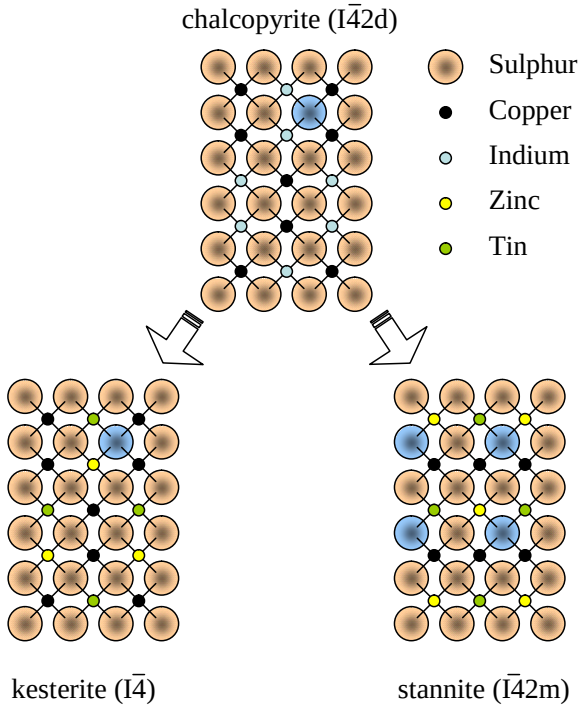

Figure 1: **A schematic representing the evolution of the kesterite and stannite-type crystal structures from the chalcopyrite structure. Derived from reference [26].**

Attempting to differentiate between these two polymorphs can prove challenging. Many studies have only used the commonly employed powder X-ray diffraction (XRD) technique, but without carrying out comprehensive single crystal structural analysis using XRD and/or Neutron diffraction [27] the structure cannot be conclusively ascertained. CZTS(Se) material has been found usually to occur in the thermodynamically stable kesterite phase as opposed to the stannite-type [26]. Therefore, in this study the CZTS(Se) family of materials is referred to as only forming into the kesterite structure.

2.2 CZTS(Se) fabrication

CZTS(Se) absorber layers and device structures can be fabricated by a wide range of techniques and can be categorised as either vacuum or non-vacuum methods. The majority of techniques involve a two-stage process where the metallic precursor

elements (Cu-Zn-Sn) are initially deposited, either sequentially or simultaneously, before undergoing an annealing process in the presence of chalcogen (S and/or Se) for the conversion into semiconductor, known as "sulphurisation" or "selenisation." In the case of both sulphur and selenium being incorporated into the compound, this is normally referred to as "sulphoselenisation." A one-step process, in some instances, is used where all materials are deposited and annealed simultaneously. Although the vacuum and non-vacuum technologies available encompass a vast range, only a few studies are reported on in the following sections which are of notable interest and represent some milestones in the area of CZTS(Se) research.

2.2.1 Vacuum deposition

Vacuum deposition mainly encompasses variants of sputtering and evaporation techniques as well as pulsed laser deposition (PLD). These are collectively known as physical vapour deposition (PVD) methods. One of the first groups to work on CZTS was Ito and Nakazawa [28] in 1988, whereby they deposited stoichiometric CZTS films and devices using atomic beam sputtering. Tanaka et al. [29] deposited elemental Cu, Zn and Sn sequentially in the presence of sulphur onto a 400 °C heated quartz substrate to form CZTS thin films within one hour using a hybrid sputtering set up. Above 450 °C, however, significant Zn losses were experienced due to its high vapour pressure. Momose et al. [30] simultaneously deposited Cu, Zn and Sn metals onto soda lime glass substrates. Notably the fully converted CZTS film involved a rapid annealing process in the presence of sulphur of only seven minutes. Some groups have investigated the deposition of sequential layering of each element as opposed to the co-deposition route. Fernandes et al. [31] fabricated CZTS precursor structures with stacking orders of Mo/Zn/Cu/Sn and Mo/Zn/Sn/Cu using DC magnetron sputtering. They found that the Mo/Zn/Sn/Cu sequence facilitated better CZTS growth and crystallinity concluding that a Cu layer on the top prevents the elemental loss of Zn and Sn during sulphurisation by acting as a "capping layer", although there was evidence of the secondary $Cu_{2-x}S$ phase present in the form of crystallites predominantly on the surface of the film. Araki et al. [32] studied various stacking orders of electron-beam evaporated metal layers with respect to

the CZTS properties and device performance. Some very interesting results came to light: the best performing solar cell consisted of a Mo/Zn/Cu/Sn stacking order yielding a device efficiency around 1.79 %. This is in relatively good agreement with Fernandes et al. [31] as mentioned previously. They found that when Cu and Zn layers were in contact larger grain sizes were induced. Furthermore, and perhaps most importantly, when Cu was used as the bottom layer i.e. in contact with Mo, formation of voids occurred between the Mo and CZTS interface and hence device performance degraded dramatically.

2.2.2 Non-vacuum deposition

Non-vacuum methods offer the possibility of reducing overall production and material costs with an increased opportunity for scalability. They are generally referred to as chemical vapour deposition (CVD) techniques, some of which have been used to fabricate CZTS including spray pyrolysis [33], sol-gel [34] and screen-printing [35]. Not surprisingly, the work by Todorov and co-workers is mentioned first, whereby a record performing CZTSSe cell ($\eta \approx 9.7$ %) was prepared by a unique solution-particle process. All constituent elements Cu, Zn, Sn and S were subjected to a "sulfoselenide" rich atmosphere at 540 °C [36]. Some groups including Guo et al. were the first to synthesise CZTS-based semiconductor nanocrystals using a hot-injection solution method in 2009. When subjected to Se vapour at 500 °C improved film quality, grain growth and device efficiencies were experienced [37]. Electrodeposited CZTS thin films were first reported by Scragg et al. [38] with varying elemental metal stacking layers deposited directly onto Mo coated glass substrates. For comparative reasons, the films were fully converted within an elemental sulphur rich atmosphere and also H_2S gas at 500 °C, with the latter improving film crystallinity.

2.3 CZTS(Se) device structures and efficiencies

This section begins by describing the underlying physics behind the operation of photovoltaic cells in general, before moving onto CZTS(Se)-based device structures and efficiencies.

2.3.1 The physics of photovoltaics

A photovoltaic device consists of an *n*-type emitter (electrons) and a *p*-type base (holes) forming a *p*-*n* junction, either of the same semiconducting material (homojunction) or of two different crystalline materials (heterojunction). The two different *p*-*n* interface configurations are described in detail below. A third *p*-*i*-*n* device configuration is also briefly introduced.

1. *p*-*n* homojunction

A homojunction is sometimes referred to as the classical model for a photovoltaic cell. This junction is formed when a semiconductor material is doped differently in two regions in order to create a *p*- and *n*-type either side both of which have equal band gaps. Crystalline silicon is a prime example where both an *n*-type (donor doped) and *p*-type (acceptor doped) create a single *p*-*n* junction interface. The position of the Fermi level, E_F, in the band gap indicates the main type of carrier. For *p*-type, the E_F has a position closer to the valence band, E_V, with an abundance of free holes. Similarly, the E_F closer to the conduction band, E_C, means there is a larger number of conduction electrons. When the *p*-type and *n*-type materials are isolated from one another, excess holes in the *p*-type and electrons in the *n*-type cannot come into equilibrium with each other and hence the respective E_F do not line up. This is illustrated in Figure 2a. Once a *p*-*n* junction is formed, under thermal equilibrium the E_F will be continuous across the structure due to high-energy free electrons diffusing from *n*- to *p*-side and low-energy holes diffusing in the opposite direction as shown in Figure 2b.

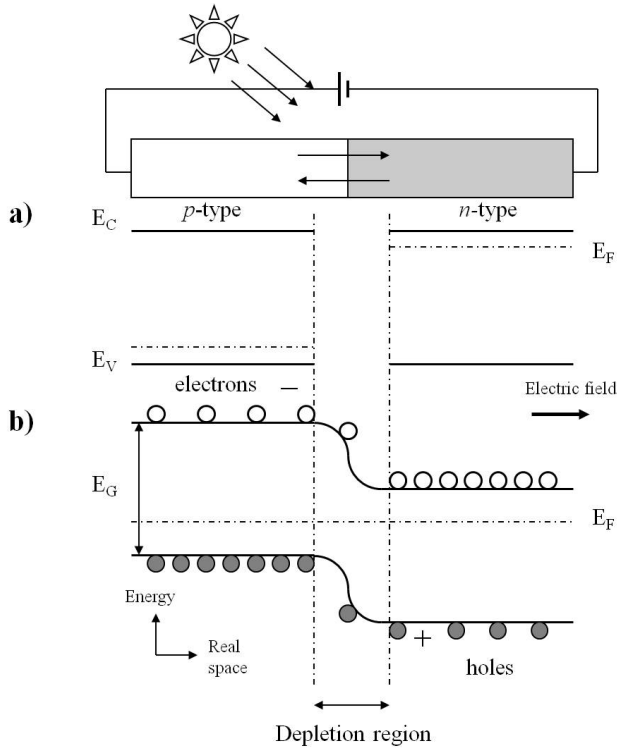

Figure 2: **Schematic of a *p*-*n* homojunction solar device: a) Two identical semiconductor materials (*p*- and *n*- type) prior to contact; and, b) Band diagram of a *p*-*n* homojunction in equilibrium.**

Under continued illumination, an incident photon will pass through the device which may be absorbed in the form of band-to-band electronic transitions between the valence, E_V, and conduction, E_C, bands thus creating electron-hole pairs on both sides of the *p*-*n* junction (in this case the single E_F is split into quasi E_F for electrons and holes) provided the electron energy is greater than the band gap $hv > E_G$ of the host semiconductor. If these generated carriers can diffuse to the depletion region before they recombine, then they are separated by the electric field. Electrons migrate across the junction to a lower energy level causing a build up of negative charge in the emitter, while holes oppose this behaviour and generate a positive charge in the base region. Thus, the potential energy at the junction is lowered and so charge (or current) is able to flow through an external load. This is essentially how the photocurrent of a solar cell is created and forms the basis for all photovoltaic devices. Formally known as the photovoltaic effect, it was not until 1954 that the first Si solar cell capable of directly converting enough sunlight into electricity to run electrical devices was fabricated [39]. It is important to note that

energy in excess of the band gap is delivered as thermal energy to the solar cell raising its temperature. Similarly, low photon energies will not induce absorption. This of course is undesirable, therefore it is necessary to match the band gap to the available visible light in order to minimise these effects by using materials with band gap energies in the narrow range of 1 - 2 eV (governed by the solar spectrum). A band gap of 1.4 - 1.5 eV is optimum for photovoltaic applications and hence the highest conversion efficiencies are expected in this region.

2. *p-n* heterojunction

Heterojunction devices require two dissimilar crystalline semiconductors with different band gaps (E_{G1} and E_{G2}) to be brought into contact as illustrated in Figure 3. Heterojunction devices have an inherent advantage over homojunction devices, which require materials that can be doped both *p*- and *n*-type. This structure is often chosen to produce cells made of thin film materials that absorb light better than silicon. An example of this type of device structure is the successful CIGSSe cell, in which the junction is formed by contacting *n*-type CdS with *p*-type CIGSSe. Normally, the most optimum design is for the absorber layer to have a band gap matched to the spectrum (1.3 - 1.5 eV) and for the upper layer to have a much larger band gap so that it does not absorb any photons or alternatively very thin so that it also absorbs as few photons as possible (the CdS often used is rather too narrow for this). However, although the operation is generally the same, the band diagram in this case is more complicated than the homojunction device as there are energy band discontinuities in the conduction band (ΔE_C) and the valence band (ΔE_V) at the junction of the two materials. This is due to the change in band gap and work functions of the two semiconductors.

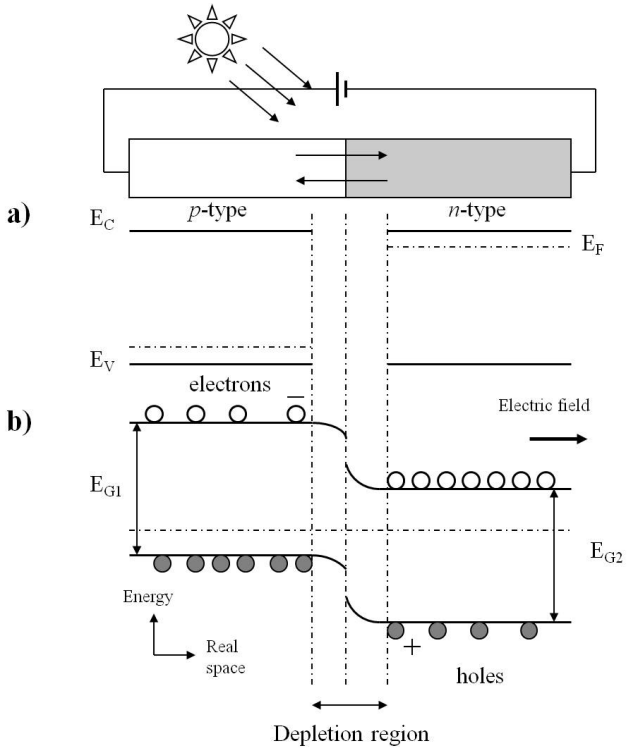

Figure 3: **Schematic of a *p*-*n* heterojunction solar device: a) Two dissimilar semiconductor materials (*p*- and *n*- type) prior to contact; and, b) Band diagram of a *p*-*n* heterojunction in equilibrium.**

For this study, the primary focus is on heterostructures which form the origin of most thin film solar devices. It is worth mentioning, however, that typical thin film solar cell structures can consist of many stacked layers each introducing multiple interfaces such as the following: a back contact, an absorber layer, a buffer layer, a window layer and a front contact in either a substrate or superstrate configuration. The reader is referred to references [40] for further details on the physics behind solid state theory and solar cells structures.

3. *p*-*i*-*n* junction

A third type of junction used typically in thin film amorphous silicon (a-Si) devices is the *p*-*i*-*n* photodiode structure which consists of three differently doped layers: an undoped (intrinsic) resistive layer located between heavily doped *p*- and *n*- type regions. This configuration sets up an electric field between the *p*- and *n*-type regions across the middle intrinsic *i*-layer region. Light generates free electrons and holes in

this intrinsic region, which are then separated by the electric field. In a CdTe cell, the device structure is similar to the a-Si cell, except the order of layers is inverted (superstrate configuration). Typically a CdTe cell has an upper p-type cadmium sulfide (CdS) layer, a middle intrinsic CdTe layer, and a bottom layer which is an n-type based material.

2.3.2 CZTS(Se) devices

Ito et al. first reported photoelectric behaviour in 1988 [28] for the CZTS/CdSnO heterostructure. Although device efficiency was not well documented, a full investigation of the p-type CZTS concluded its ideality with a direct band gap of 1.45 eV. In 1997, Friedlmeier et al. [41] fabricated CZTS solar cells using a device structure CZTS/CdS/ZnO yielding conversion efficiencies of 2.3 %. This record was soon superseded by Katagiri's group in 1999 [24], with a cell reaching power conversion efficiencies up to 2.63 %. Further investigation and optimisation of the annealing and conversion process by this group substantially improved AM 1.5 device efficiencies reaching 5.45% in 2003 [42] and then their best to date of 6.8% in 2008 [43].

With increased interest and awareness of the materials potential, many research groups have since undertaken extensive studies into the fabrication and characterisation of CZTS(Se) thin film single layers and complete device structures. There has since been a remarkable improvement in device efficiencies. This is covered in depth in references [19, 44]. Interestingly, the current record by Barkhouse et al. boasts a conversion efficiency narrowly surpassing 10% [45]. This has now overtaken the previous record held by Todorov et al. at 9.7% in 2010 [36] (although both authors' are part of the IBM group). In both cases, the device structures used a CZT(S,Se) absorber layer fabricated via a hybrid non-vacuum solution-particle approach. Also, synthesis of selenised CZTS nanocrystals via hot injection has shown total area efficiencies as high as 7.2% grown by Guo et al. [46]. It should be noted that the CZTSSe compound uses the addition of selenium to engineer the band gap closer to the PV optium range of 1.4 - 1.5 eV and as a result the highest efficiencies have ensued. It would be desirable, however, to fabricate pure sulphur CZTS active layers without inclusion of the rare element of selenium (only the sulphur compound

has highly abundant and non-toxic elements). Katagiri et al. maintain the current record of 6.8% by fabricating Se-free CZTS solar cells via an in-line sputtering and sulphurisation process [43]. Similarly, a single step thermal evaporation process by Wang et al. also yielded efficiencies up to 6.8% [47].

The current status of kesterite-type efficiencies has shown progressive improvements but still remains substantially low compared to competing thin film technologies as mentioned in section 1.2 and certainly the Shockley and Quessier theoretical limit (although this is somewhat unjust as CZTS has a band gap exceeding that of the optimum value and could never attain an efficiency over 30 % in principle) [48], thus requiring a concerted effort to fully understand and optimise material and device parameters. Interestingly, these studies have all targeted the same stoichiometric ratios and notably demonstrated that the best performing CZTS(Se)-based devices consist of Zn-rich and Cu-poor compositions, as has been well documented within the literature, irrespective of which fabrication route is pursued. The optimum compositions for the Se-free compounds were estimated to be at or close to Zn/Sn $\approx$ 1.25, Cu/(Zn+Sn) $\approx$ 0.85 and S/metal $\approx$ 1.1 [43]. The greatest challenge remains in precisely controlling the desired stoichiometry of precursor elements during the sulphurisation process for the complete conversion of mono-phase kesterite CZTS(Se). Incomplete conversion or elemental change/loss during sulphurisation, as will be later explained in greater detail, will almost certainly induce the decomposition of the pure CZTS(Se) phase and lead to the formation of detrimental binary and/or ternary metallic-chalcogen phases. A greater understanding is required of which compositions are necessary to fabricate high performing absorber material that in turn will facilitate improved device efficiencies for commercialisation. In conjunction to this, suitably refined low-cost and scalable methods of implementation would be desirable. This has recently been demonstrated using an electrodeposition route where a CZTS solar cell achieving a power conversion efficiency of 7.3% was fabricated [49]. Furthermore, the idea of commercialising CZTS(Se) has started to come to fruition with the thin film producer Solar Frontier announcing collaboration with IBM to take CZTSSe development further [50].

CZTS(Se) absorber layers have the added advantage of being integrated into the

well utilised substrate configuration as used for CIS/CIGS devices. This multi-layer structure, as illustrated in Figure 4, typically starts with a glass base coated with a molybdenum (Mo) electrical back contact, a p-n junction consisting of a CZTS(Se) active absorber layer (p-type) to replace materials like CIGSSe, and a thin CdS buffer layer (n-type). A further i-ZnO/Al:ZnO window layer and top electrical (Al) contacts complete the solar cell.

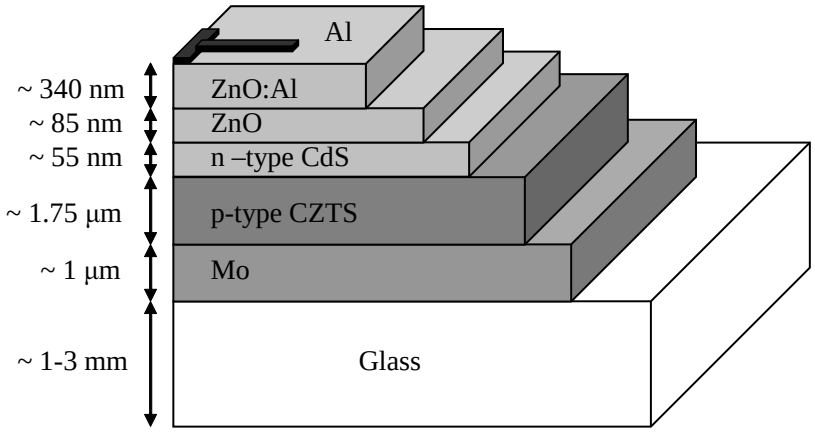

Figure 4: **Schematic cross-section of the substrate device configuration commonly used for CZTS(Se)-based solar cells. Each constituent layer is indicated with approximate thicknesses as taken from the Katagiri cell [44].**

Whether this configuration is the most suitable for CZTS(Se)-based devices has yet to be fully investigated. Many research groups are beginning to look into using different layers, thicknesses and substrates. Rajeshmon et al. have for instance, demonstrated low cell efficiencies with alternate cell structures by avoiding the usual KCN etching treatment of CZTS(Se) and further substituting the CdS buffer layer for In_2S_3 [51].

2.4 Studies on the compositional effect on the properties and formation of CZTS(Se)

The well studied thin film absorber layers of CIS and CIGS have demonstrated that the respective Cu/In and Cu/(In+Ga) composition ratios play a significant role in determining the absorber material properties suitable for solar cell fabrication and increased conversion efficiencies [52, 53]. Thus, it seems rational to investi-

gate the elemental changes when fabricating kesterite films, represented using the ratios Cu/(Zn+Sn), Zn/Sn and S/(metal), to gain an in-depth understanding of crystal growth, phase transformation, morphology and opto-electronic properties. The above ratios are widely recognised in CZTS(Se) literature and are used as a gauge of how far compositions deviate away from stoichiometry. This in turn can ultimately dictate whether a high quality and performing kesterite material can be synthesized or not.

Some recent reports investigating the compositional influence on CZTS(Se) formation and properties have been explored. Tanaka et al. co-evaporated complete CZTS thin films onto stationary soda lime glass substrates (SLG) at a temperature of 550 °C for 12 minutes, yielding films with varying Cu/(Zn+Sn) and Zn/Sn ratios ranging from 0.95 - 1.10 and 0.82 - 1.28, respectively [54]. The overall CZTS film thickness was in the region of 310 - 530 nm, which is perhaps surprisingly thin compared to most studies (notably the current world record of 10.1 % uses a thickness of up to $\approx$ 2.5 μm [45]). In summary, the crystallinity improved with enhanced grain size as the Cu/(Zn+Sn) ratio increased and interestingly, the structural properties were only affected by the change in Cu/(Zn+Sn) and not Zn/Sn. A further study by Babu et al. focussed on the effect of changing Cu/(Zn+Sn) of CZTSe films using a four-source co-evaporation set-up [55]. Films were converted in a single-step with a substrate temperature of 350 °C. Using a constant Zn/Sn ratio, the Cu/(Zn+Sn) ranged from 0.83 - 1.15. Of particular significance in this study is the realisation that phase pure and polycrystalline CZTSSe films with an optical band gap are only evident in the 0.90 - 1.10 range, with the formation of secondary phases ZnSe and $Cu_{2-x}S$ occurring at 0.85 and 1.15, respectively.

The influence of composition in non-vacuum environments was also explored by Tanaka et al. using changeable sol-gel solutions [56]. The Cu/(Zn+Sn) was varied from 0.73 - 1.00 with a constant Zn/Sn ratio held at 1.15. As the ratio decreased, large grains began to develop with a shift in band gap towards higher energies. The best performing solar cell with an efficiency of 2.03% was Cu-poor (Cu/(Zn+Sn = 0.80). Kumar et al. used spray pyrolysis to investigate the concentration effect of copper salt and thiourea on CZTS formation. Conversion occurred at a substrate

temperature of 350 °C and film ratios of Zn/Sn = 0.92, Cu/(Zn+Sn) = 0.79 and S/metal = 0.64 yielded a single phase kesterite structure with a band gap of 1.43 eV [57]. However, preventing the substantial sulphur-loss remains a challenge with this particular technique. Platzer-Bjorkman et al. have recently studied the effects of precursor sulphur content on co-sputtered CZTS [58]. They interestingly compared sulphurised precursor metals to that of sulphur-containing precursor compounds. By sulphurising metallic precursors substantial Sn-loss was observed, with the latter yielding higher quality film and improved uniformity. It was further shown that specific compositions dominated the overall device efficiencies: Zn-rich and Cu-poor were highest, while near to stoichiometric material yielded low performances.

Although these studies offer an interesting and useful insight into how chemical composition effects the overall formation and characteristics of CZTS(Se) thin films, only changes within a very narrow range are targeted. In fact, most studies generally keep the Zn/Sn ratio constant while the Cu/(Zn+Sn) value incremently deviates away from stoichiometry. Very few studies give a comprehensive overview of how CZTS(Se) formation and device performance are affected by a large elemental change over a wide spatial region. One of the main constraints is the vast number of individual samples with different stoichiometries required to undertake such a study, coupled with a large investment in time, effort and the need for advanced and automated analytical tools. As previously mentioned, Tanaka et al. [56] showed a way of keeping the substrate stationary and deliberately changing the angle of the sputter targets to obtain a graded composition in a single run. This offers a relatively simple example of the high throughput combinatorial screening approach and is introduced further in Section 2.6. A discussion is given on how careful experimental design and adequate characterisation tools can fulfill the requirements to explore properties of well known and completely new materials systems, and further how this will form the basis behind the research presented in this thesis.

2.5 Metallic precursors

There are a wide array of new and well established methods available that are capable of synthesising thin film coatings onto substrates which have become an integral part of research within the electronics, energy and optical coatings industries. The exact nature and properties of these films rely on the type, preparation and control of these techniques before and during deposition.

As outlined in Section 2.2, the fabrication of CZTS(Se) thin film samples typically relies on several key stages which can be summarised as follows:

1. Deposition of metallic precursors: typically either co-deposited or sequentially stacked at room or elevated temperatures;

2. Addition of elemental pure sulphur (and/or selenium) in either compound or gaseous form: onset of metal-chalcogen formation;

3. Conversion of metallic precursors into sulphide compounds (chalcogenisation) via thermal treatment.

Generally speaking, stages two and three normally occur simultaneously. It is, however, possible to synthesise CZTS films in a single *in-situ* process, whereby sulphur-containing metal alloys are deposited and annealed under vacuum. This approach was demonstrated by Katagiri et al. [43].

However, in this study, sulphur powder is first thermally evaporated (essentially creating a Cu-Zn-Sn-S multilayer structure at room temperature) prior to annealing the film in a furnace. This is discussed in greater detail in the subsequent chapters.

The primary focus of this section is on stage one - the deposition of precursor metals. An introduction to the background of the ternary Cu-Zn-Sn material system with its constituent binary systems (Cu-Zn, Cu-Sn and Zn-Sn) is given first, before moving onto the theory associated with the sputtering process used to deposit the precursor metals.

Gaining a clear and in-depth understanding of how the Cu-Zn-Sn ternary system behaves under specific synthesis conditions will give a useful insight into which phases will form before and after crystallisation. This will play an important role in

determining the reaction pathways for CZTS(Se) formation and ultimately influence the photoactive-quality of the film. As will be discussed in further detail in a later chapter, the metallic precursors are normally deposited in two ways: sequential stacking of discrete metal layers or co-deposition of all metal constituents. For comparative purposes, this study will investigate both fabrication routes under room temperature conditions. The stacking order of metals will be alternated in order to assess the effects on the formation and properties of CZTS(Se).

The following sections firstly address the three important constituent binary phase systems: Cu-Zn, Cu-Sn and Zn-Sn. It is important to note that interpretation of these binary alloy systems can be extremely complex especially at higher temperatures. In the interest of this investigation, however, only low temperatures will be discussed. The final section then moves onto the Cu-Zn-Sn ternary system which is of greater significance for this study.

2.5.1 Cu-Zn binary system

Cu-Zn metallic alloys are commonly used industrially as brasses, and for this reason have been extensively studied [59]. The addition of Zn to Cu results in the formation of a series of solid solutions and as a result changes the properties. Figure 5 shows the calculated phase diagram for the metallic Cu-Zn binary system. Cu (Cu) and Zn (Zn) are terminal solid solutions accompanied by a number of Cu_xZn_y intermediate phases (β, β', δ, Cu_5Zn_8(γ), and ε-$CuZn_5$) which are predominantly formed at high temperatures by peritectic, eutectic, and euctoid reactions within the composition extremes (0 - 100 at. %).

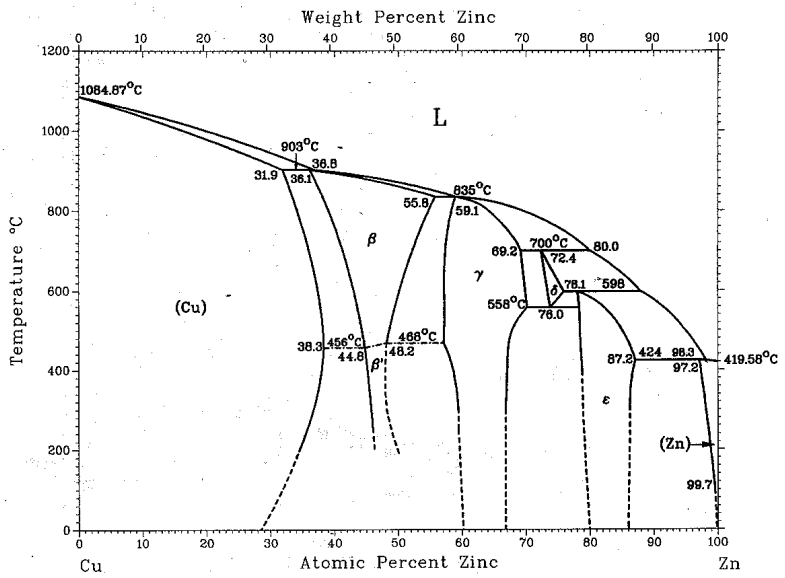

Figure 5: Calculated phase diagram for the Cu-Zn binary system [60].

At low Zn concentrations, the FCC structure relating to Cu is observed for a large temperature range up to melting point (liquid form of Cu occurs at $\approx$ 1084 °C).

2.5.2 Cu-Sn binary system

Two terminal solution phases, Cu (Cu) and Sn (βSn), occur at the edges of the binary Cu-Sn system with an additional seven intermediate phases forming by peritectic or peritectoid reactions: β, γ, $Cu_{10}Sn_3$ (ζ), $Cu_{41}Sn_{11}$ (δ), Cu_3Sn (ε), and Cu_6Sn_5 (η). The lower temperature Cu_6Sn_5 (η') also occurs which is is likely to occur at temperatures as low as room temperature. The Cu-Sn phase diagram is shown below in Figure 6 and is widely studied as bronze materials [61].

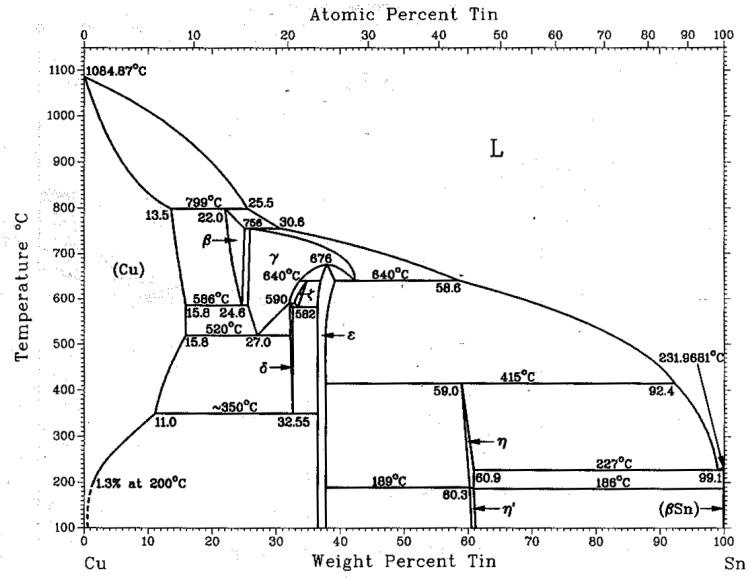

Figure 6: **Calculated phase diagram for the Cu-Sn binary system [60].**

2.5.3 Zn-Sn binary system

The phase diagram, as shown in Figure 7, of the Zn-Sn eutectic binary system is relatively simple in comparison and well established. It has a eutectic point at 198.5 °C, the temperature at which the liquid (L) form decomposes into the two terminal solid solutions, Zn (Zn) and Sn (βSn) at a composition of 91.2 wt. % Sn, as denoted by the intersection.

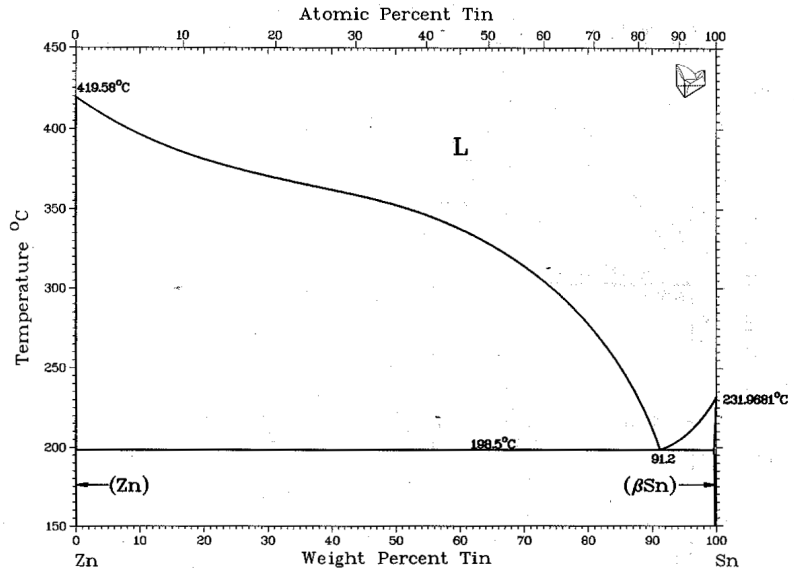

Figure 7: **Calculated phase diagram for the Zn-Sn binary system [60].**

At low temperatures, no intermediate phases precipitate and therefore no Zn_xSn_y phases would be expected to form during the sputtering of metals at room temperature for this study.

2.5.4 Cu-Zn-Sn ternary system

Ternary phase diagrams show the relationship between three components for one isothermal section i.e. the phase equilibrium is represented at one specific temperature and are normally drawn graphically as a Gibb's triangle. This essentially allows the calculation of the relative amount and composition of phases present in the system for a fixed thermodynamic state under equilibrium. There are perhaps surprisingly very few experimental studies on the Cu-Zn-Sn phase diagram. Knowledge of the phase formation across a broad range of compositions and temperatures is limited. One notable study by Chen et al in 2006 [62], focussed on the Cu-Zn-Sn phase equilibria to fully understand the Sn-Zn/Cu reactions for alloy solder applications.

An isothermal section at 250 °C was studied comprehensively with compositions covering a wide spatial region. Further studies, although in less detail, were undertaken at different temperatures and can be summarised as follows:

1. Isothermal section at 250 °C: a large range of compositions, with a liquid phase forming tie-lines with all three Cu-Zn binary compounds (CuZn, Cu_5Zn_8 and $CuZn_5$). No ternary compounds precipitate under these conditions.

2. Isothermal section at 230 °C: fewer compositions were studied, but a liquid + solid Sn two-phase region was observed with tie-lines to all Cu-Zn binaries and the higher temperature $Cu_6Sn_5(\eta)$.

3. Isothermal section at 210 °C as shown in Figure 8 (this phase diagram is also expected for lower temperatures): notably no liquid phase present with only solid elemental Sn tie-lines.

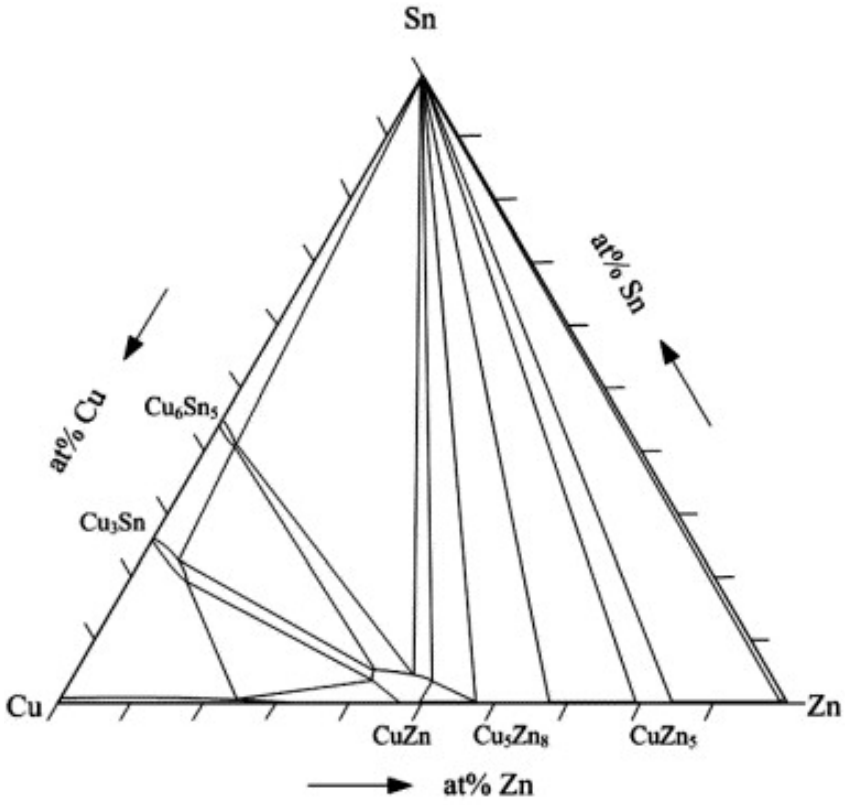

Figure 8: **Ternary Cu-Zn-Sn phase diagram for the isothermal section of 210 °C, as studied by Chen et al. [62]. Intersection of the dashed lines denotes the stoichiometric precursor ratio (Cu:Zn:Sn = 2:1:1), applicable for CZTS formation.**

If the fact that the diffusivity of Cu through Sn and the high reactivity of Zn is considered, then the formation of Cu-Zn phases show preference to Cu-Sn phases in this ternary system. It should also be mentioned that in order to achieve thermodynamic equilibrium in any system large time scales are required (especially at low temperatures such as room temperature). Therefore, non-equilibrium phase structures are often encountered and the Cu-Zn-Sn is no exception. Therefore, it must be taken into account that for the study by Chen et al. [62] only fully equilibrated bulk-form alloy material is experimented with, and not thin film compounds as in the case with this study. In that light, it is important to note that thin film effects and low deposition/anneal temperatures will play a dominant role in determining which phases are expected to precipitate.

2.6 High throughput combinatorial screening for materials discovery

2.6.1 A review of the high throughput combinatorial screening approach

This section introduces the mechanism and motivation behind deploying the high throughput screening approach for the fabrication and characterisation of material systems. The high-throughput, or otherwise referred to as the combinatorial screening approach, is becoming a favoured technique for the optimisation of known material systems as well as a useful tool to aid the discovery of new materials for a broad range of applications. Pioneered within the pharmaceutical industry for drugs screening as far back as the 1960's [63], the methodology has since progressed into many other multidisciplinary areas of materials research including catalysts [64] as well as potentially new and exciting photovoltaic materials. The approach is a useful exploratory screening tool encompassing two stages of parallel importance: firstly, the synthesis of a thin film layer, or multi-structure, is grown directly onto a substrate with extensive compositional and structural variation creating multiple samples within a single specimen known as a "library". Secondly, the deployment of a wide range of fully automated characterisation techniques to carefully investigate the structural-composition-electronic properties across the complete library is used. As a result, this tool proves to be advantageous in rapidly fabricating, identifying and comprehensively evaluating a large range of candidate material systems within a single run, as opposed to the conventional method of single-composition sample studies. High throughput screening combined with advances in technology and computation would significantly reduce the timeframe with a greater opportunity to further enhance material systems. Pioneering work by Hanak et al. [65] successfully executed the idea of high throughput experimentation in the 1970's, by co-sputtering multiple target materials simultaneously. A generic development workflow was introduced by Hanak and follows four main stages:

1. Synthesis of multi-component materials systems;

2. Non-destructive chemical composition analysis;

3. Materials properties scanned and obtained via analytical techniques;

4. Data acquisition and computer processing.

The modern approach has since evolved from the work done by Hanak which uses the integration of informatics, experimental design/modelling, simulations and scale up [66].
Generally, there are three widely recognised ways to synthesise thin film combinatorial libraries:

- Discrete or continuous sequential depositions - generally used with the aid of masking and shutter mechanisms. Studies by Xiang et al. [67], that in fact publicised the term "combinatorial," focussed on using the discrete technique to evaluate the solid state BiSrCaCuO and YBaCuO superconducting material systems.

- Composition spread co-deposition - the co-deposition of metallic elements and/or compounds with the use of masks and/or tailored target-source geometry to create lateral composition differences across a single substrate. This second approach was demonstrated by Kennedy et al. [68], where in this instance the 760 °C isothermal section of the Cr-Fe-Ni ternary phase diagram via co-deposition was mapped.

- Composition-gradient atomic epitaxy - perhaps the most complex, this technique is primarily achieved via PVD methods that intricately grow films layer-by-layer, with precisely controlled compositions and crystal structure.

2.6.2 The combinatorial application to PV

Many research groups have recently adopted the technique using one or a combination of the above methods to focus on photovoltaic and solid state electronic materials. Studies on transparent conducting oxides (TCO's) have been comprehensively investigated including the ternary Zn-Al-O and Zn-Sn-O thin film systems [69]. T. Kuykendall et al. studied the growth of the composition-related tunability of the energy band gap for single-crystalline In_xGaN_{1-x} nanowires via a CVD technique

[70]. Interest has also followed suit for device optimisation in the area of organics PV (OPV) [71]. Furthermore, Haber et al. have focused their research efforts into optimising and discovering new chalcogenide-based thin film absorber layers such as Cu_3BiS_3 [72]. Teeter et al. based at NREL, have notably begun studying the CZTS compound using combinatorial approaches by co-sputtering precursor metals before undergoing a sulphurisation/annealing process [73]. Although the approach within the PV industry remains in its infancy, it is beginning to prove to be a very useful exploratory tool particularly in the area of new oxide and chalcogenide materials. As many of these material systems contain multiple elements all dependant on one another, it is of paramount importance to be able to fine tune and optimise their properties with precision.

2.7 Primary objectives of this research

Recent studies, as mentioned in Sections 2.3 and 2.4, have shown that record device efficiencies favour a non-stoichiometric CZTS(Se) compound. More precisely, a moderately Cu-deficient and Zn-rich film is desirable. It is therefore not surprising that an in-depth knowledge is required of how compositional variation directly affects and influences the reaction pathway of the kesterite structure as well as the crystallographic, morphological and opto-electronic properties. There are relatively few in-depth studies on such influences thus stimulating the motivation for this research.

The primary objective of this study is to investigate how the compositional variation of the ternary precursor metallic system (Cu-Zn-Sn) influences the overall complex thermodynamic behaviour of Se-free CZTS and subsequently its effect on the structural, morphological and opto-electronic properties. For this study, we adopt the continuous composition spread approach as described in Section 2.6.1 to fully investigate the CZTS compound. The use of DC magnetron sputtering with a tailored system geometry has the added advantage of producing a compositionally graded library without the use of masking mechanisms. It is important to realise that this technique is relatively limited for cases of more than three or more components, and will not yield a full composition-phase diagram in a single run. In fact, it is not of interest to develop the full phase diagram but only to explore a relatively

large region around the point of stoichiometry. In short, a dual high throughput combinatorial screening approach is adopted for the fabrication and characterisation of CZTS thin film libraries. Firstly, the synthesis route involves a two-stage deposition reaction process: i) sputtering (co-deposition and sequential stacking are both investigated) of laterally graded metallic precursor libraries at room temprature, and, ii) semiconductor conversion via annealing at 500 °C in the presence of evaporated chalcogen (sulphur). Secondly, a broad range of fully automated characterisation tools are utilised to rapidly interrogate and explore material properties of mulitple compositions constrained within a single library.

3 Thin Film deposition

This chapter will outline the thin film deposition techniques used in this study. The first section will focus on the theory and mechanisms behind the sputter process used for precursor fabrication. The second part will then progress onto the calibration of each metallic element in preparation for the design of compositionally graded libraries. Finally, a brief overview on the emission characteristics associated with evaporation is given and how this knowledge can be applied to the combinatorial set up in the next chapter.

3.1 Sputtering of metal precursor layers

3.1.1 Theory and methodology of the vacuum sputtering process

Sputtering is a well established PVD vacuum coating technique offering the versatility to fabricate a wide range of desired metallic and alloy thin film material systems. The sputtering process can be divided up into four main types: DC, AC (or radio frequency, RF), reactive, and magnetron. There are, however, many variants within each category or even hybrid set-ups such as reactive magnetron. For this investigation, DC magnetron sputtering is used for the deposition of pure metals. Being such a broad subject area, focus is only given to the basic mechanisms of this type of sputtering and therefore the reader is referred to reference [74] for further information.

Magnetron sputtering is the most widely used variant of DC sputtering with several advantages over basic DC set-ups: i) deposition rates are increased due to a lower operating voltage, and ii) a stable discharge is easily attainable at lower pressures required for most industrial applications. A prerequisite for the DC-set up is the use of conducting materials such as metals or doped semiconductors. No current would be drawn if a non-conducting target is bombarded with positive ions, as surface charging builds up acting as a shield to the electrical field. Radio frequency sputtering, therefore, is normally used to deposit non-conducting materials such as oxide compounds for TCO's [75].

The DC-sputtering system setup, as illustrated in Figure 9, consists of a pair of

electrodes separated by a pre-determined distance: an anode where the substrate is located and the corresponding cathode(s) known as the target(s). Deposition of material takes place inside a high vacuum chamber, typically in the order of ≈ 1 x 10^{-6} mbar. Usually argon (Ar) inert sputtering gas is fed into the chamber with a pressure range between 0.5 - 12 mbar to facilitate the ignition of a plasma. This works when a negative potential is applied to the target. Below the target, a ring magnet is used where the electrons in its field are trapped and circulate in the vicinity of the target surface. This electron agglomeration within the gas causes a higher ionisation probability over time, thus creating a plasma at these working pressures. As a result, the Ar^+ ions are accelerated towards the target and break up or "sputter" the material free which then condenses on the substrate.

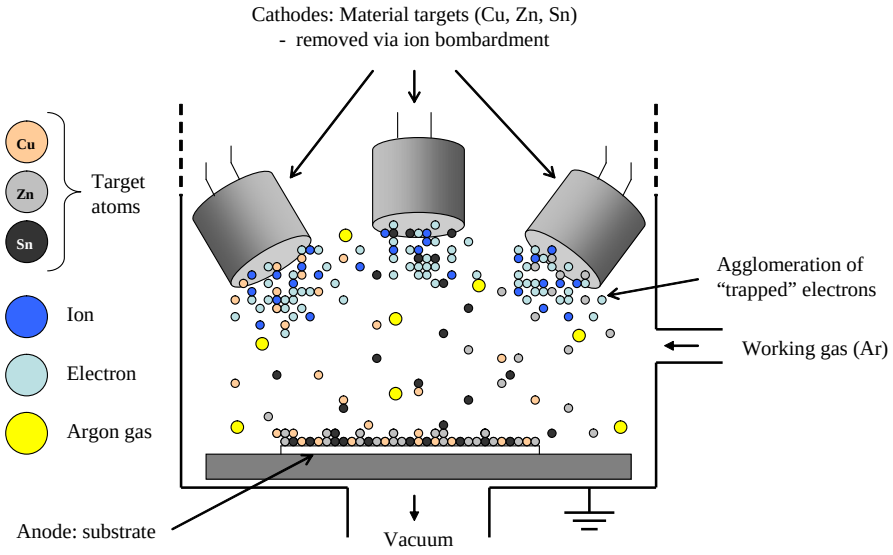

Figure 9: **Schematic illustrating a two-electrode DC magnetron sputtering set-up (three targets), as used in this study.**

3.1.2 Process and parameters selection

In general, there are two different methods of sputtering metallic alloys. The first approach uses alloy targets with the correct stoichiomety, whereas the second method deals with indirect deposition of alloys by using multiple targets of single metals. For this study, the latter approach for the synthesis of Cu-Zn-Sn ternary layers is adopted (as in Figure 9).

Although thickness variation across the substrate area is often unavoidable within

a few percent, differences in target incident angles can also cause compositional deviations. In fact, this change in elemental concentration is fundamental for this study, as the geometry will be intentionally arranged to favour compositionally non-uniform films as will be later addressed.

In practice, it is important to consider and take into account that each material has its own characteristic sputter yield which is dependent on several key factors: the target metal itself; glow discharge effects (essentially the effects of the mass of the incoming ion and the voltage through which the ion is accelerated); the applied sputtering power; sputter gas pressure; target-substrate distance and target angle of incidence with respect to the substrate normal. In addition, sputtered material is also likely to be significantly scattered by collisions with Ar gas molecules. Some of these parameters are described in greater detail as follows:

i) Target-substrate distance

Due to geometric constraints within the sputtering chamber, perpendicular target-to-substrate distances of 50 mm and 100 mm have only been evaluated for this study. Of course, reducing this distance is a simple and effective method to increase deposition rate which would be particularly desirable for saving time on a large-scale industrial level, but it is important to consider that a shorter distance will affect the thickness uniformity, film quality and further introduce unnecessary internal compressive stresses during crystal growth. Furthermore, film properties could significantly change if subjected to temperature gradients i.e. if in the vicinity of a heated substrate. However, shorter distances can have beneficial effects too: tensile stress may be reduced and film adhesion may improve due to the higher energy of arriving atoms. Generally, it can be assumed that the sputtered material leaves the target in a cosine distribution pattern and the sputter rate varies as the inverse square of the total target-substrate distance. In this instance, by halving a total distance of 100 mm to 50 mm, the material arrival rate essentially increases by a factor of four at the substrate. At a longer distance, the number of thermalising collisions increases between sputtered metal atoms and Ar gas molecules and as a consequence, the deposition behaviour no longer obeys the cosine distribution

leading to a relatively uniform and thinner layer.

For the combinatorial approach, graded compositions of each metal are required which is governed by the inclination of each target towards the centre of the substrate. It is highly important, however, to maintain a uniform film in terms of thickness when all three elements are sputtered. This is discussed in further detail in Section 3.3.

ii) Sputter gas pressure

In this study, a diverse range of operating gas pressures (denoted as P_1) from 1 x 10^{-3} mbar to 1.1 x 10^{-2} mbar have been used to assess the effects on the sputter rate of each metal. In general, deposition rates are gradually increased by lowering the sputter gas pressure. This can be accounted for principally by the fact that sputtered atoms ejected from the target will undergo fewer thermalising collisions, thus a larger proportion will deposit on the substrate. One potential downside, however, of lowering the gas pressure too much is a change in film uniformity, mainly due to a reduction in the number of thermalising collisions.

iii) Sputtering powers

Selecting the optimum power for each material is essential and needs careful consideration, not only to ensure the correct amount of material is being sputtered from the target, but also to limit any damage that may be caused to the target and system itself. The power supplied to the gun dissipates into the system, with the majority used to heat the cooling water. Given the target/interface thermal limitations, such damage can be reduced or eliminated by using an appropriate maximum power, which are normally very conservative values. In this instance, the maximum powers associated with the three target metals used in this study are: Cu (250 - 300 W), Zn (100 W) and Sn (50 W).

3.2 System and materials calibration

It is important to understand the sputtering behaviour of each metal and how they will react when deposited individually as layers before progressing onto co-deposition or stacking of all elements. The first aim was to establish the optimal processing conditions for each of the three targets - copper, zinc and tin. Calibration data was recorded with respect to different target-substrate distances, as well as varying operating chamber and working argon gas pressures (P_1 and P_{argon}, respectively, as measured using independant gauges). Furthermore, the power supplied to each target was varied incrementally up to its threshold at a fixed pressure. A quartz crystal microbalance monitor with data acquired via software (Inficon, Q-POD), was placed next to the glass substrate in an arrangement such that the sputter target is aligned perpendicular to the source.

3.2.1 Quartz crystal monitor (QCM)

In order to measure the sputter rate and film thickness at normal incidence, a QCM transducer was used in situ. The crystal monitor is positioned in the deposition chamber to intercept a fraction of the vapour flux from the target material. When a deposited mass of material (thin film) adheres to the surface of the crystal, the natural resonant frequency which is highly sensitive to density, pressure and elastic moduli is lowered as the properties of the mechanically oscillating plates are effectively altered [76]. For this study, the AT-cut crystals used composed of an alloy coated electrode (Inficon) with a resonance frequency of 6 MHz ($\pm$ 0.002 %) when unloaded, and a stability value of $\pm$ 2ppm (in the temperature range of 0 - 200 °C ideally suited to room temperature deposition). The use of an alloy composition is favoured over the commonly employed silver or gold crystals. This is predominantly due to the fact that although silver and gold both perform well with PVD techniques and have high lifetimes, there is a tendency to react to moisture, fluoride and sulphide compounds which is not ideal for this study. There are a couple of important factors to take into account when attempting to make precise thickness measurements as follows:

1) Tooling Factor

During deposition, the QCM is never normally arranged such that it occupies the same position as the substrate. Therefore, a minor offset to the incident normal means the crystal will measure a different deposition rate, albeit very small in most instances. The tooling factor corrects this geometric constraint and is normally determined by system calibration. This involves directly measuring the deposited layer either mechanically or optically, and comparing it to the thickness as monitored by the QCM. The tooling factor T_{factor} is defined as the ratio between sample thickness and the thickness as monitored by the sensor given by:

$$T_{factor} = \frac{t_{measured}}{t_{monitored}} \tag{1}$$

where $t_{measured}$ is the directly measured film thickness and $t_{monitored}$ is the thickness as measured by the QCM. A tooling factor of 1.00 signifies that both the sample and sensor receive the same thickness of film. A tooling factor $>$ 1.00 implies that the sample receives a thicker deposit than the sensor. In this case, we assume T_{factor} $\approx$ 1 due to close the proximity of the sensor to the substrate (several mm) and the appreciable magnitude of the target-substrate spacing.

2) Acoustic Impedance

The acoustic impedance of a material, often denoted as a "Z-ratio," is a signal correction factor and is calculated by taking into account the density of the material and the velocity of sound, compared to that of quartz. The accuracy of the mass load and film thickness calculation on the QCM is often limited by how well the Z-ratio and density of the material are known (typically very close to bulk values). For this setup, Z-values are selected from a materials database [77] and input via the software.

Three values are required to ensure accurate measurements of deposition rate and film thickness: the density, tooling factor and Z-ratio. These values are dependant on the material and the lifetime of the crystals. Table 1 summaries the values used in this study.

Material	Deposition technique	Density (gcm^{-3})	Z-ratio
Cu	DC sputter	8.94	0.437
Zn	DC sputter	7.14	0.514
Sn	DC sputter	7.37	0.724
S	Evaporation	2.07	2.29

Table 1: **A summary of the required QCM parameters. $T_{factor} \approx 1$ [83].**

Figure 10 shows the change in crystal frequency as a function of deposition time. When deposition begins, it is clear as expected that the value gradually decreases over time as the film deposit condenses on the crystal surface.

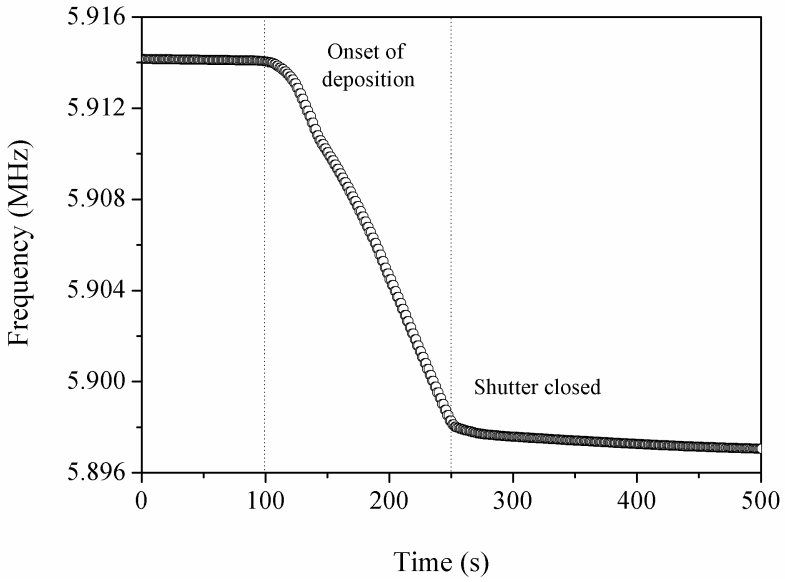

Figure 10: **QCM frequency as a function of deposition time. Dotted lines represent both the onset (shutter opened) and termination (shutter closed) of film deposition.**

Once the shutter is closed, deposition terminates and hence the crystal frequency stabilises. An important point regarding QCM set ups is the inaccuracy in film thickness measurements when muliple elements and/or compounds are deposited simultaneously. This is due to the thickness as measured by the QCM being material dependent i.e. on the Z calibration which in turn depends on the relative thicknesses deposited of each material. In order to minimise this effect, frequent crystal changes are required. Crystals should be replaced when the lifetime falls below 50% to obtain accurate and meaningful data.

3.2.2 Copper, zinc and tin deposition

The experimental emission characteristics of the Cu, Zn and Sn sputter targets are shown in Figures 11, 12 and 13, respectively. Measurements are taken from two fixed target-substrate distances at 50 mm and 100 mm. All figures show the strong linear correlation between sputter power, P, and the deposition rate, R, for both distances. As expected the rate is increased near four-fold when the target-substrate spacing is halved. Furthermore, as P_1 decreases higher sputter rates can be observed. This also holds true for low P_{argon} values. The maximum sputter powers are set to 250 W (Cu), 100 W (Zn) and 50 W (Sn).

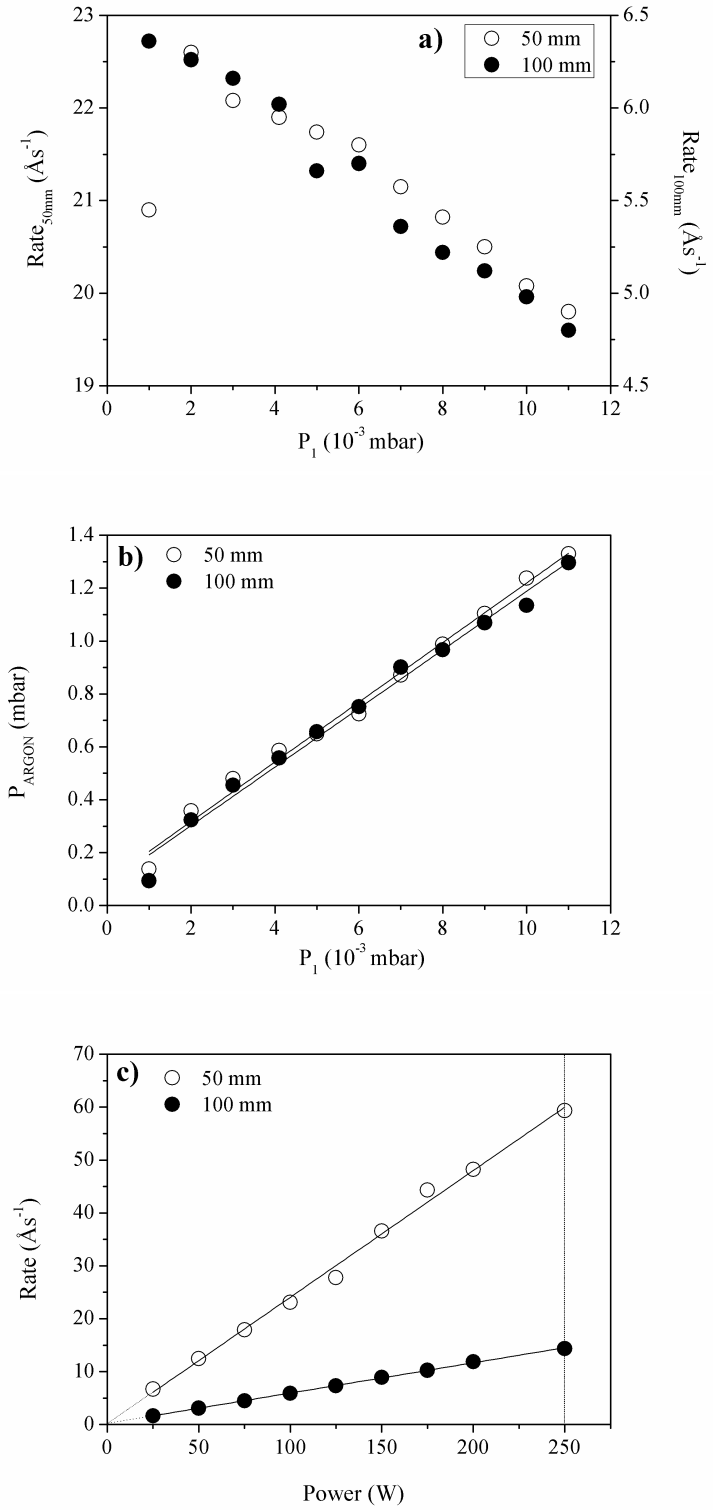

Figure 11: **Calibration data for the Cu sputter target: a) operating chamber pressure P_1 against sputter rate; b) correlation between operating pressure P_1 and argon working gas P_{argon}; and, c) Sputter power, P versus sputter rate, R.**

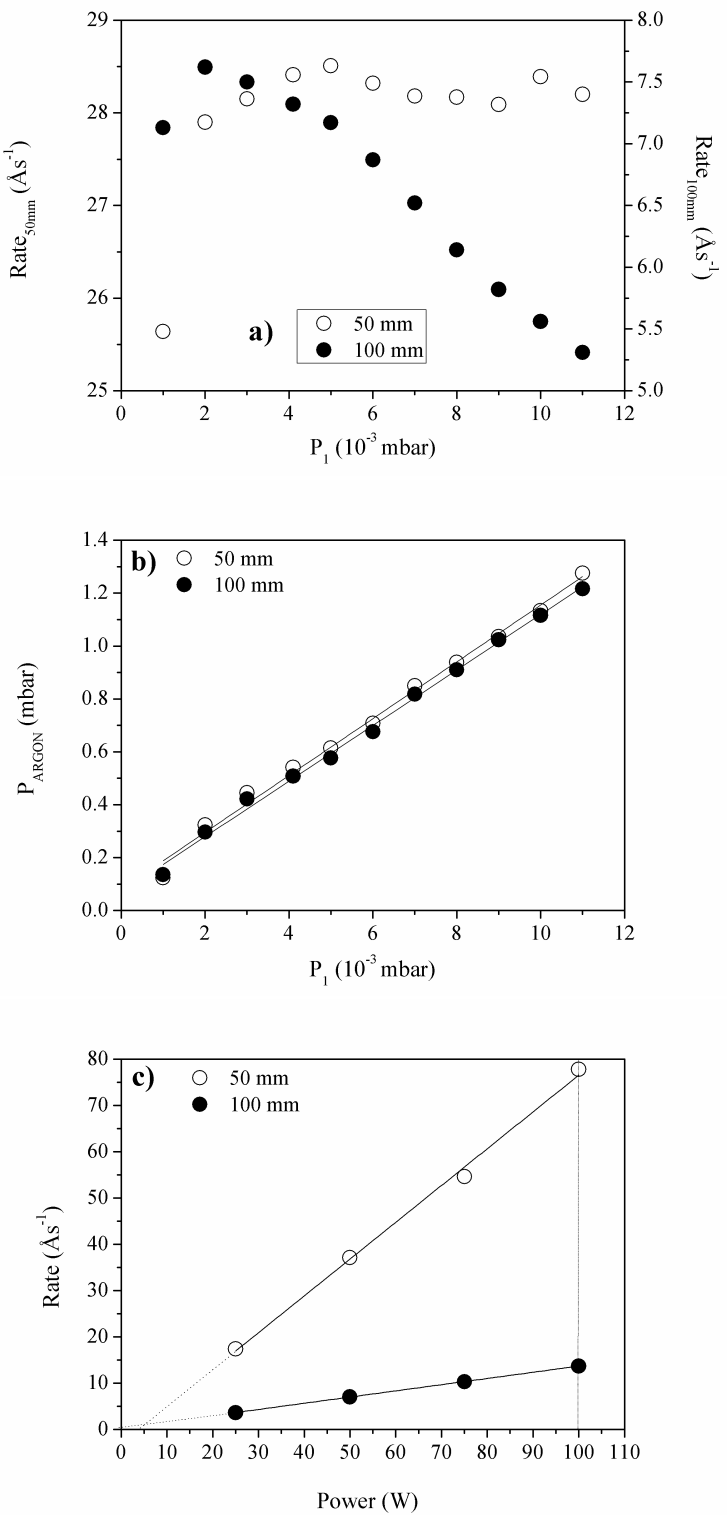

Figure 12: **Calibration data for the Zn sputter target: a) operating chamber pressure P_1 against sputter rate; b) correlation between operating pressure P_1 and argon working gas P_{argon}; and, c) Sputter power, P versus sputter rate, R.**

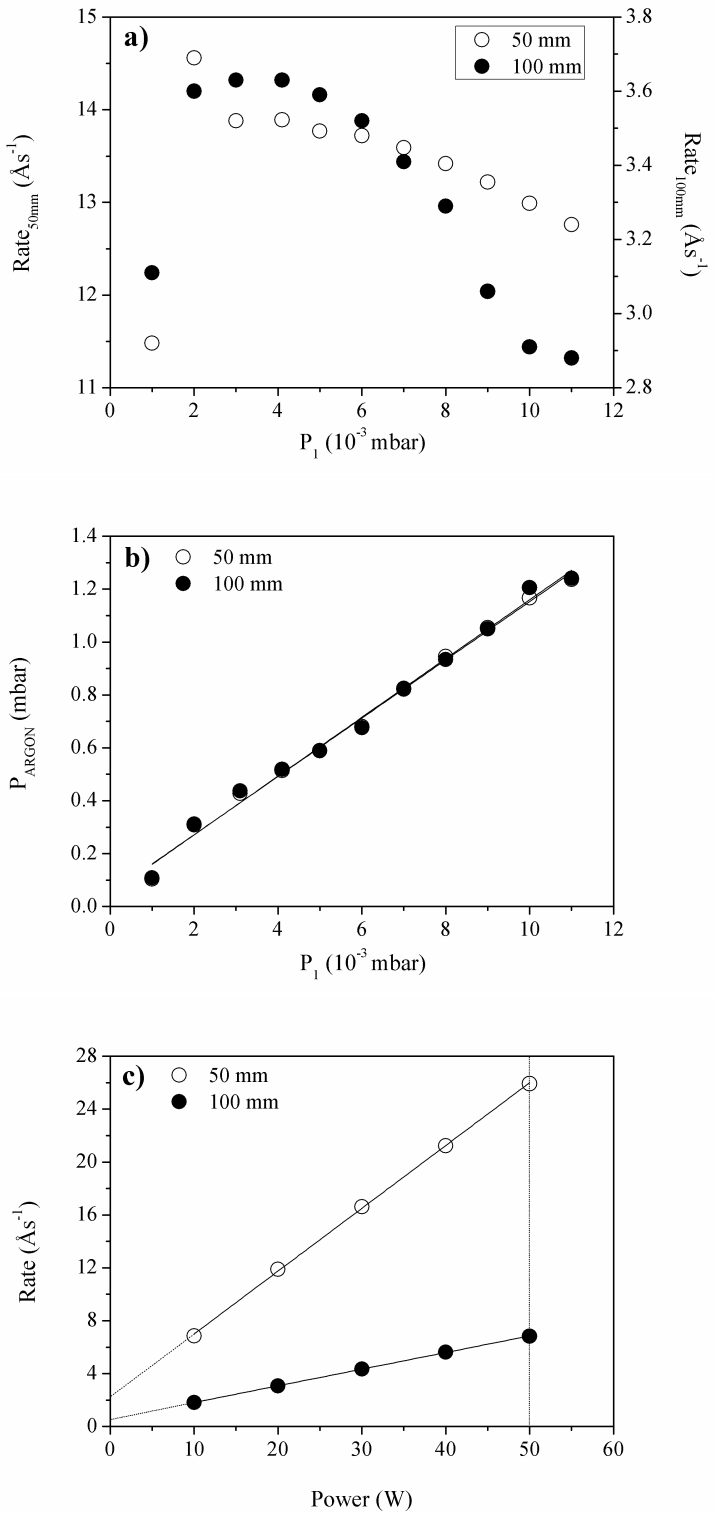

Figure 13: **Calibration data for the Sn sputter target: a) operating chamber pressure P_1 against sputter rate; b) correlation between operating pressure $P_1$and argon working gas P_{argon}; and, c) Sputter power, P versus sputter rate, R.**

The line equation derived from Figures 11c, 12c and 13c showing the relationship between sputter powers, P, and deposition rate, R, for Cu, Zn and Sn, respectively, can be given by equation (2):

$$R(x) = a(x)P(x) + b(x) \tag{2}$$

where a represents the gradient of the line and b is the y-intercept. These values are listed in Table 2. The notation x denotes the element of interest i.e. Cu, Zn or Sn.

	50 mm				100 mm			
Element	**a**	**Error**	**b**	**Error**	**a**	**Error**	**b**	**Error**
Cu	0.2395	±0.0065	0.0974	±0.0141	0.0572	±0.0006	0.2267	±0.0811
Zn	0.7947	±0.0311	-2.9200	±0.0163	0.1339	±0.0005	0.3151	±0.0322
Sn	0.4749	±0.0044	2.2510	±0.0146	0.1259	±0.0008	0.5590	±0.0278

Table 2: **Fitting parameters as calculated from the sputter power, P, vs rate, R, line graphs for distances set at 50 mm and 100 mm. The values a and b represent the gradient and intercept, respectively.**

With the acquired calibration data for each metal using a perpendicular set-up, the focus now turns to using this data in order to calculate the desired stoichiometries. Therefore, target composition values must first be considered. Based on high performing devices as described in the literature in Section 2.3, it would seem sensible to aim for a Zn-rich and Cu-poor stoichiometry towards the centre of the substrate. Thus, an inital calculation is made on the following near-stoichiometric ratios: Zn/Sn = 1 and Cu/(Zn+Sn) = 0.8. As this does not substantially deviate away from the stoichiometric film (Zn/Sn = 1 and Cu/(Zn+Sn) = 1), the stoichiometric region will also occur near the centre of the library. Careful attention should be paid to the fact that three elements are involved and are highly dependent on one another which adds a level of complexity to the calculation. Therefore, the sputter powers will need to be balanced accordingly. It is important to note that these initial calibration calculations are under the assumption that all targets are directed towards the substrate in a perpendicular fashion. Based on the calibration data, the pre-selected conditions for sputtering are as follows: an operating gas pressure of ≈

5 x 10^{-3} mbar and argon gas pressure close to 0.5 mbar over the two target-substrate distances of 50 mm and 100 mm.

3.3 Design of combinatorial precursor libraries

As previously mentioned, the power ratings for each target need to be balanced in order to yield a targeted film stoichiometry. This is achieved in two steps: firstly, the atomic ratio Zn/Sn is set to one (Zn/Sn = 1) and secondly the other atomic ratio Cu/(Zn+Sn) is set to 0.8 (Cu/(Zn+Sn) = 0.8). These two ratios will best describe the overall metallic concentration of the film.

Table 3 summarises the key parameters required for the following sputtering calculations used to deposit precursor metallic layers.

Element	Density, ρ [gcm^{-3}]	Atomic weight, W [gmol^{-1}]	Max. power, P (W)
Cu	8.94	63.55	250
Zn	7.14	65.38	100
Sn	7.37	118.71	50

Table 3: **Elemental parameters required for calculating sputtering ratios for the deposition of precursor metals**.

3.3.1 Zn/Sn sputter power calculation

In order for the atomic ratio of Zn/Sn to be equal to unity, the powers of both Zn and Sn need to be compensated for such that the final film composition is stoichiometric i.e. Zn:Sn = 1:1.

The molar densities, Φ (molcm^{-3}), of both Zn and Sn are initially calculated using the density, ρ, and atomic weight, W, values as listed in Table 3. These are given by the following:

$$\Phi_{Sn} = \frac{\rho_{Sn}}{W_{Sn}} \tag{3}$$

and,

$$\Phi_{Zn} = \frac{\rho_{Zn}}{W_{Zn}} \tag{4}$$

The values obtained from equations (3) and (4) are used to calculate the Zn/Sn ratio for a range of different powers given by the following formula:

$$\frac{Zn}{Sn} = \frac{[(\Phi_{Zn}(P_i(Zn)a(Zn) + b(Zn))]}{[(\Phi_{Sn}(P_i(Sn)a(Sn) + b(Sn))]} \tag{5}$$

where P_i is the selected power value for the range $0 \geq i \geq 50$. Equation (5) is calculated for a wide range of target powers up to the maximum permissible level for each target. In this case it is 50 W, governed by the maximum Sn power rating. At this stage, it is important to realise that the Zn/Sn ratio will vary significantly over a wide range of power values. Only a select few will satisfy the ration Zn/Sn = 1.

A linear relationship as derived from equation (5) between the two elements Zn and Sn is illustrated in Figure 14.

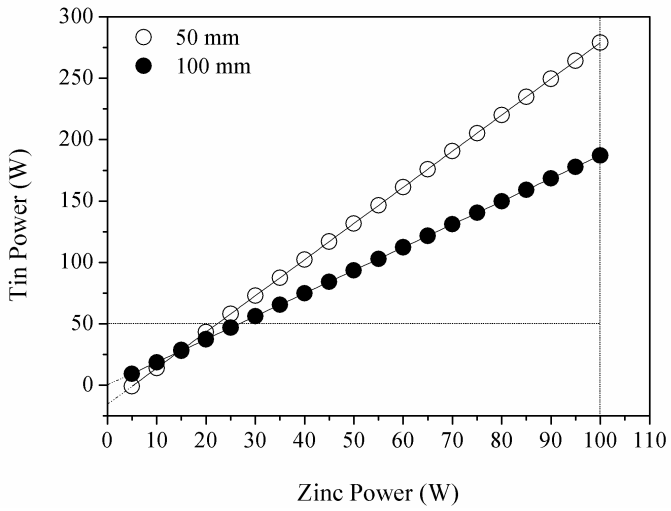

Figure 14: **Plots of sputtering powers for the ratio Zn/Sn = 1 for two distances, 50mm and 100mm. Dashed lines indicate maximum possible sputter power thresholds for each element.**

3.3.2 Cu/(Zn+Sn) sputter power calculation

Thus far, only the ratio Zn/Sn = 1 has now been considered. The more complicated three-component ratio Cu/(Zn+Sn) will now need to be accounted for in a separate calculation. The targeted ratio relates to a near-stoichiometric (marginally Cu-deficient) film: Cu/(Zn+Sn) = 0.8. As the overall power settings are governed by the maximum allowed value of Sn, the power calculation of Sn versus Cu can be considered. In this instance, the ratio can be simplified by only taking a two-component system. Arbitrary but equal values can be substituted for Zn and Sn in order to satisfy the ratio Zn/Sn = 1. Now, if the values of Zn and Sn are both equal to 1 for example, the value of Cu in the ratio Cu/(Zn+Sn) = 0.8 would be equal to 1.6. Thus, by rearranging this equation such that Cu/Sn = 1.6, the ratio Cu/Sn is calculated for a range of different powers as follows in equation (6):

$$\frac{Cu}{Sn} = \frac{[(\Phi_{Cu}(P_i(Cu)a(Cu) + b(Cu))]}{[(\Phi_{Sn}(P_i(Sn)a(Sn) + b(Sn))]} \tag{6}$$

where P_i is the selected power value for the range $0 \geq i \geq 50$ as before. The linear relationship of sputtering powers for the two elements is illustrated in Figure 15.

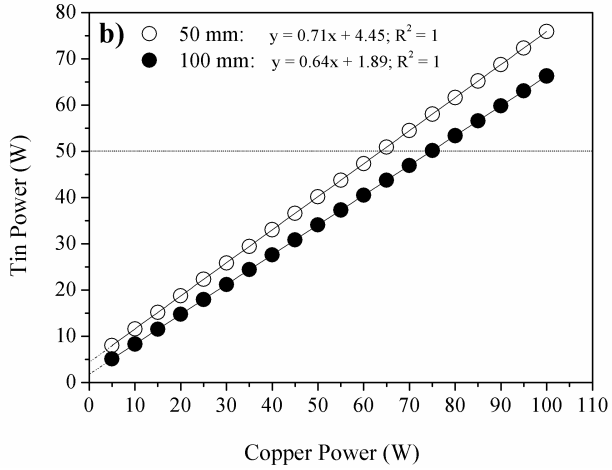

Figure 15: **Plots of sputter powers for the ratio Cu/Sn = 1.6 for two distances, 50mm and 100mm. Dashed lines indicate maximum sputter power thresholds for each element.**

3.4 Thermal evaporation

In this study, CZTS films are grown by sulphurising metal alloy layers. This is achieved by initially evaporating a thin sulphur layer onto the alloy followed by heat treatment. This section introduces the phenomena of thermal evaporation, and although sulphurisation is not discussed until Chapters 6 and 7, it is worth mentioning how the technique is affected by changes in emission angles and target-substrate distances and ultimately what effect this can have on thickness and compositional uniformity.

The process of evaporation in its simplest form consists of the vaporisation (or sublimation) and condensation of a specific element or compound onto a substrate under high vacuum. Figure 16 illustrates the assembly used for evaporating sulphur in this study.

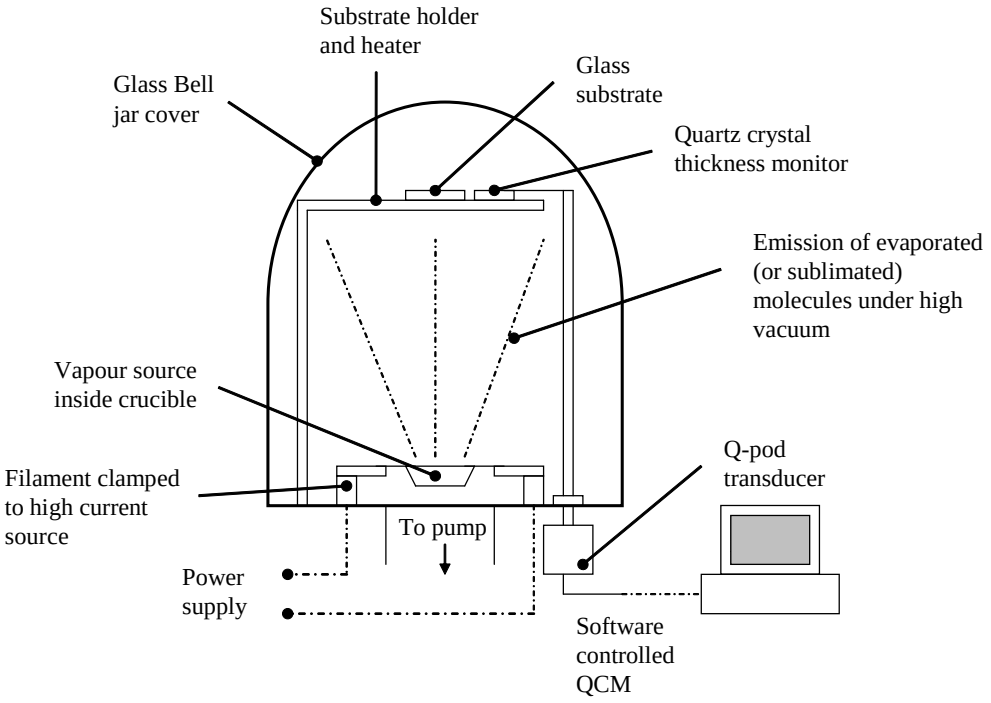

Figure 16: **Experimental set-up of the thermal evaporation system used to deposit uniform layers of sulphur.**

Evaporation from a point source is the simplest scenario to understand the process. In this instance, particles are evaporated from an infinitesimally sized spherical source, (dA_e), with a defined surface area, A_e [74]. Assuming that the evaporation

rate of the mass material, Π_e, is uniform, the total evaporated mass, M, over time, t, is given by the double integral:

$$M = \int_0^t \int_{A_e} \Pi_e dA_e dt \tag{7}$$

Of course only a small fraction of the mass will directly fall onto the substrate, dM_{sub}, with an area of dA_{sub}. The following relationship can then derived as shown in equation (8):

$$\frac{dM_{sub}}{dA_{sub}} = \frac{M \cos\theta}{4\pi r^2} \tag{8}$$

where θ is the angle between the point source and the substrate normal and r denotes the radius of the sphere. The deposition is governed by the orientation of the substrate and the inverse square law of the target-substrate distance, h. Substrates aligned in a fashion that is tangent to the spherical surface surrounding the point source at any point would theoretically receive a uniform coating (since $\theta = 0$ and $\cos\theta = 1$).

The second model, which perhaps best predicts practical scenarios more accurately, is the analogy of a surface or Knudsen effusion cell acting as an evaporation source (or multiple point sources as opposed to a single point source in equation (8). A very small opening upon which evaporant material exits, obeys a cosine emission law which is now dependant on two angles: the evaporant emission angle ϕ and the deposition angle θ. The mass deposited per unit area, therefore, is given by the following equation:

$$\frac{dM_{sub}}{dA_{sub}} = \frac{M \cos\phi \cos\theta}{\pi r^2} \tag{9}$$

Wide crucibles or filaments containing material in powder or pellet form can be approximated as a surface source. Equation (9) can be further corrected for the angular distribution of film thickness. A $\cos^n\phi$ evaporation law has experimentally been shown to be more realistic in many cases such that:

$$\frac{dM_{sub}}{dA_{sub}} = \frac{M(n+1)\cos^{\mathbf{n}}\phi\cos\theta}{2\pi r^{\mathbf{2}}} \tag{10}$$

where n is the number that determines the geometry and angular distribution of the vapour flux. When n is large in value, the vapour flux is highly directed.

For many thin film applications, such as optical coatings, thickness uniformity is an important parameter to be able to control reliably. In order to achieve ideal thickness uniformity, which is desirable when thermally evaporating sulphur in our case, both the source and the substrate are required to be located on the surface of a sphere with radius r. This eliminates the effect of the angle of incidence, θ. The geometry of this setup is illustrated in Figure 17.

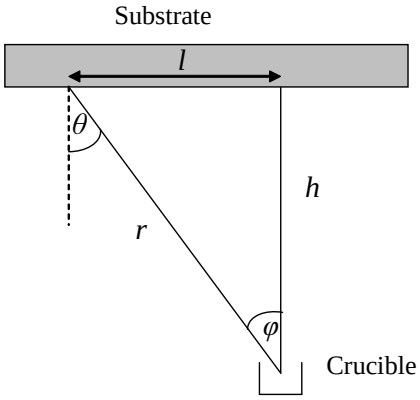

Figure 17: **Schematic illustrating the evaporation geometry (relating to equations 9 - 11). Material is evaporated from the crucible (point or surface source) onto a parallel plane substrate located above.**

In the case of a surface source, cosθ = cosϕ = h/r, and so the film thickness can be approximated to be:

$$d_{film} = \frac{M\cos\phi\cos\theta}{\pi\rho r^{\mathbf{2}}} = \frac{Mh^{\mathbf{2}}}{\pi\rho(h^{\mathbf{2}}+l^{\mathbf{2}})^{\mathbf{2}}} \tag{11}$$

where ρ is the density of the film. A further in depth explanation is given in reference [74].

3.5 Combinatorial sputter system geometry

In the previous sections, sputtered material normal to the substrate plane was only considered. A requirement for the growth of combinatorially graded Cu-Zn-Sn precursor libraries is for the target-substrate geometry to be deliberately arranged so that all targets are directed towards the centre of the substrate. It is therefore important to mention the relationship between the sputter yield as a function of incident flux angle. This section begins by outlining the theory associated with how the angle of incidence influences the sputtered material before progressing onto how this knowledge can be utilised to arrange the geometry of the sputter system in order to synthesise combinatorial precursor libraries.

3.5.1 Magnetron sputtering

Although similar characteristics can be observed for sputtering to that of evaporation, as outlined in Section 3.4, there are differences that should be accounted for. Experimental studies have shown that the variation of the sputtering yield, Y, as a function of the incident sputtering angle, θ, (defined as the angle with respect to the substrate normal) shows an inverse cosine $(\cos\theta)^{-1}$ relationship given by:

$$Y(\theta) = \frac{Y(0)}{cos\theta^{f}} \tag{12}$$

where the exponent f is calculated analytically. It can be approximated to take a value of $\frac{5}{3}$ for most applications. This was theorised by Sigmund et al. [78] in 1969 using a Boltzmann model. As θ increases from zero, the penetration depth in the target material decreases. The reason for this is that the atoms close to the surface are excited by the impact and more easily ejected (hence increasing the sputter yield). As the angle is increased further to beyond 45°, the sputter yield ultimately reaches a maximum value between 50° and 80° then starts to decrease rapidly at larger values ($> 80°$). This is due to a scattering effect, caused by the ineffective transfer of energy from the incident ions to the target surface atoms.

The model does however suffer from a number of limitations. One in particular is the fact that Equation (12) is unable to predict the subsequent drop off in the

sputter yield at elevated angles above 45°, as surface effects are not fully accounted for. Monte Carlo simulations have since been utilised to model and predict sputter yields with greater accuracy [79, 80].

Taking into account the sputter yield dependency on the angle of incidence, the arrangement of the sputtering apparatus used for this study is such that all three Torus targets (Cu, Zn and Sn) are equidistantly separated from one another and are angled at approximately 60° with respect to the centre of the substrate as illustrated in Figure 18.

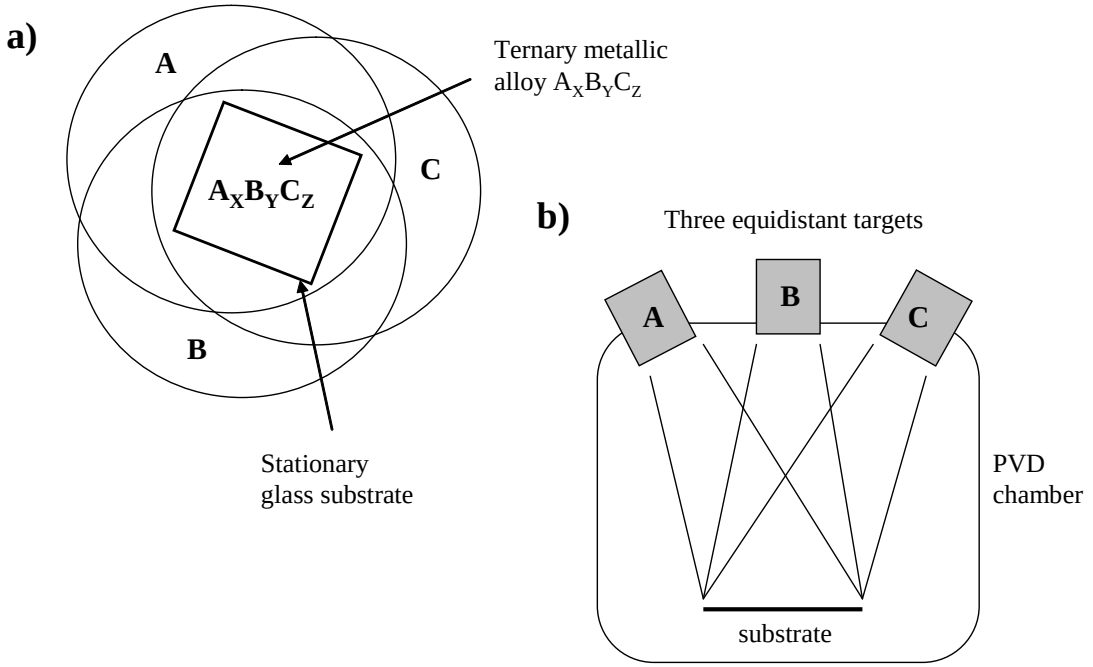

Figure 18: **Schematic of sputter chamber geometry: a) Plan view of target coverage across the glass substrate and, b) Side view of target-substrate arrangement inside the PVD chamber. Target-to-substrate distance is fixed at 100 mm.**

4 Thin film characterisation techniques

In order to fully evaluate and understand the fabricated library, it is important to interrogate each specimen with a wide range of analytical techniques ensuring each point of interest is "married up." Careful consideration was taken to design well suited mapping protocols for each technique. The raster line grid used was a 14 x 4 point matrix (points were scanned every 2 mm giving a total of 56 points per slide - 168 points per library). The follwoing section outlines and discusses the general theory of the analytical techniques used for this study to characterise both precursor and sulphurised libraries.

4.1 Energy-dispersive X-ray Spectroscopy (EDS)

4.1.1 Principles of the technique

Energy-dispersive X-ray Spectroscopy (EDS) is a commonly used non-destructive analytical technique that can obtain the chemical composition of a sample material. A focussed high-energy electron beam like the one in a scanning electron microscope (SEM) is used to strike the surface of the sample, where electrons are ejected from the constituent material atoms. The resulting electron vacancies are filled by electrons from a higher state, and an emitted X-ray (of which the energy is signature to the element from which it was released) balances the energy difference between the two electron states forming a peak(s) in the spectrum.

4.1.2 Accuracy and sensitivity

An EDS spectrum can be acquired which shows the elemental content and distribution across the sample with the x-axis representing X-ray energy (measured in eV) and the y-axis representing the number of counts per channel. The overall accuracy is governed by statistical error and generally a relative precision (defined as 2σ) of approximately $\pm$ 1 - 2% can be attained for heavier elements. Furthermore, this spectrum can be affected by the fact that many individual elements will almost certainly have multiple and/or overlapping peaks (e.g., the peaks associated with Mo La and S Ka, which is a prime example when investigating CZTSSe-based devices

deposited onto Mo coated glass substrates). This can generally be (although not always possible) minimised with longer counting times and/or an increase in the beam current. For lighter elements and/or low elemental concentrations (such as dopants or impurities), statistical errors and uncertainties in background corrections become increasingly dominant which limits the capability of distinguishing the peaks thus greater sensitivity (detection limits are typically about 0.1%, although this can be improved with some SSD detectors) is sometimes required. A further comment should also be made about the optimum choice of accelerating voltage (in keV) which is ultimately determined by the elements present in the sample. Typically, the voltage value is taken to be approximately twice that of the highest excitation energy of any element present in a compound. In this sudy, Cu and Zn have the highest excitation energies (K-lines 8.99 keV and 9.67 keV, respectively), hence the accelerating voltage should be at least 20 - 25 kV (Sn L-line excitation energy is used at 4.47 keV). It should be noted that line intensities increase with accelerating voltage, but as a result so does electron penetration causing the spatial resolution to deteriorate substantially. The reader is referred to references [81, 82] for further information on the EDS technique.

4.2 X-ray diffraction (XRD)

4.2.1 Principles of the technique

The X-ray diffraction (XRD) technique is normally used to identify the crystal phase structures that form in material systems. In brief, the XRD technique can be described as the interrogation of a material using a monochromatic X-ray beam that passes through the matter and interacts with the electrons causing the X-ray radiation to scatter. Most crystal structures can have many sets of planes pass through their atoms with each set having a specific lattice or interplanar spacing that will give rise to a characteristic angle of diffracted X-rays, provided the lattice spacing is of comparable magnitude to the wavelength of the X-rays. Depending on the orientation of these planes, the reflected rays either constructively or destructively interfere. Although these rays cancel one another out in most directions (destructive

interference), they do add constructively in a few specific directions. In this case, if the incoming wavelength is known and the angle is measured with a diffractometer, then the interplanar distance, d, can be calculated from the Bragg equation as follows:

$$n\lambda = 2dsin\theta \tag{13}$$

where θ is the incident angle, n the order and is any integer (which in this case is equal to one), and λ is the wavelength of the beam. Reference [83] gives a comprehensive overview of the XRD technique.

4.3 Raman spectroscopy

4.3.1 Principles of the technique

Raman spectroscopy is widely used to study the composition and crystal structure of solid, liquid and gaseous samples. An incident beam of radiation with a single frequency, typically a laser, is used to irradiate a material sample. The molecules or phonon's in a crystal are excited to an unstable "virtual" electronic state (as governed by the frequency of the light source) and immediately fall back to their original state by releasing a photon which is detected. When photons are scattered with negligible frequency shifts elastic Rayleigh scattering occurs (scattered photon energy is equal to that of the incoming light and as a result there is no energy change). If, on the contrary, inelastic Raman scattering occurs the scattered photons have a different energy value to that of the incoming radiation (energy shift). However, this is a weak process and the Rayleigh scattering is the most dominant.

During Raman scattering, a molecule may fall back from an excited electronic state to an energy state that is higher (Stokes) or lower (anti-Stokes) than the original state. The different vibrational modes of a molecule can therefore be identified by recognising Raman shifts in the inelastically scattered light spectrum. Strictly speaking, the peaks associated with Raman scattering should be expressed as a shift in energy with respect to the exciting radiation i.e. a change in energy but for

simplicity the literature generally expresses it simply as cm^{-1}.

In this study, however, Raman analysis on crystalline solids rather than on molecular compounds is more of interest. It is only "Raman-active" phonons that give a signal (standing wave optical phonons due to crystal vibrations and not the molecular vibrations that occur at certain bond energies as they are not "Raman-active"). For this study a tuneable laser is used. It should be noted that there is always broad-band random emission over the whole tuning range thus lasers cannot be considered as ideal monochromatic light sources. Two ways to avoid this is to either block the spontaneous emission prior to reaching the sample by passing the laser beam through a spatial filter or; to use a monochromator which acts as a filter for the laser beam before it reaches the sample (however this can cause about 50% of the laser power to dissipate). Spatial resolutions of around 10^{-6} m can be achieved, depending on the particular optical system used. References [84, 85] contains a very useful introductory chapter on the subject of Raman scattering.

4.4 Rutherford Backscattering spectrometry (RBS)

4.4.1 Principles of the technique

Rutherford Backscattering spectrometry (RBS) is a non-destructive ion scattering technique used for compositional thin film analysis and is ideal that it allows quantification without the use of reference standards. Helium ions typically in the 0.5 - 4 MeV range bombard a sample and are elastically backscattered by the nuclei of a specimen. The energy associated with the backscattered particles are a function of the mass of the sample and can provide a quantitative elemental depth profile of up to a few microns i .e. depth information is gained via the energy loss of the ions on their way through the material. Multi-elemental and/or multi-layered samples can be analysed and is well suited to measuring the absolute thickness of thin film coatings, surface and/or interfacial layers (units in atoms/cm^2); interdiffusion kinetics of thin films, and elemental composition of complex materials such as oxides and compound semiconductors. All elements from Be to U can be detected normally using a silicon solid state detector. Detection limits depend on the sample composi-

tion and are orders of magnitude better for heavy elements than for light elements such as oxygen [86]. Typically, the composition and thickness of thin layers can be determined with an accuracy of $< 1\%$. For bulk materials the accuracy is 3 - 4 %. The drawback of RBS is the low sensitivity for lighter elements, which often requires the combination of other nuclear based methods such as nuclear reaction analysis (NRA).

4.4.2 Data fitting and simulation

Data evaluation of RBS spectra can be carried out using conputer spectrum simulator programs such as SIMNRA. This code has the capability of calculating and modelling spectra with non-Rutherford backscattering cross-sections for a given target structure and allows fitting of target compositions to measured spectra. The reader is referred to reference [86] for an in-depth overview of the underlying physics and simulation parameters used for this study. In brief, the material sample which is referred to as the target is subdivided into individual sublayers. Each simulated spectrum consists of isotope contributions of each sublayer of the corresponding sample target. The incident particles lose energy once they penetrate a sublayer and the beam energy is spread (this is due to what is known as straggling). The SIMNRA program essentially calculates the energy of backscattered particles from the front and the backside of the sublayer, and the energy of these particles when reaching the detector.

5 Experimental procedures

5.1 Substrate preparation

Soda-lime glass (SLG) substrates with dimensions 75 x 25 x 1 mm^2 (three slides used in one deposition run giving a total substrate area of 75 x 75 mm^2) were used for this study and underwent a thorough multi-stage cleaning procedure as follows: sequential ultrasonic cleaning in decon-90 detergent/deionised water solution, ethanol and isopropanol each with a duration of five minutes. The slides were then subsequently

dried with N_2 gas flux. Prior to any deposition within the sputtering chamber, the substrates were subjected to electrical glow discharge (plasma created via the passage of current through the argon working gas) at an operating vacuum around 1 x 10^{-2} mbar for ten minutes at room temperature to help with the outgassing of material and further eliminate any surface organic contaminants. Care was taken not to subject the substrate to high energies or extended glow times that would in any way cause surface damage and/or preferential sputtering.

5.2 Deposition and characterisation of precursor metal libraries

The preparation and calibration of metal precursors was comprehensively described in Section 3.2. Deposition was achieved under high vacuum within an Ar atmosphere at an operating pressure of $\approx 5\times10^{-3}$ mbar using three Torus two inch targets (Kurt J. Lesker). The target-substrate distance was fixed at 100 mm. Two very different approaches for the deposition of Cu-Zn-Sn metallic precursors were explored at room temperature via DC magnetron sputtering (Kurt J. Lesker chamber) onto stationary 75 x 75 mm^2 soda-lime glass (SLG) substrates: i) co-deposition and, ii) sequential stacking of each element. This consisted of depositing each element alternately and repeating four times giving a total of 12 discrete layers to promote intimate mixing. The elements were further arranged in different stacking orders to investigate the effect of how each metal reacts with different neighbouring elements and how this ultimately affects the complex crystallisation process of CZTS. The assembly of the two diffferent configurations are illustrated in Figure 19.

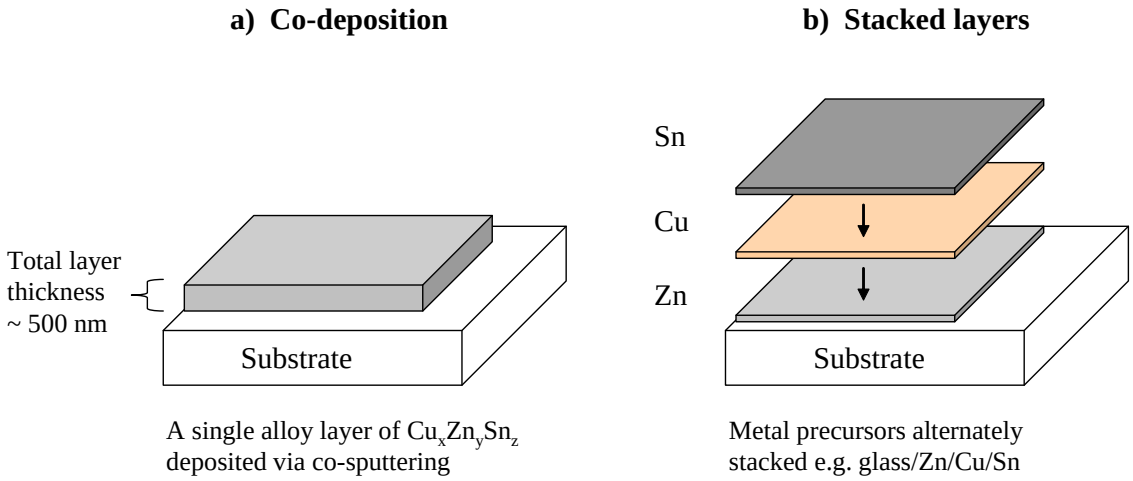

Figure 19: **Two different precursor deposition configurations a) co-deposited metals and, b) sequentially stacked layers of each metal.**

To summarise, the total number of metal precursor libraries that were fabricated are as follows:

1. Co-deposited Cu-Zn-Sn metal alloy onto glass, and;

2. Sequential stacking onto glass with different metal orders: Cu/Zn/Sn; Cu/Sn/Zn; Zn/Cu/Sn; Zn/Sn/Cu; Sn/Zn/Cu; Sn/Cu/Zn.

From the calculations in Section 3.2, Sn was selected as the common element due to power constraints. A value of 40 W was selected for Sn, thus power values for Cu and Zn could be calculated accordingly. Tables 4 and 5 summarise the experimental conditions for both a co-deposited and stacked library, respectively. The total precursor layer thickness was estimated at 500 nm based on the QCM values during calibration. It is important to note that for the stacked configuration, each discrete layer was approximately 42 nm in thickness (thus 12 layers in total would yield an approximate thickness of 500 nm). Furthermore, the deposition rate R, has now been converted to nms^{-1}.

Element	Power, P (W)	Rate, R (nms^{-1})	Thickness, d (nm)	Time, t (s)
Cu	65	0.4	-	-
Zn	22	0.32	-	-
Sn	40	0.56	-	-
	Total	**1.8**	**1 layer = 500**	**278**

Table 4: Deposition parameters for each element used to fabricate a co-deposited library with a total layer thickness of 500 nm.

Element	Power, P (W)	Rate, R (nms^{-1})	Thickness, d (nm)	Time, t (s)
Cu	65	0.4	42	300
Zn	22	0.32	42	272
Sn	40	0.56	42	472
	Total	**1.8**	**12 layers = 500**	**1044**

Table 5: Deposition parameters for each element used to fabricate a stacked precursor library. Note that four layers of each element are deposited three times (total of 12 layers) to yield a final film thickness of 500 nm.

Elemental analysis was obtained using EDS rastor scan measurements (25 kV accelerating voltage). The phase structures and crystallinity were identified by correlating the same points using XRD measurements made on a Bruker D8 microdiffractometer with a Cu Kα radiation source (λ = 1.5406 Å) and GADDS area detector (spot size ≈ 500 μm). The RBS analysis of the samples was to verify film composition at the centre of the library (region of near-stoichiometry) using a 2 MeV (He ions) Van de Graaff accelerator. A surface barrier detector with 20 keV of FWHM-energy resolution was positioned at an angle of 165°. The RBS spectra were analyzed using the SIMNRA code [87].

6 Results and Discussion

This chapter begins by focussing on the analysis of the co-sputtered and stacked precursor metal libraries deposited at room temperature, prior to any sulphurisation/annealing treatment. Due to this low ambient temperature, very similar results for each configuration in terms of composition and phase formation can be assumed to occur. Thus, the focus is on only two of the precursor deposition configurations: co-sputtered and a stacked library with a sequential ordering of glass/Sn/Cu/Zn. All results for the other libraries with varying stacking orders can be reviewed in the Appendix section.

6.1 Compositional and crystalinity results on co-deposited metal precursor thin films

6.1.1 Compositional analysis

Elemental composition was quantitatively determined by sequentially mapping across the libraries using EDS and contour plots are shown in Figure 20 for the co-sputtered metallic precursors as a function of distance across the substrate, prior to the incorporation of sulphur. The orientation of each metal pattern is in accordance with the setup as illustrated in Figure 18. It is clear from the plots that there is an incremental change in elemental concentration as illustrated by the "band-like" changes laterally across the substrate. This is approximately the same for Zn and Sn (within the range 5 - 55 at. %). The concentration range for Cu is substantially higher (25 - 85 at. %) as desired. Towards the centre of the library the region of near-stoichiometry is obtained i.e. Cu/(Zn+Sn) $\approx$ 1 (Cu $\approx$ 50 at.% with Zn and Sn both equal to $\approx$ 25 at. %).

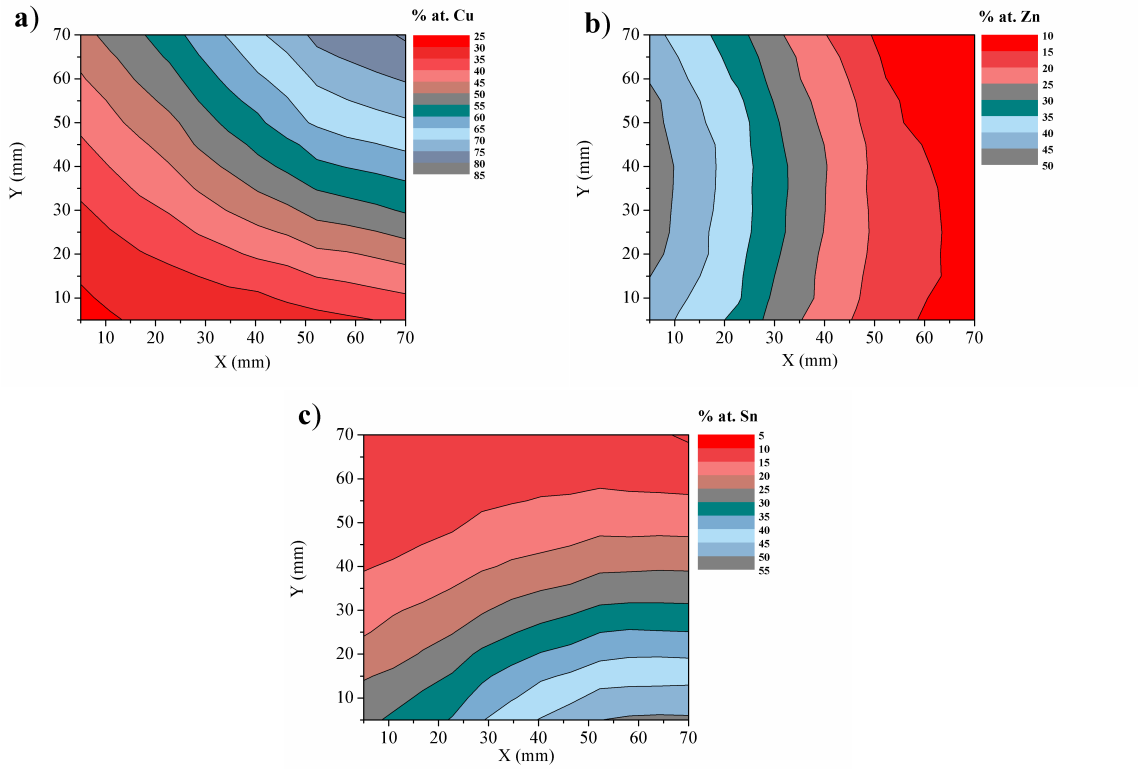

Figure 20: **Elemental contour plots obtained from EDS measurements illustrating the total composition of each constituent element for the co-sputtered precursor library: a) (% at.) Cu; b) (% at.) of Zn; and c) (% at.) of Sn.**

Raster scanned EDS-measurements were obtained to derive elemental contour plots for the precursor library represented by the two ratios Zn/Sn and Cu/(Zn+Sn), as depicted in Figure 21 (a and b), respectively. This best illustrates the change in composition of the three elements and shows the targeted stoichiometric region (Zn/Sn = 1 and Cu/(Zn+Sn) = 1) forming a distinct central band (this region is located on or close to the boundary of the two central light red bands in Figure 21a and b), for which the possible formation of phase-pure kesterite is expected to occur when the precursor material undergoes chalcogenisation. Either side there is a moderately large spatial deviation spanning the approximate range from near-zero to 4.5 across the composition-spread library.

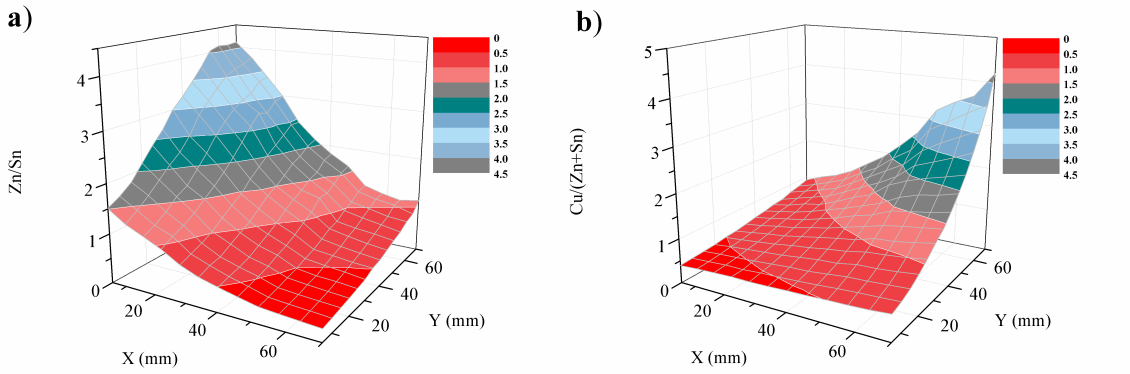

Figure 21: **Elemental ratio contour plots as determined from EDS measurements for co-deposited precursor metals as a function of position: a) Zn/Sn and, b) Cu/(Zn+Sn).**

The thickness and surface roughness values as well as the verification of the composition of the grown single precursor layer were obtained from the analysis of the RBS spectra as shown in Figure 22 and summarised in Table 6.

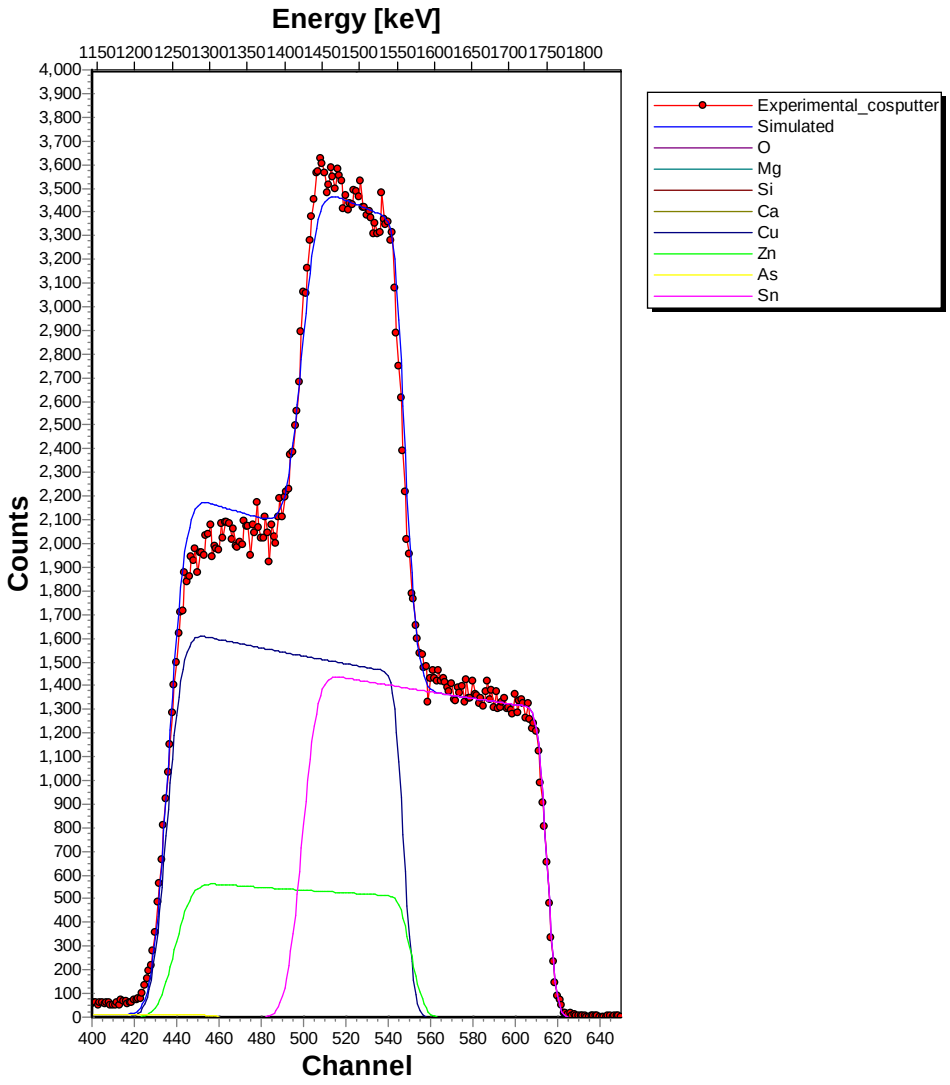

Figure 22: **RBS spectrum of a near-stoichiometric co-sputtered $Cu_xZn_ySn_z$ single precursor layer onto glass (positioned in the centre of the library). The sample structure, the thickness and the surface roughness of the layer (in atoms/cm^2) are summarised in Table 6. Note: substrate elemental information which occurs at lower energies is excluded.**

	Concen. (at. %)			t, (10^{15} atoms/cm^2)
Layer	**Cu**	**Zn**	**Sn**	**CuZnSn**
1	55	21	26	2220
Total	**$Cu_{55}Zn_{21}Sn_{26}$**			**2220**
R_S, (10^{15} atoms/cm^2)				**150**

Table 6: **Summary of RBS parameters obtained from the SIMNRA simulation model: elemental atomic concentration (at. %); layer thickness, t (10^{15} atoms/cm^2); and surface roughness, R_S (10^{15} atoms/cm^2).**

Phase	Structure	Lattice parameters (Å)	Source	PDF no.
CuZn	cubic	a = 2.959	[89]	65-9061
Cu_5Zn_8	cubic	a = 8.878	[90]	71-397
CuSn	hexagonal	a = 4.198; c = 5.096	[91]	65-3434
Cu_6Sn_5	monoclinic	a = 11.022; b =7.282; c = 9.827; β = 98.84°	[92]	65-2303
Sn	tetragonal	a = 5.8316; c = 3.181	[93]	86-2265

Table 7: **A list of the XRD standards (Search-Match Crystallographica) used in this study for the Cu-Zn-Sn ternary system at low temperature.**

The composition as expected and as verified by EDS measurements shows a near-stoichiometric region in the centre of the library. In fact, the very centre of the library is moderately Cu-rich and Zn-deficient (slightly Sn-rich). The spectrum in Figure 22 suggests the interdiffusion of all three elements, even at room temperature, yielding a very smooth thin film. It is important to note that RBS, as well as all other ion beam techniques, provides quantitative results for the amount of atoms per unit area in each layer. A film thickness and surface roughness measurement value in other units, such as nanometres or angstroms, can only be obtained if the atomic density of the layers is known. In this case, with three different metallic elements being deposited simultaneously, this would prove to be very difficult to obtain and so the units, atoms/cm^2, are used. Although this unit of measurement cannot be a direct comparison to nanometres of which this study uses, it will give a clear indication in terms of thickness and roughness changes between the different configurations.

6.1.2 Phase analysis and crystal structure

Table 7 shows a list of the standards used in this study to identify the precursor peaks present. Sn further has a crystal diamond structure [88] and is in fact semiconducting although has been excluded from this study.

Figure 23 shows the composition dependence of diffractograms for selected regions within a 2θ range from 21° to 55° for the co-sputtered Cu-Zn-Sn precursor library. The different compositions a) - d) are summarised in Table 8.

The observed peaks are attributable to the co-existence of multi-phase alloys. The point of near-stoichiometry (Zn/Sn ≈ 1.01; Cu/(Zn+Sn) ≈ 1.02) is included as

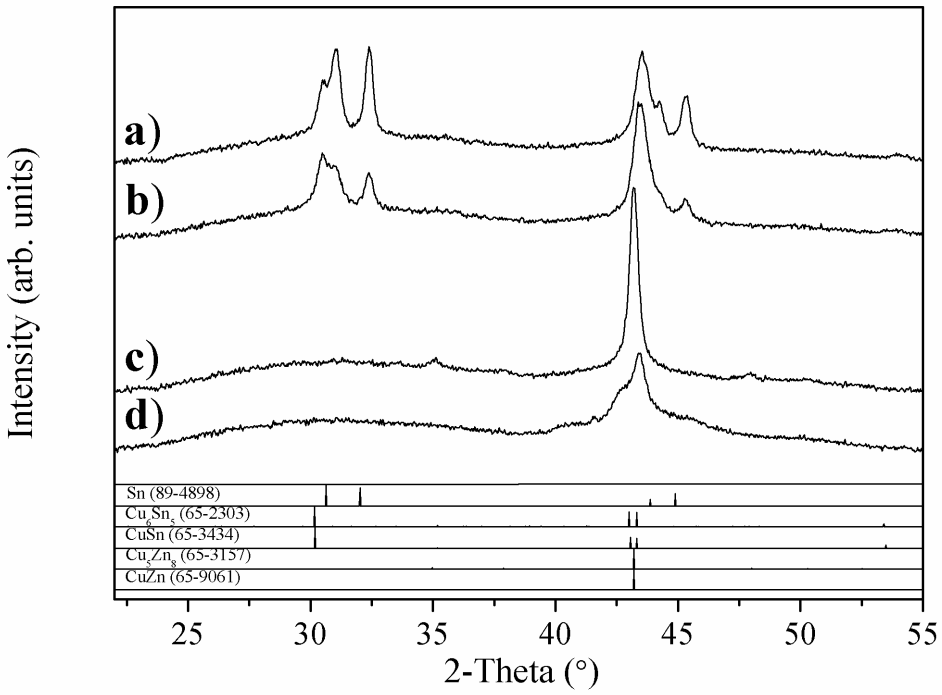

Figure 23: **Diffractograms of co-sputtered precursor metals at room temperature indicating the evolution in crystalline phases with respect to selected composition ratios, Cu/(Zn+Sn) and Zn/Sn, across the library.**

a reference to clearly show and identify phase transformations and peak shifts with respect to compositional change. Although not all compositions are shown, these diffractograms best represent the most abrupt changes in crystal structure observed across the library.

	Composition ratios	
Region	**Cu/(Zn+Sn)**	**Zn/Sn**
a)	0.55	0.46
b)	0.69	0.67
c)	1.01	1.00
d)	2.24	1.83

Table 8: **Summary of composition ratios corresponding to the selected diffractograms a) - d) in Figure 23.**

Characterisation of the specific precursor phases are necessary, since these phases determine the reaction pathway leading to CZTS and additional sulphide compounds that form post-annealing. The observed values of the Bragg d-spacings are compared

with standard d-spacings for the precursor compounds found, as summarised in Table 9, and are shown to be in very good agreement. Multiple copper-metallic binary compounds with Zn (CuZn and Cu_5Zn_8) and Sn (CuSn and Cu_6Sn_5) were found to predominantly exist. It is difficult, however, to clearly distinguish between CuZn (PDF #65-9061) and Cu_5Zn_8 (PDF #71-397), and CuSn (PDF #65-3434) and Cu_6Sn_5 (PDF #65-2303), respectively, due to similar peak positions and intensities.

	2θ (°) / d (Å)	**hkl / d (Å)**				
	Observed	**CuZn**	**Cu_5Zn_8**	**CuSn**	**Cu_6Sn_5**	**Sn**
		(65-9061)	**(71-397)**	**(65-3434)**	**(65-2303)**	**(86-2265)**
a)	30.6 / 2.93			101 / 2.96	311 / 2.96	
	31.0 / 2.88					200 / 2.90
	32.4 / 2.76					101 / 2.79
	43.5 / 2.08	110 / 2.09	330 / 2.09	102 / 2.09	510 / 2.09	
	44.2 / 2.05					220 / 2.06
	45.3 / 2.00					211 / 2.02
	53.0 / 1.70			201 / 1.71	423 / 1.71	
b)	30.5 / 2.93			101 / 2.96	311 / 2.96	
	31.0 / 2.88					
	32.4 / 2.76					101 / 2.79
	43.4 / 2.08	110 / 2.09	330 / 2.09	102 / 2.09	510 / 2.09	
	45.3 / 2.00					211 / 2.02
	53.9 / 1.70			201 / 1.71	423 / 1.71	
c)	35.1 / 2.55		222 / 2.56			
	43.2 / 2.09	110 / 2.09	330 / 2.09	102 / 2.09	510 / 2.09	
d)	42.9 / 2.10			110 / 2.10	204 / 2.10	
	43.4 / 2.08	110 / 2.09	330 / 2.09	102 / 2.09	510 / 2.09	

Table 9: **Peak assignment for each diffractrogram in Figure 24 (a - d).**

For instance the 110 peak for CuZn and the 330 peak for Cu_5Zn_8 coincide at an angle around 43.5°. Cu_xSn_y compounds potentially also occur at this angle (due to the good match with d-spacing values) but do not necessarily form as an associated higher intensity peak also occurs at lower Bragg angles (the 101 peak at 30.17° for CuSn and the 311 peak at 30.15° for Cu_6Sn_5). Thus, it is also very difficult to distinguish which Cu_xSn_y related phases are present. Therefore, it can be assumed that more than one of the four phases may be present as a phase-mixture in certain regions but this would require further investigation. There is clear evidence, however, of solid elemental Sn occurring at elevated concentrations (particularly when the film

is Cu deficient, thus preventing any Cu_xSn_y phases). From the range of compositions studied, there is no evidence to suggest the precipitation of any ternary compounds, elemental Zn and Cu, or Zn_xSn_y binary phases. This is, however, of no surprise for the Zn_xSn_yphases. As discussed in Section 2.5.3, the Zn-Sn binary phase diagram predicts no intermediate solid solutions at any temperature or compositional range. In the case for the other phases, this could be due to the peaks being present in a non-crystalline form, or more likely the unfavourable synthesis conditions necessary for compound formation.

In Figure 23, only diffractograms relating to regions with the most abrupt crystallographic changes were shown. In Figure 24, diffractograms are shown from two line scans across the graded precursor library (both of which intercept the centre of the library representing the stoichiometric region, as denoted by the shaded region) that indicate the extent to which peak intensities vary.

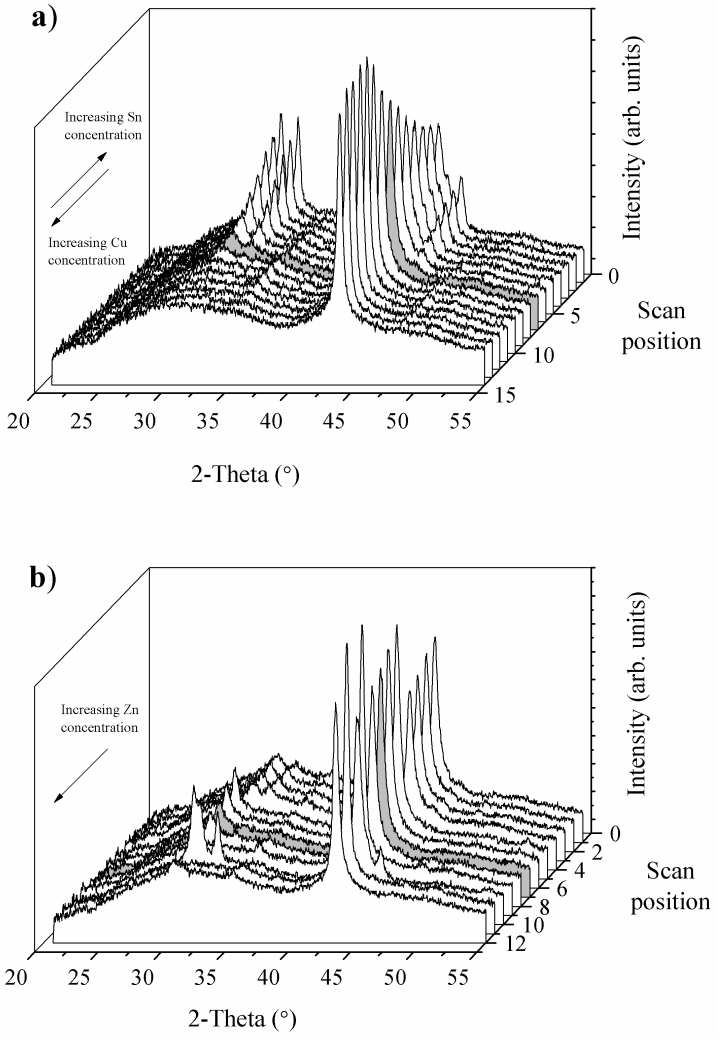

Figure 24: **Diffractograms with respect to two scan positions across the co-sputtered sample. a) Change of Cu and Sn composition and, b) change of Zn concentration. Shaded region indicates stoichiometric point (centre of library).**

Figure 24a shows a clear change in peak intensity with respect to changes in Cu and Sn concentration. More precisely, the peak located at 30.6° increases with Sn content and completely disappears in Cu-rich regions. On the contrary, the peak situated at the angle 43.5° increases with elevated levels of Cu in the film. Interestingly, as seen in Figure 24b, there is little change in peak intensity with respect to Zn concentration. The rise in peak intensities is generally more noticeable towards the stoichiometric region of the library which is attributable to improved film crystallinty. This is also reinforced by the reduced shifts in peak positions as

confirmed from the d-spacing values observed in Table 9.

A ternary phase-composition plot was constructed using combined measurements from XRD and EDS as illustrated in Figure 25, showing the change in composition and multi-phase structure for the precursor Cu-Zn-Sn system. A relatively large spatial region is sampled on a single substrate focussing around the small region of stoichiometry as indicated by the intersection of the dashed lines (precursor ratio Cu:Zn:Sn = 2:1:1). The construction of the phase diagram is an adaptation of the theoretical 180° C and experimental 210° C isothermal sections [62], where all binary Cu_xZn_y and Cu_6Sn_5 phases have tie-lines with solid Sn and no liquid phases (due to low temperatures).

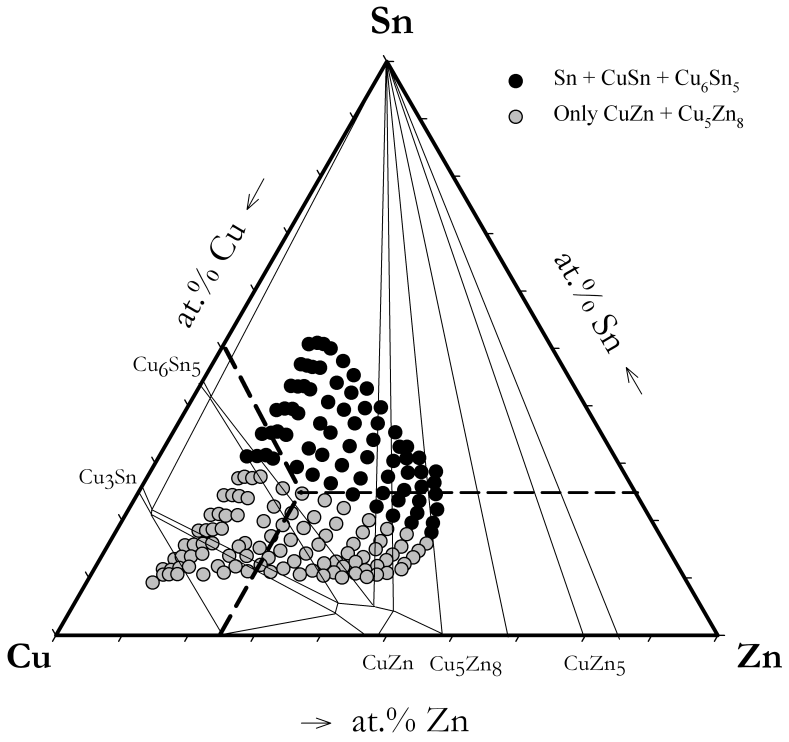

Figure 25: **Precursor (co-deposited) phase-composition plot superimposed onto the ternary Cu-Zn-Sn equilibrium phase diagram [73]. Intersection of the dashed lines denotes stoichiometric precursor ratio (Cu:Zn:Sn = 2:1:1).**

There is a clear "cut-off" boundary where phase transformation is most prominent. As shown in Table 9, the peak positions of the Cu_xZn_y phases are likely to occur in all regions of the phase diagram, as the single dominant peak located at 43.5° occurs at all points. As the Sn concentration increases additional Cu_xSn_y

phases form alongside the Cu_xZn_y phases (denoted by the black points in the phase diagram). The region of stoichiometry does not consist of any Cu_xSn_y phases, which may give a clear indication of which phases are favourable under these conditions when converting the precursor metals into a sulphide compound. There is no evidence of the Cu_3Sn binary alloy forming which is expected to arise at higher temperatures ranging from approximately 60 - 90 °C [94]. Furthermore, the $Cu_{41}Sn_{11}$ phase is non-existent which has been observed to form at even higher temperatures ranging from 200 - 350 °C [95]. The Zn-rich compound, $CuZn_5$, is predicted to form at compositions outside the range of this study. A study has shown, however, the instability of the phase $CuZn_5$ such that it is slowly consumed by Cu_5Zn_8 with respect to increased ageing time [96]. It is important to realise that although generally the observed phases are strongly dependent on elemental change and are in good agreement with the phase diagram, the low temperature conditions and thin film effects (non-bulk compound) used in this study yield only non-equilibrium phases. A more comprehensive study with respect to changes in temperature is required to evaluate the evolution of further phase formation.

6.2 Compositional and crystalinity results on sequential metal precursor thin films with stacking order: glass/Sn/Cu/Zn

6.2.1 Compositional analysis

Similar analysis was carried out for the multilayer precursor libraries with varying stacking orders. Figures 26 and 27 show the EDS-derived contour plots of individual elements and ratios with respect to substrate distance, respectively, for the Sn/Cu/Zn stack configuration.

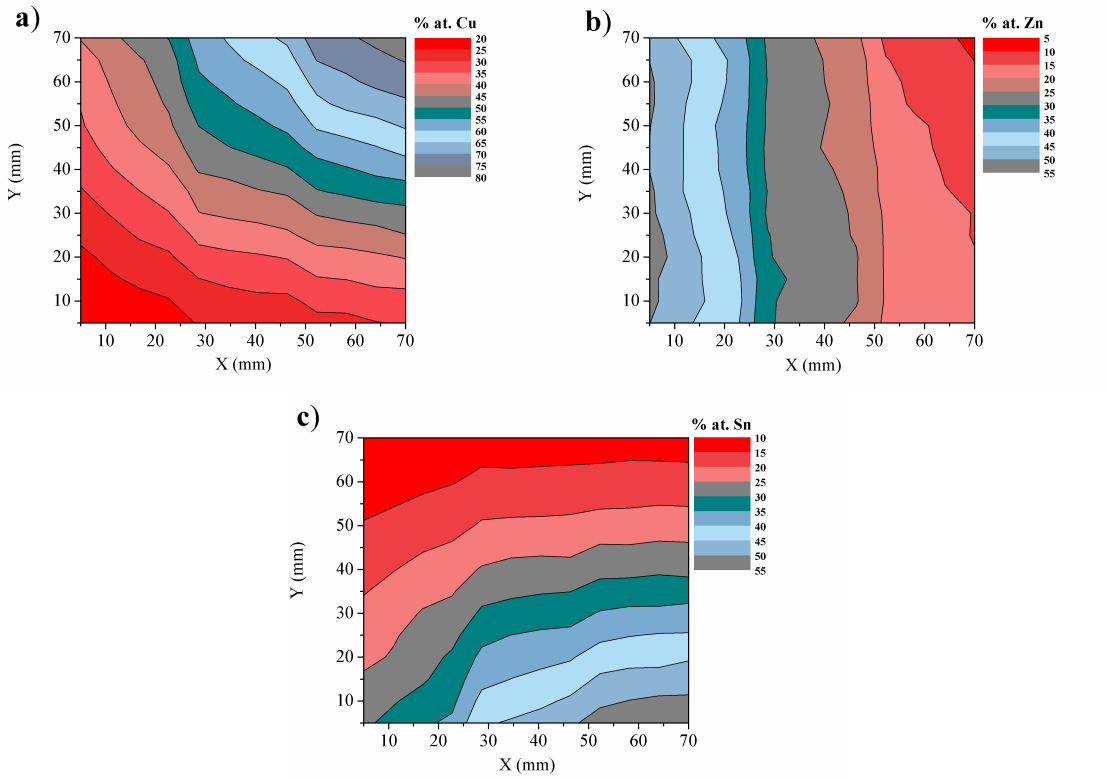

Figure 26: **EDS-derived elemental contour plots illustrating the total composition of each constituent element for the Sn/Cu/Zn stacked precursor library: a) (% at.) Cu; b) (% at.) of Zn; and c) (% at.) of Sn.**

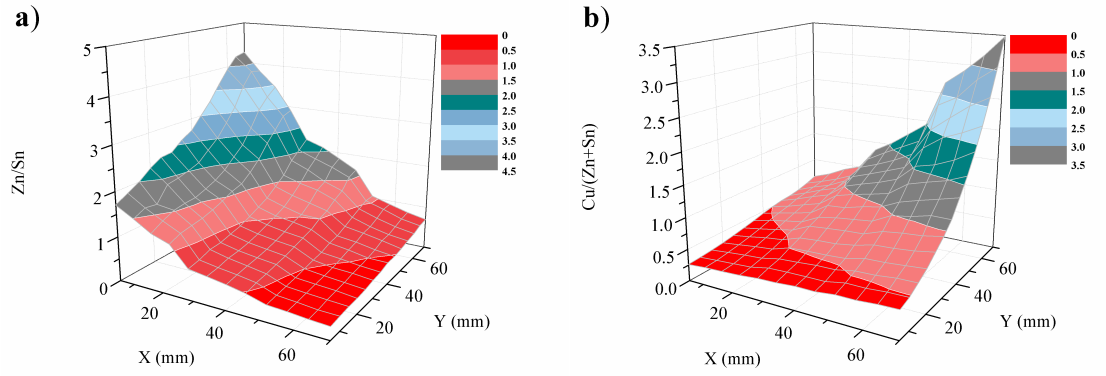

Figure 27: **EDS-derived elemental ratio contour plots for sequential stacking order Sn/Cu/Zn as a function of position: a) Zn/Sn and, b) Cu/(Zn+Sn).**

Importantly for comparative purposes, the calibration and system geometry have enabled very reproducible outcomes in terms of the composition-spread for both the co-deposited and stacked configuration, with the stoichiometric region forming a band towards the centre of the library. This in fact holds true for all stacked

libraries with different element orders as can be seen in the Appendix section.

The RBS spectrum in Figure 28 shows the intermixing of all the discrete layers in the film. It further illustrates, interestingly, a small and well defined front peak associated with the heavy element Sn. This is somewhat different to that observed with the co-deposition route whereby a much broader peak was evident. This may suggest the likelihood of a non-homogenous film with respect to film depth.

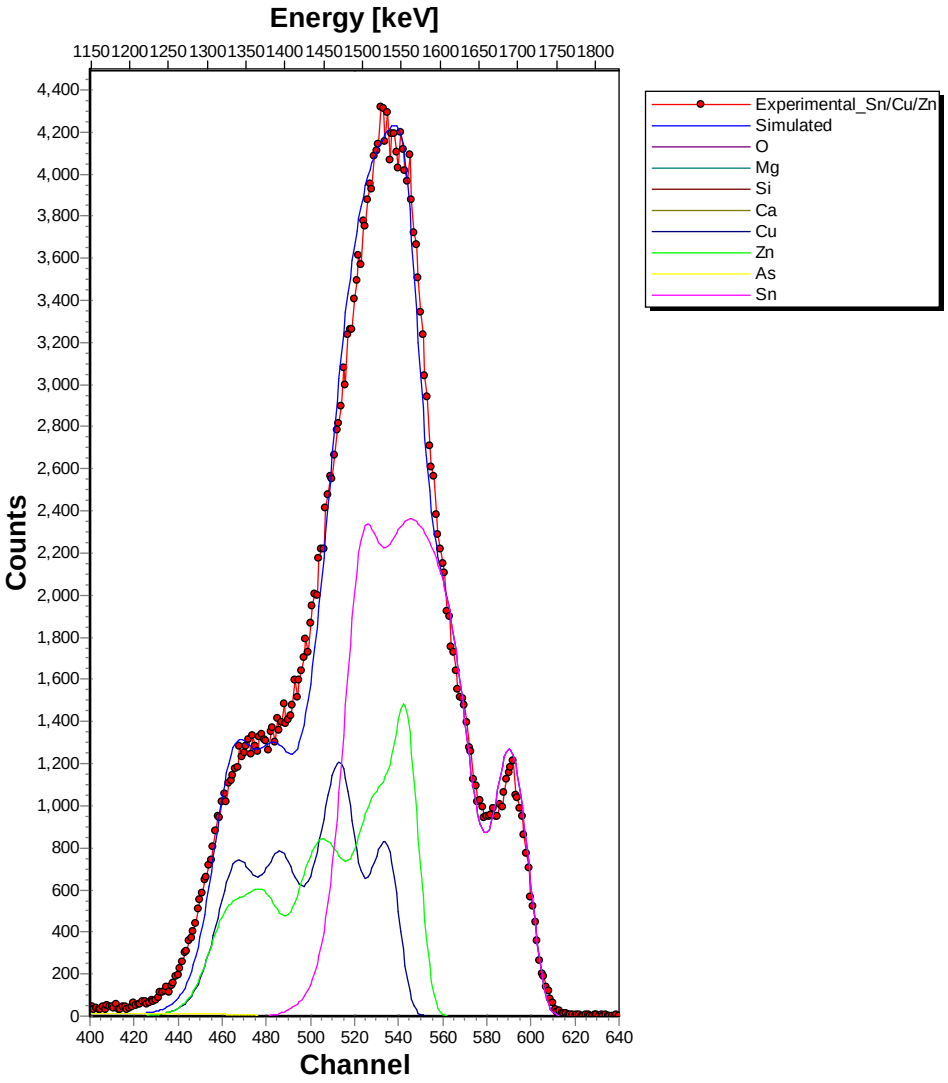

Figure 28: **RBS spectrum of a stacked $Cu_xZn_ySn_z$ precursor layer onto glass with stacking order: Sn/Cu/Zn. The sample structure, the thickness and the surface roughness of the layer (in atoms/cm^2) are summarised in Table 10. Note: substrate elemental information which occurs at lower energies is excluded.**

This is perhaps reinforced in Table 10, which summarises the RBS model used to simulate the collected RBS spectra for the stacked layer. As 12 individual layers were deposited (Sn/Cu/Zn repeated four times), the model is based on this configuration and accounts for all discrete layers. This is noticeable by the undulating nature of the elemental profiles in Figure 28. Layer 12 in this case denotes the first layer deposited directly onto the underlying glass substrate i.e. in this case a single Sn layer. From these undulating peaks, there is evidence to suggest a Sn-deficient top region of the film (dominated by Cu but also Zn-rich), which would further imply diffusion of elemental species within the film. The final film composition at this particular point in the centre of the substrate is Cu-poor and slightly Zn-rich with a film thickness approximately 6% thinner than that of the co-deposited film. The surface roughness is almost doubled in magnitude.

	Concen. (at.%)			**t, (10^{15} atoms/cm^2**
Layer	**Cu**	**Zn**	**Sn**	**SnCuZn**
1	70	30	-	200
2	100	-	-	150
3	30	45	25	150
4	10	60	30	160
5	100	-	-	150
6	30	50	20	150
7	20	40	40	230
8	60	-	40	170
9	35	20	45	200
10	20	40	40	170
11	55	15	30	150
12	10	35	55	200
Total	**$Cu_{45}Zn_{28}Sn_{26}$**			**2080**
R_S, (10^{15} atoms/cm^2				320

Table 10: **Summary of RBS parameters obtained from the modelling within SIMNRA for the multi-layer structure: elemental atomic concentration (at. %); layer thickness, t (10^{15} atoms/cm^2); and surface roughness, R_S (10^{15} atoms/cm^2).**

6.2.2 Phase analysis and crystal structure

The diffractograms represented in Figure 29 show a major difference to those observed for the co-deposited library in Figure 23. As summarised in Table 11, diffrac-

togram (c) shows the region of near-stoichiometry with an additional peak present at the Bragg angle 30.5°. With confirmation of the calculated d-spacing values in Table 12, this peak can only be associated with Cu_xSn_y compounds suggesting even at a composition close to ideality, the phase mixture is such that it consists of both Cu_xZn_y and Cu_xSn_y phases. This was not evident with the co-deposited library.

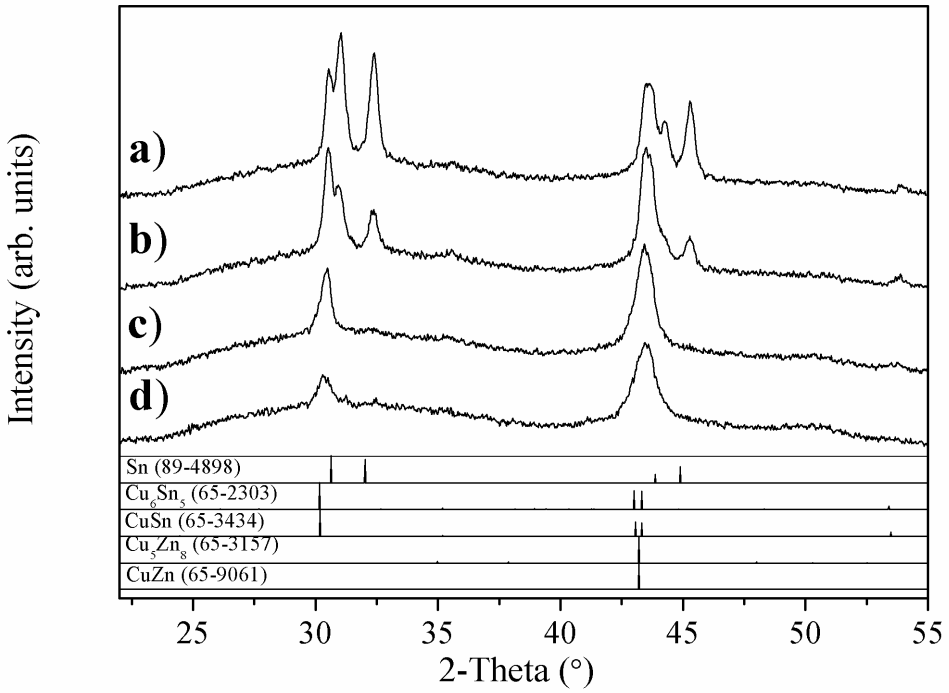

Figure 29: **Diffractograms of stacked (Sn/Cu/Zn) precursor metals indicating the evolution in crystalline phases with respect to selected composition ratios Zn/Sn and Cu/(Zn+Sn) across the library.**

	Composition ratios	
Region	**Cu/(Zn+Sn)**	**Zn/Sn**
a)	0.61	0.59
b)	0.84	0.72
c)	1.02	0.99
d)	1.32	1.17

Table 11: **Summary of composition ratios corresponding to the selected diffractograms in Figure 29.**

The reason could be due to the fact that sequential layers of metals create a non-homogenous film with respect to depth when deposited at low temperatures. In other

words, instead of the elements interdiffusing to create a homogenous film, segregation is occurring causing an imbalance of each element with respect to film depth. As seen from the RBS model in Figure 28 and Table 10, Sn predominately accumulates in the lower to mid-region of the film, whereas Zn favours a higher concentration in the mid-upper region. Furthermore, with Cu being embedded in the middle of the other two elements it is likely both Cu_xZn_y and Cu_xSn_y compounds will form. Although not confirmed, one could assume that phase segregation may occur such that Cu_xSn_y phases precipitate in the lower region and Cu_xZn_y towards the upper region. This disparity in phase formation could lead to undesirable secondary phases forming during the sulphurisation process, of which we address later on in Chapter 6.

	2θ (°) / d (Å)	**hkl / d (Å)**				
	Observed	**CuZn**	**Cu_5Zn_8**	**CuSn**	**Cu_6Sn_5**	**Sn**
		(65-9061)	**(71-397)**	**(65-3434)**	**(65-2303)**	**(86-2265)**
a)	30.6 / 2.93			101 / 2.96	311 / 2.96	
	31.0 / 2.88					200 / 2.90
	32.4 / 2.76					101 / 2.79
	43.5 / 2.08	110 / 2.09	330 / 2.09	102 / 2.09	510 / 2.09	
	44.2 / 2.05					220 / 2.06
	45.3 / 2.00					211 / 2.02
	53.9 / 1.70			201 / 1.71	423 / 1.71	
b)	30.5 / 2.93			101 / 2.96	311 / 2.96	
	31. 0 / 2.88					
	32.4 / 2.76					101 / 2.79
	43.4 / 2.08	110 / 2.09	330 / 2.09	102 / 2.09	510 / 2.09	
	45.3 / 2.00					211 / 2.02
	53.9 / 1.70			201 / 1.71	423 / 1.71	
c)	30.5 / 2.93			101 / 2.96	311 / 2.96	
	43.4 / 2.098	110 / 2.09	330 / 2.09	102 / 2.09	510 / 2.09	
d)	30.5 / 2.93			101 / 2.96	311 / 2.96	
	43.4 / 2.098	110 / 2.09	330 / 2.09	102 / 2.09	510 / 2.09	

Table 12: P**eak assignment for each diffractrogram in Figure 29 (a - d).**

Figure 30 shows the diffractograms with respect to library position across two scan lines. As with the co-sputtered library in Figure 23, the change in peak intensities suggests a change in crystallinity which is highly dependent on elemental concentration. The peak located at 30.6° increases with Sn content (decreasing in

Cu-rich regions although it does not completely disappear as in the case of the co-sputtered library). The 43.5° peak increases only marginally with elevated levels of Cu in the film. Both Figures a) and b) consolidate the presence of Cu_xSn_y compounds forming even in composition areas rich in Cu and Zn.

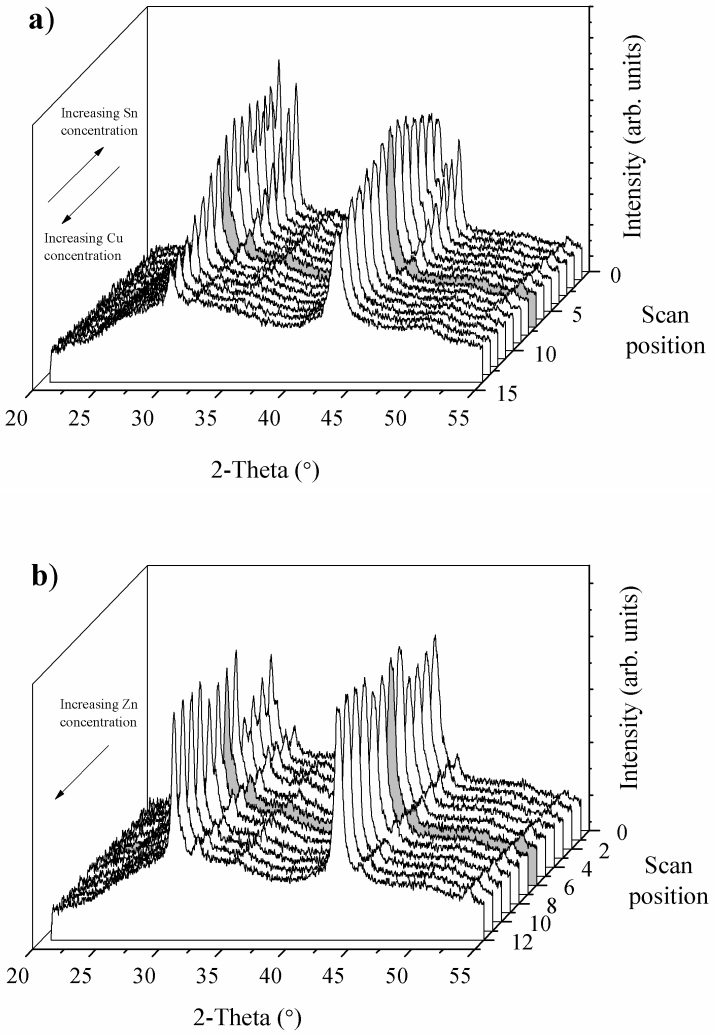

Figure 30: **Diffractograms with respect to two scan positions across the multilayer Sn/Cu/Zn sample. a) Change of Cu and Sn composition and, b) change of Zn concentration. Shaded region indicates stoichiometric point (centre of library).**

A precursor ternary phase-composition plot was derived as shown in Figure 31. Very similar characteristics are observed to that of the co-sputtered library. The only major difference with the stacked library is the cut off boundary such that all

regions now consist of Cu_xZn_y and Cu_xSn_y phases.

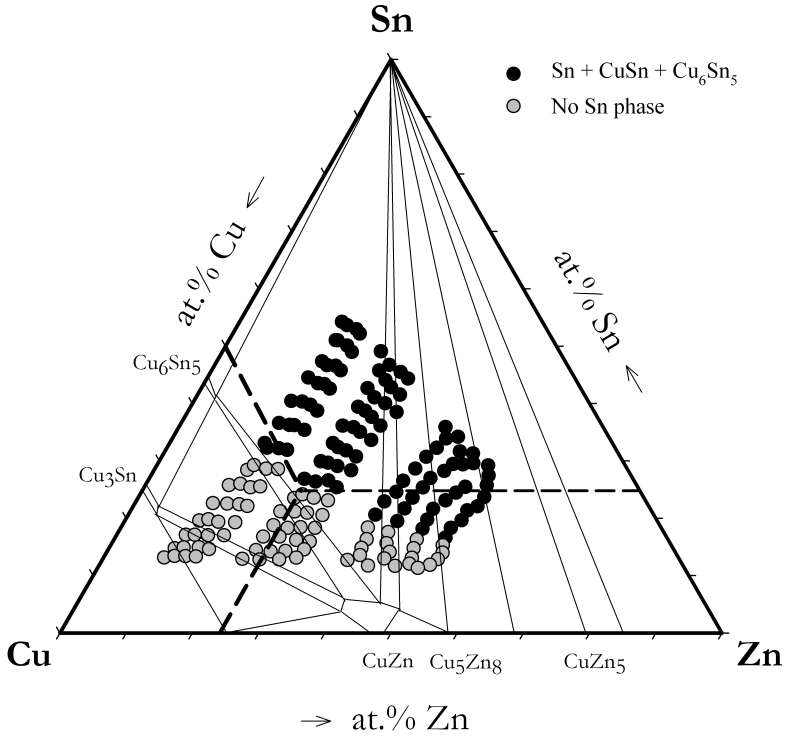

Figure 31: **Precursor (stacked - Sn/Cu/Zn) phase-composition plot superimposed onto the ternary Cu-Zn-Sn equilibrium phase diagram [73]. Intersection of the dashed lines denotes stoichiometric precursor ratio (Cu:Zn:Sn = 2:1:1).**

6.2.3 A brief note on other precursor stacking order libraries

Only two different deposition configurations with regards to the fabrication of precursors have been presented here, namely, the co-sputtering of metals and the sequential stacking with an order of glass/Sn/Cu/Zn. The data for the other stacking orders' are presented in the Appendix section at the end of this thesis. Due to the system geometry and calibration, all results show good reproducibility in terms of composition-spread across the library with a stoichiometric region towards the centre. Many of the same phases also precipitate which are governed by the same synthesis conditions; therefore, further exploration is not necessary. It is, however, important to bear in mind that the different stacking orders' may initiate inhomogeneous phase formation with respect to film composition and depth when subjected to heat treatment in the presence of sulphur.

6.3 Conclusions relating to the synthesis of percursor metals

Combinatorial precursor libraries of the ternary Cu-Zn-Sn metallic system have been successfully grown at room temperature using two different design configurations. The general aims of Chapters 3 and 4 were to design a combinatorial protocol for the preparation of compositionally graded Cu-Zn-Sn libraries and evaluate their properties in order to assess their suitability prior to the semiconductor conversion process. The implementation of a combinatorial setup involved a relatively straightforward and versatile geometry without the use of intricately designed masking apparatus. By inclining the target materials towards the centre of the substrate and taking into account the nature of the emission characteristics, very reproducible results in terms of composition and film thickness could be realised for both co-sputtered and stacked libraries covering a wide compositional space.

It has been observed that the co-sputtering approach could potentially be more desirable in terms of film quality, as we have seen from improved film crystallinty and homogenous intermixing of elements from the XRD and RBS measurements, respectively. The stacking approach tends to induce phase segregation with respect to film depth which could have serious and damaging implications on the conversion process into CZTS. This in fact is evident with all stacked layers with alternate elemental ordering. However, the approach of sequential stacking perhaps offers greater control over film thickness. This potential "side-effect" of phase disparity when stacking layers at low temperatures could be circumvented, or certainly minimised, by thermally treating the precursor layers either during the deposition process (heated substrate) or immediately after the completed cycle. This deliberate alloying of precursor metals has a couple of key advantages: (i) thermal energy will induce intimate mixing of elements forming a homogenous film similar to that of co-deposited samples and, (ii) induces phase stability at elevated temperatures. Of course, very high temperatures in a vacuum environment should be avoided as to reduce any elemental loss occurring as has been experienced with some groups [29]. This is one potential workaround, although it will still prove a major challenge to convert stacked layers into a homogenous film with desirable phase formation.

The other fundamental finding in this chapter of the study is the influence of el-

emental composition on the formation of films. In the regions of near-stoichiometry, where we would expect the precursor material to form phase-pure kesterite material when subjected to sulphurisation processes, there is a noticeable improvement in crystallinity (this is particularly evident with the co-sputtered library). Furthermore, for the co-sputtered library only Cu_xZn_y phases were found to be present in the stoichiometri region, but in the case of the stacked library both Cu_xZn_y and Cu_xSn_y phases co-existed. Elemental Sn only precipitated at elevated Sn concentrations (and low Cu content).

These precursors will subsequently be sulphurised by using thermal energy in the presence of pure sulphur to convert the samples into graded Cu-Zn-Sn-S libraries. Based on the above evaluation, several key conditions can be ascertained that potentially are required for the successful conversion process: (i) the deposition configuration used needs to promote a fully homogenous film without phase segragation; (ii) the Cu-Zn-Sn stoichiometry should be controlled in such a manner not to induce extraneous phases that would ultimately lead to secondary phases occurring in the sulphide compound (and hence detrimental to the structural and opto-electronic properties of the film), and (iii) growth conditions, either with the application of heat or not, need to promote complete intermixing of elements with good film crystallinity and morphology (i.e. low surface roughness).

7 Sulphurisation of precursor metals into Cu-Zn-Sn-S thin film libraries

The second stage of the dual synthesis process involves fully converting the precursor metals into a quaternary sulphide compound via annealing in the presence of chalcogen (sulphur). This chapter summarises the complete process for the fabrication of Cu-Zn-Sn-S thin film libraries and begins by exploring in greater detail the terminology used and the challenges associated with identifying compositions and phase structures with the kesterite material.

7.1 Terminology associated with the material Cu_2ZnSnS_4

When deliberately attempting to vary the precursor elements independently as is the case in this investigation, care must be taken when describing the compositions of the CZTS thin film libraries. Normally, as already dealt with, the atomic ratios Zn/Sn and Cu/(Zn+Sn) are commonly used in CZTS literature to express the composition of the metallic elements in the film. A further complementary ratio S/(Cu+Zn+Sn), or S/metal, is used to represent the overall composition of the sulphide compound. In this instance, all three ratios are equal to unity for the stoichiometric material i.e. Cu_2ZnSnS_4. This by no means makes the evaluation any simpler, as a marginal elemental change cannot be accounted for by solely assessing these ratios. So to specify whether a film is "Cu-poor" or "Zn-rich" requires further evaluation. The most suitable method would be to use a graphical representation such as a phase diagram, which has already been addressed in Section 2.5.4 for the ternary Cu-Zn-Sn ternary system. With four elements, however, a quasi-ternary phase diagram can be constructed which is introduced in the next section.

7.2 Cu_2S-ZnS-SnS_2 quasi-ternary system

There are limited studies on the phase diagram associated with CZTS. In fact, only one comprehensive investigation of the Cu_2S-ZnS-SnS_2 quasi-ternary system in bulk form at 400 °C has been carried out by Olekseyuk et al. [97]. Some important

conclusions that can be drawn from this study are illustrated in Figure 32 which include the following: the desired stoichiometric mono-phase Cu_2ZnSnS_4 only forms within a very narrow composition range (as denoted by the intersection of the dashed lines) along the Cu_2SnS_3-ZnS quasi-binary system, and proves very difficult to synthesise. The difficulty arises from the initial control of the composition, whereby any slight deviation from stoichiometry will induce secondary and/or ternary phases precipitating alongside the kesterite structure.

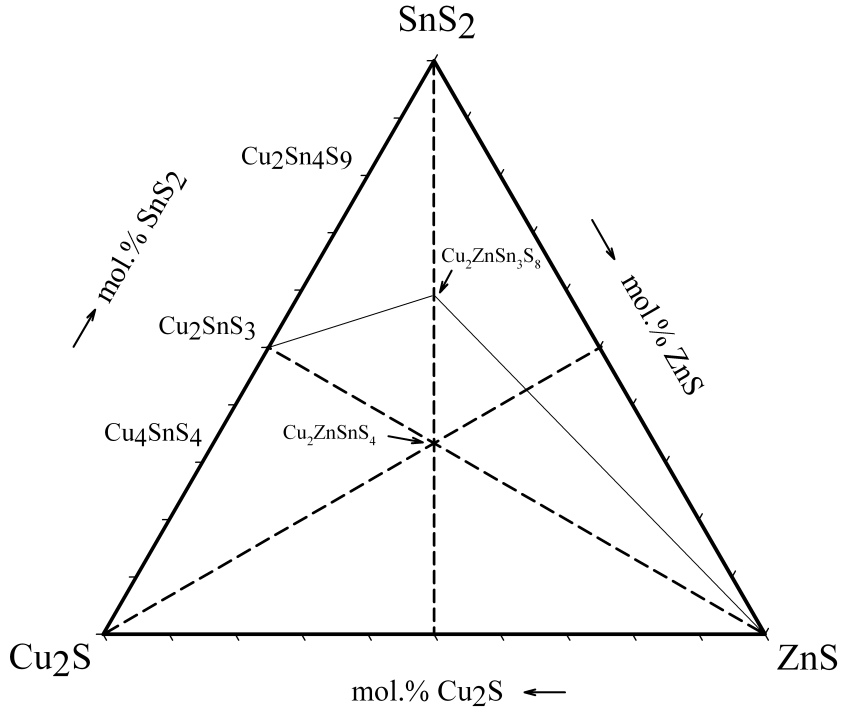

Figure 32: Cu_2S-ZnS-SnS_2 quasi-ternary system at 400 °C adapted from reference [91]. The intersection of the dashed lines denotes the region of CZTS stoichiometry.

For this research, phase diagrams are adapted and presented as in Figure 32. From the studies by Olekseyuk et al. [97] and Scragg et al. [98], specific regions can be pinpointed within the phase diagram whereby certain extraneous phases alongside the kesterite structure are expected to form. These are listed in Table 13 in terms of composition ratio.

Composition ratio	Expected extraneous phases
Cu/(Zn+Sn) > 1 ("Cu-rich")	$Cu_{2-x}S$
Cu/(Zn+Sn) < 1 ("Cu-poor")	ZnS, $Cu_2ZnSn_3S_8$
Zn/(Cu+Sn) > 1 ("Zn-rich")	ZnS
Zn/(Cu+Sn) < 1 ("Zn-poor")	Cu_4SnS_4, Cu_2SnS_3, $Cu_2Sn_4S_9$, $Cu_2ZnSn_3S_8$
Sn/(Cu+Zn) > 1 ("Sn-rich")	$Cu_2Sn_4S_9$, $Cu_2ZnSn_3S_8$, SnS_{2-x}
Sn/(Cu+Zn) > 1 ("Sn-poor")	ZnS, $Cu_{2-x}S$

Table 13: **Expected extraneous phases with respect to different composition ratios forming during the synthesis of CZTS samples.**

There are six possible regions of varying composition that certain phases are expected to occur. Of course, the precipitation of these phases depends highly on the processing and growth conditions therefore some of which may not be observed in certain studies. This is particularly true of the quaternary compound, $Cu_2ZnSn_3S_8$, of which there is very limited literature on its formation [97, 98]. Another reason why certain phases cannot be observed is the difficulty in distinguishing them using commonly employed thin film analysis techniques such as XRD, as will be addressed in the next section.

7.3 Identifying and distinguishing phases present in the CZTS material system

The identification of phases in polycrystalline thin film compounds is normally investigated using XRD. A brief overview regarding how the XRD technique is used is given in Section 4.2. As the precursor metal alloys undergo chalcogenisation, this technique becomes increasingly difficult to distinguish all the co-existing phases present as many of them share similar crystal symmetry. Thus, another technique is required that could confirm the existence of the kesterite-type structure. Many groups for this reason have resorted to using Raman spectroscopy to compliment the analysis of XRD [99, 100]. This underlying physics of this technique is briefly described in Section 4.3.

7.3.1 X-ray diffraction

Generally, XRD is more than sufficient in identifying phases within thin film materials. Unfortunately, as already mentioned, CZTS crystallises with crystallographically similar secondary phases, namely ZnS and Cu_2SnS_3. In other words, the crystal symmetry and lattice parameters are almost identical thus confounding the identification of each phase with a high degree of accuracy.

Table 14 gives a list of all the possible phases observed using Search-Match Crystallographica in the Cu_2S-ZnS-SnS_2 quasi-ternary system for this study. This is in accordance to the powder diffraction files obtained via the International Centre for Diffraction Data (ICDD). These include pure CZTS and its accompanying binary/ternary phases with each of their crystallographic properties.

	Phase	**Structure**	**Lattice parameters (Å)**	**Source**	**PDF no.**
Observed	Cu_2ZnSnS_4	Tetragonal	a = 5.427; c = 10.848	[101]	26-575
	Cu_2SnS_3	Cubic	a = 5.43	[102]	89-2877
	ZnS	Cubic	a = 5.414	[103]	77-2100
	ZnS	Hexangonal	a = 3.824; c = 31.20	[104]	72-162
	CuS	Cubic	a = 5.387	[105]	78-877
	SnS	Cubic	a = 5.445	[106]	89-2755
	SnS_2	Hexagonal	a = 3.6486; c = 5.899	[107]	23-677

Table 14: **A summary of the phases (Search-Match Crystallographica) present in this study that exist in the Cu_2S-ZnS-SnS_2 quasi-ternary system.**

7.3.2 Raman spectroscopy

One alternative technique that has been recently used to confirm and/or distinguish extraneous phases from CZTS is Raman spectroscopy. Typically, for CZTS material an optimal excitation wavelength of 532 nm is used.

Upon analysis of CZTS material using the Raman technique, there are phase-specific Raman shifts that are expected to arise. Table 15 lists the phases that predominantly form in this study with their associated vibrational shifts (based on other similar studies of CZTS as referenced).

Phase present	Raman shift (cm^{-1})	Reference
Cu_2ZnSnS_4	289, 339, 350, 370	[108, 109]
Cu_2SnS_3(tetragonal, below 673 K)	297, 337, 352	[110]
Cu_2SnS_3(cubic, above 673 K)	267, 303, 356	[111]
ZnS	275, 352	[112]
$Cu_{2-x}S$	475	[113]
SnS	160, 190, 219	[114]
SnS_2	314, 215	[115]

Table 15: **Expected Raman shifts for selected phases in the Cu_2S-ZnS-SnS_2 quasi-ternary system.**

7.4 Sulphurising compositionally graded Cu-Zn-Sn film film libraries

The most widely used technique for fabricating CZTS films is based on sulphurisation (or selenisation) of a deposited thin film elemental precursor layer consisting of Cu, Zn and Sn. Films can either be sulphurised via annealing in-situ during deposition using sulphur-containing compounds or by a secondary post-sulphurisation/anneal process. Typically, sulphurisation occurs in the presence of H_2S gas or in elemental sulphur vapour at high temperatures ($>$ 400 °C).

One of the major concerns during the synthesis is the control of sulphur content. Even when sulphur is deposited as a compound with the metal, additional sulphur must usually be incorporated into the film through post deposition annealing (due to re-evaporation of sulphur and sulphur-containing compounds). It is obvious that post deposition sulphurisation leads to substantial changes in crystal structure and film morphology. Thus, a systematic investigation of the sulphurisation methods and parameters are needed to synthesize stoichiometric large grain and phase pure CZTS films. Three fundamental parameters that need to be accounted for are as follows:

1. The effects of annealing temperature on CZTS films;

2. The effects of sulphurisation duration on the conversion process;

3. Influence of annealing atmosphere on CZTS film formation.

7.5 Experimental procedures

7.5.1 Sulphurisation and annealing

For this study, a two-stage synthesis approach is used: deposition of metallic Cu-Zn-Sn precursors and then sulphurisation/annealing. It may be considered to be the less favourable option, but this however is unavoidable due to the restricted laboratory and sputtering apparatus. Furthermore, it is important to put this current study into perspective such that it is only the compositional influence and precursor configuration (i.e. co-sputtered and stacking layers) on CZTS properties and solar cell performance that will be solely investigated. Therefore, to maintain an element of consistency the same sputtering technique and sulphurisation conditions are used for all sample libraries.

The two-stage sulphurisation and annealing is discussed in greater detail as follows:

1. **Evaporation of a sulphur layer onto the precursor sample under high vacuum**

Crystals of high purity sulphur (99.99+%, Sigma-Aldrich) were thermally evaporated under high vacuum ($\approx 1\times10^{-4}$ mbar) directly onto the precursor library at room temperature. This formed a uniform sulphur 'cap' of $\approx$ 1 μm (excess sulphur) essentially creating a Cu-Zn-Sn-S multilayer structure. Figure 33 illustrates the sulphur deposition process as monitored in-situ using a QCM. Once the shutter is opened, deposition begins until a sulphur layer of 1 μm is attained, before closing the shutter.

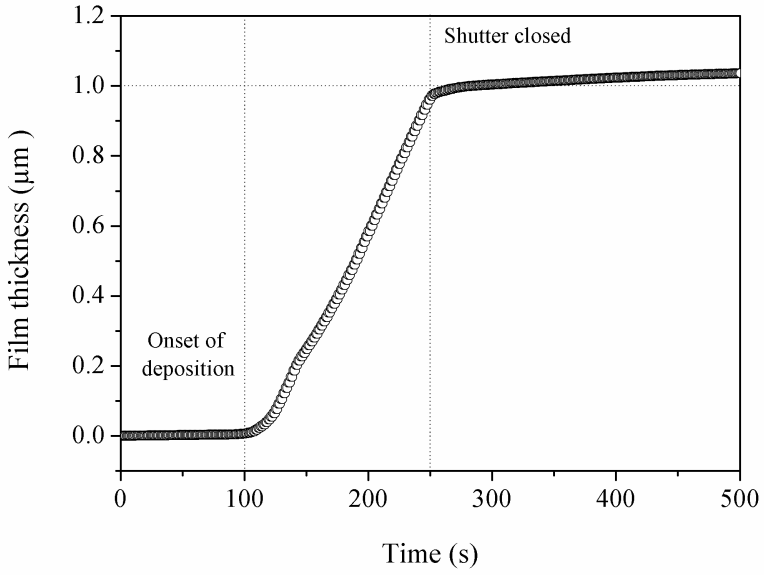

Figure 33: **Sulphur layer thickness as a function of time. Once the shutter is opened, the rate of S vapour is approximately 6.7 x 10^{-3} μms^{-1} in order to attain a 1 μm thick sulphur "cap" before the shutter is closed.**

1. **Annealing of the library in a furnace.**

The library was subsequently enclosed within a Pyrex glass ampoule and inserted into a tube furnace (Carbolite CTF) as illustrated in Figure 34, where the temperature was ramped up from 20 °C to 500 °C at approximately 10 °C min^{-1} with a total annealing time of 30 minutes. After completion, the sulphurised samples were placed into the cool zone at roughly 200 °C and remained there to naturally cool and stabilise back to room temperature. The total absorber layer thickness of the CZTS library was approximated to be 1.5 μm.

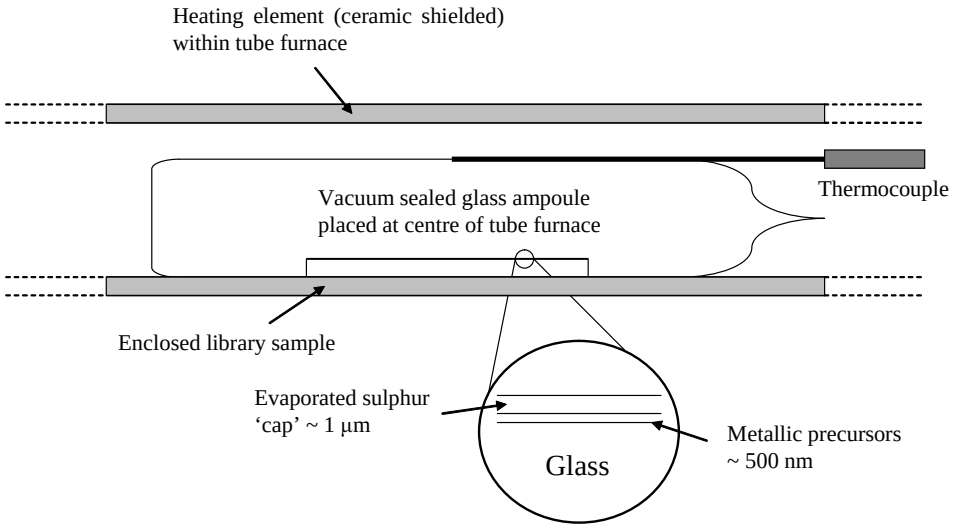

Figure 34: **Schematic of the annealing apparatus as part of the sulphurisation process. The library sample is placed under vacuum inside a closed glass ampoule and subsequently heated at 500 °C.**

The partial pressure of sulphur vapour during the heating process at 500 °C was approximated to be 2 mbar. This was calculated using the ideal gas law:

$$PV = nRT \tag{14}$$

where P is the sulphur pressure, V is the total volume of the cylindrical ampoule, n is the estimated number of moles of sulphur present, T is the maximum temperature attained during sulphurisation (taken to be 500 °C) and R is the gas law constant.

7.5.2 Chemical etching treatment

The fully sulphurised libraries were subsequently subjected to KCN chemical etching to eliminate detrimental secondary $Cu_{2-x}S$ phases that potentially formed during the crystallisation process. Samples were submerged into a 5 wt%. KCN aqueous solution for the duration of one minute, before being thoroughly rinsed and dried in deionised water and N_2 gas flux, respectively.

7.5.3 Characterisation of fully converted Cu-Zn-Sn-S material libraries

The same mapping protocol and characterisation techniques as previously outlined in Chapter 4 were used. The CZTS thin films were grown directly onto glass substrates without a Mo back contact coating to avoid the conflicting energy peaks of Mo Lα and S Kα during EDS compositional measurements. A LEO435VP scanning electron microscope (SEM) with a 25 kV acceleration voltage was used to assess film morphology. The crystal structure of the sulphide libraries were identified by correlating the same points using XRD. Raman spectroscopy was used as a complementary technique to XRD to confirm the existence of all phases present. Spectra were recorded using a triple-grating spectrometer with a subtractive double stage (acting as a tuneable band pass filter to attenuate the laser light) followed by a 1 m dispersing stage equipped with a 300 g/mm grating. The spectral resolution was approximately 2 cm^{-1} and the detector was a liquid N_2 cooled charge-coupled device (CCD). Continuous-wave excitation at 532 nm with intensity of 1 Wcm^{-2} was used. The centre of the CZTS libraries was analysed using RBS and modelled using the SIMNRA code to verify the composition and elemental distribution of the near-stoichiometric region. Opto-electronic and electrical properties of the chemically etched CZTS libraries were assessed using room temperature photoconductivity (PC) spectroscopy and the hot point probe technique, respectively. The details of each of these methods are discussed in greater detail in Chapter 8. The complete combinatorial fabrication and characterisation cycle is illustrated in Figure 35 below.

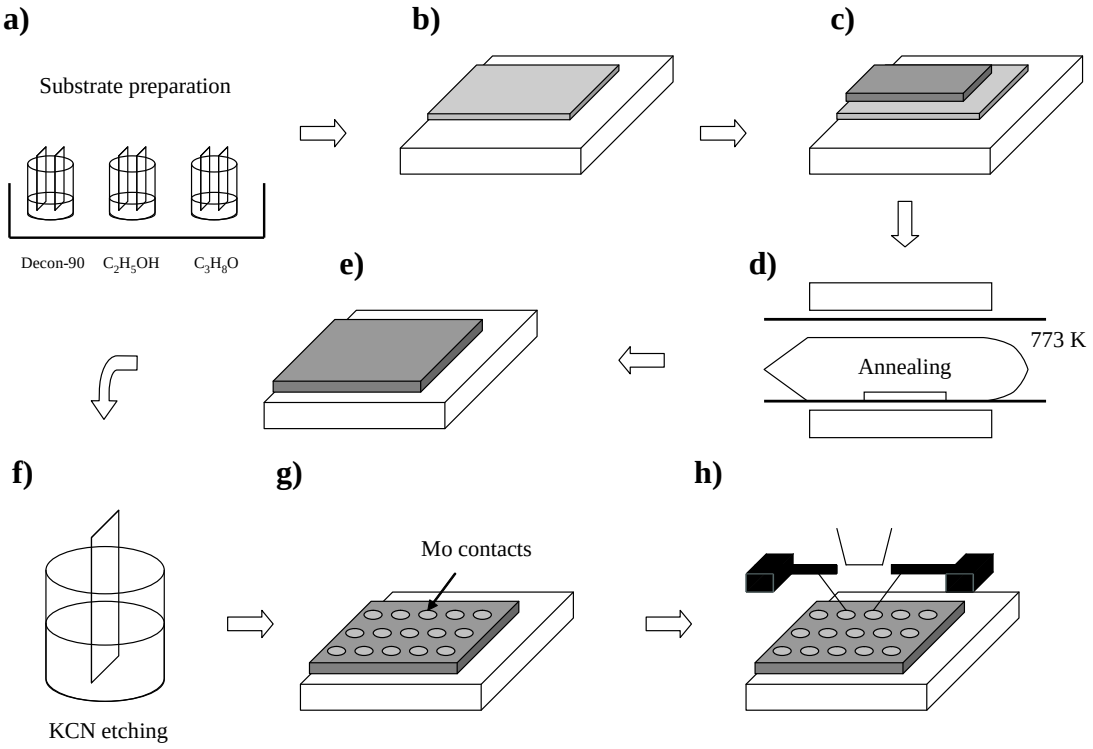

Figure 35: Complete fabrication and characterisation sequence for the synthesis of CZTS graded libraries.

8 Results and Discussion

This chapter presents results on the composition and phase analysis for the fully converted percursor metals after sulphursation for both the co-sputtered and stacked configurations following on from Chapter 6.

8.1 Characterisation of co-sputtered sulphurised CZTS libraries

8.1.1 Phase analysis and crystal structure

Figure 36 illustrates a selection of diffractograms relating to specific compositional ranges as listed in Table 16. It is clear the deviation from stoichiometry initiates peak shifting with varying intensity and the precipitation of additional crystalline metal-sulphur phases.

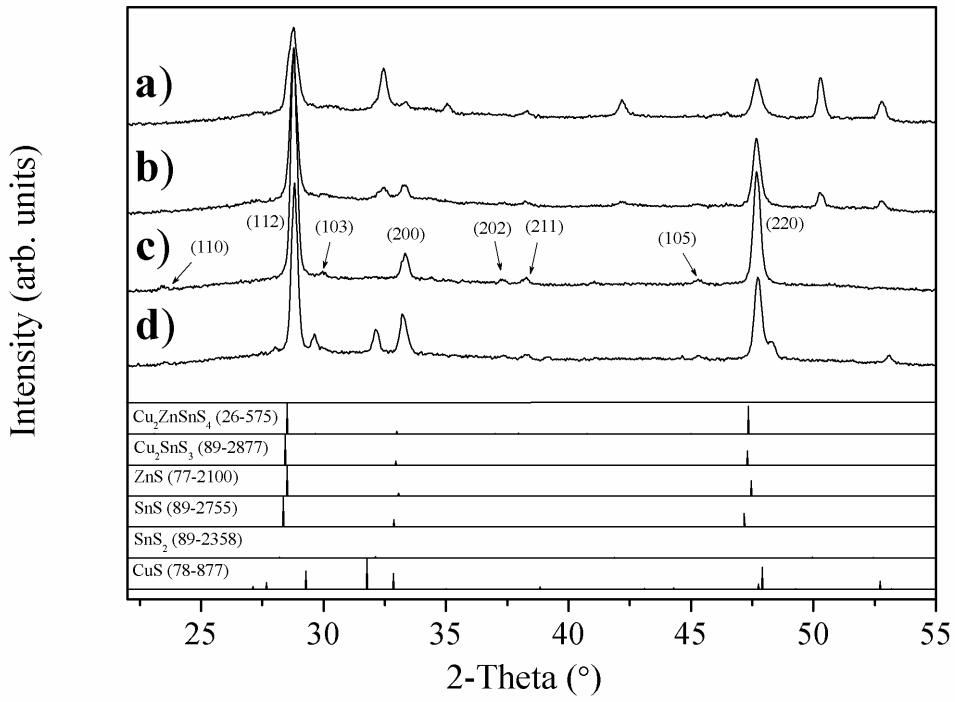

Figure 36: **Diffractograms of sulphurised co-sputtered precursor metals at 500 °C indicating the evolution of crystalline phases with respect to selected composition ratios Zn/Sn and Cu/(Zn+Sn), as given in Table 16. The Miller indices are associated with the kesterite structure.**

As previously pointed out, the three structurally similar phases Cu_2ZnSnS_4, ZnS and Cu_2SnS_3 all share overlapping peaks and thus are not easily distinguishable due to the limited resolution of the XRD measurement set-up. This is no coincidence particularly in a complex quarternary system as each phase represents a very small crystal change from the others with moderate changes in symmetry (and therefore space group). For this reason, several phases are present for a given composition and therefore neither can be ruled out. It should be noted that the compositions selected as listed in Table 16, do not correlate with the precursor ratios directly in Section 6.1.1 and are only for demonstrative purposes to show the most abrupt phase transformations.

Composition ratios				
	Precursor		**Sulphurised**	
Region	**Cu/(Zn+Sn)**	**Zn/Sn**	**Cu/(Zn+Sn)**	**Zn/Sn**
a)'	0.58	0.61	0.38	0.53
b)'	0.79	0.78	0.62	0.89
c)'	1.60	1.52	0.99	1.01
d)'	2.02	1.76	1.95	1.36

Table 16: **Summary of precursor and sulphurised composition ratios, Cu/(Zn+Sn) and Zn/Sn, corresponding to the selected diffractograms a) - d) in Figure 36.**

The change in peak intensity as a function of two different lateral scan lines across the library is shown in Figure 37. Figure 37a corresponds to the vertical scan line from high to low Sn concentration (and vice versa for Cu concentration), whereas Figure 37b depicts the horizontal scan line with respect to increasing Zn concentration. The near-stoichiomteric reference pattern (Cu/(Zn+Sn) ≈ 0.99; Zn/Sn ≈ 1.01) illustrates increased Bragg peaks 112 and 220, suggesting improved crystallinity with strong preferential orientation along these planes. There is a gradual decline in peak intensity as both Sn and Cu concentrations increase and decrease, respectively. As observed with the precursor libraries, the Zn concentration has a negligible impact on peak intensity. This observation is particularly encouraging such that Cu-poor and Zn-rich (Sn-poor) compositions yield the best crystallinity which ties in very well with improved power conversion efficiencies for CZTS devices as discussed in section 2.3.2. One reason could be that there is a greater number of phases possible

under Cu-rich/Zn-poor conditions (inducing Cu_xSn_y phases), whereas on the contrary a slight shift from stoichiometry to Cu-poor/Zn-rich conditions is favoured for the best kesterite crystallinity (as there are fewer possible phases that precipitate).

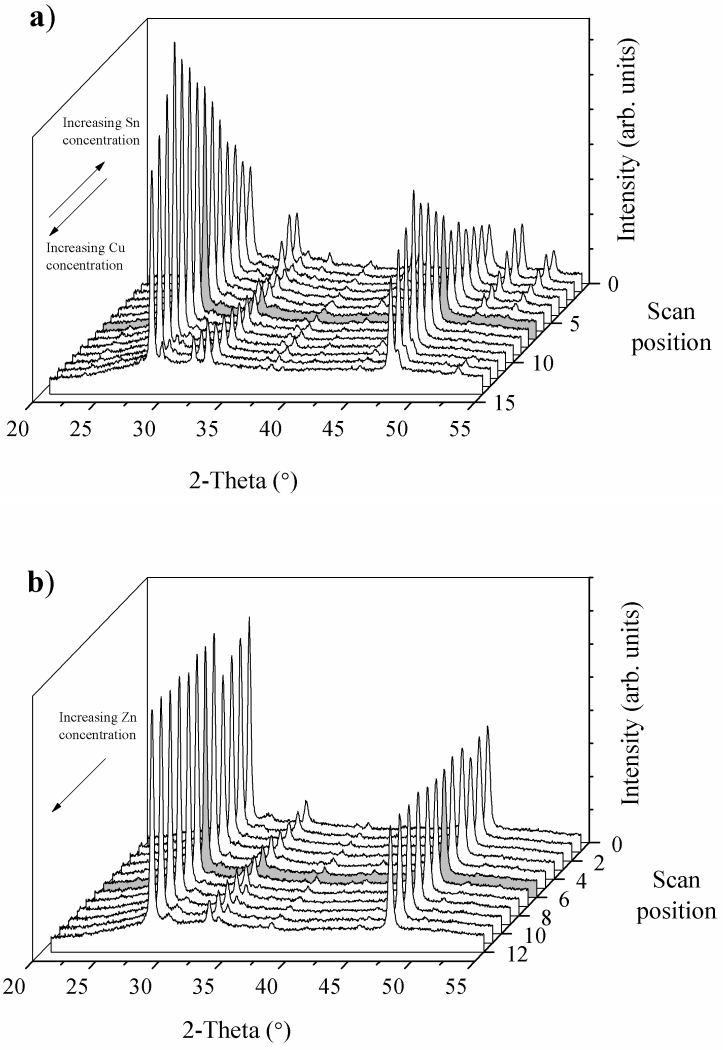

Figure 37: **Diffractograms with respect to position across the CZTS library: a) Change of Cu and Sn concentration, and b) change of Zn concentration. Shaded region indicates stoichiometric point (centre of library).**

Interestingly though, it is worth mentioning that the deposition of ideal Cu-Zn-Sn precursor film (ratio 2:1:1 - Cu/Zn+Sn = 1; Zn/Sn = 1) does not in this case yield a stoichiometric CZTS compound after sulphurisation. In fact, the precursor composition relating to diffractogram c) in Figure 36 has an initial composition ratio of Cu/(Zn+Sn) = 1.60 and Zn/Sn = 1.52, as summarised in Table 16. This

may suggest that in order to convert into a near-stoichiometric film, Cu-rich and Sn-poor (Zn-rich) compositions are favourable. It does, however, further suggest that the initial precursor composition undergoes elemental loss during the annealing stage when sulphur is incorporated. Although this would, however, need to be investigated further to draw up certain conclusions.

A quasi-ternary composition-phase diagram is constructed for the quaternary compound at 500 °C as displayed in Figure 38, which is based on the Cu_2S-ZnS-SnS_2 equilibrium phase diagram at 400 °C [97]. It should be noted that only the extraneous phases including SnS, SnS_2 and CuS (and all observed combinations) are labelled. The kesterite phase (Cu_2ZnSnS_4), ZnS and Cu_2SnS_3 are assumed to be present at each point and therfore not labelled individually. During the crystallisation process, the phase pure kesterite structure forms along the Cu_2SnS_3-ZnS line system within a small region as denoted by the intersection of the dashed lines. For this study, the co-sputtered CZTS library crystallises as a phase mixture within the investigated spatial region of the phase diagram. Only ternary copper-tin-sulphides, namely Cu_2SnS_3 (PDF #89-2877), are formed in the quasi-binary Cu_2S-SnS_2 system. Compound phases constituting Zn only form binary cubic-ZnS (PDF #77-2100), with no evidence of ternary formation in the quasi-binary ZnS-SnS_2 and Cu_2S-ZnS systems.

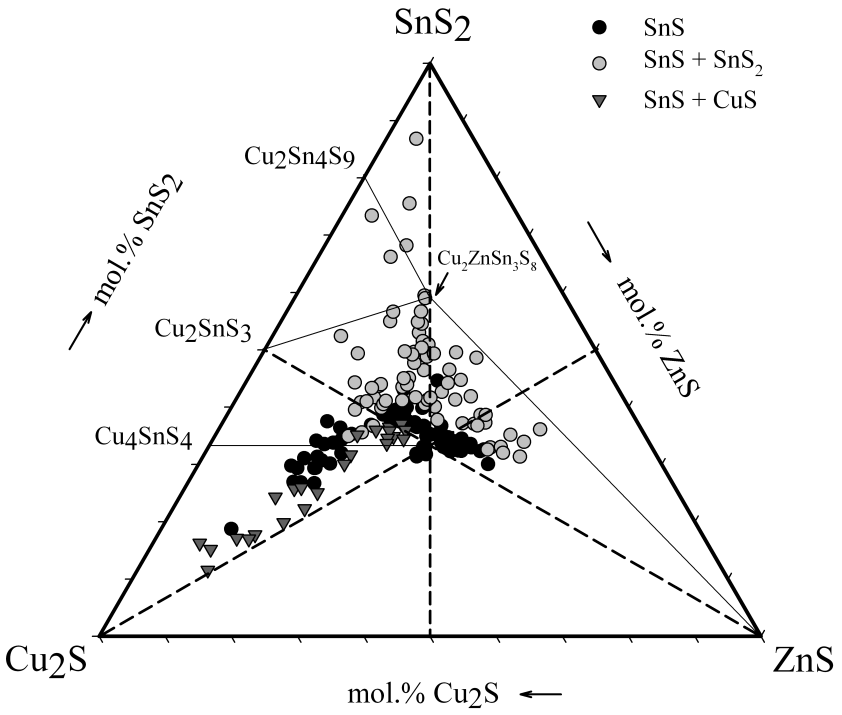

Figure 38: **Sulphurised phase-composition plot for the co-sputtered layer superimposed onto the quasi-ternary Cu_2S-ZnS-SnS_2 equilibrium phase diagram [91]. Intersection of the dashed lines denotes the stoichiometric precursor ratio (Cu:Zn:Sn =2:1:1). Cu_2ZnSnS_4, ZnS and Cu_2SnS_3 phases are assumed at each point.**

Studies by Shurr et al. [116] have reported that the deposition technique, sulphurisation conditions and precursor film thickness play an influential role in the reaction pathway leading to the formation of mono-phase CZTS. In this study, the binary phases CuS (PDF #89-2073) and SnS_2 (PDF #23-677) only occur at elevated Cu and Sn concentrations, respectively. Furthermore, there is evidence that the SnS (PDF #89-2755) phase forms in all regions of the phase diagram, in particular Sn-rich compositions, but it is difficult to ascertain whether this is the case or whether it simply coincides with the Bragg peak positions of Cu_2ZnSnS_4, ZnS and Cu_2SnS_3. Although the composition range is sufficient for the formation of the $Cu_2ZnSn_3S_8$ and Cu_4SnS_4 compounds, they do not form in this study. The new and unstudied quaternary compound $Cu_2ZnSn_3S_8$ as predicted by Olekseyuk et al. [97], is only expected to form at temperatures around 700 °C by the reaction of SnS_2 and Cu_2ZnSnS_4. This is potentially achievable if annealing temperatures were

increased, although the phases may not be thermodynamically stable when dealing with thin films. As for the ternary Cu_4SnS_4 phase not successfully forming, one feasible explanation is that the synthesis is initiated only by the presence of Cu_2S and Cu_2SnS_3. Experimentally, the binary Cu_2S has been shown to form due to the peritectic decomposition of CuS into Cu_2S and elemental sulphur at annealing temperatures reaching 510 °C [117]. The sulphurising process (temperatures $<$ 510 °C) employed for this study only causes the formation of CuS. There is no trace of Cu_2S suggesting that CuS is the most stable among the copper sulphides. Furthermore, this would seem ideal as Cu_4SnS_4 hinders the formation of CZTS [118]. As the Cu_2S and Cu_4SnS_4 phases cannot precipitate at these temperatures this would suggest that Cu-rich precursor material is preferred because there are fewer undesirable phases that can form. In this light, it should be noted that the quasi-ternary plot in Figure 38 indicates the vertex corresponding to the composition of Cu_2S (which would be expected at 400 °C under equilibrium) and not CuS as observed in this study. This is primarily adapted for illustrative purposes with respect to composition and not purely for phase identification.

As evidenced with the aforementioned XRD and EDS analyses, the crystallisation of CZTS as a phase mixture is highly probable and is strongly dependent on the initial precursor composition and annealing conditions. The binary phase Cu_2S is easily distinguishable with XRD and can be successfully removed via KCN etching although has some film quality implications as will be discussed later on in the chapter. However, the presence of kesterite CZTS, ZnS and Cu_2SnS_3 (and also SnS in this case) cannot easily be solely identified by XRD due to similar structural symmetries. One such solution as outlined in Section 7.3.2 is the combined use of XRD and complementary Raman spectroscopy will enable sufficient identification of the phase pure kesterite structure and any extraneous phases. Figure 39, together with Tables 17, 18 and 19, shows Raman scattering spectra as a function of composition for selected pre- and post-etched regions distributed across the co-sputtered library.

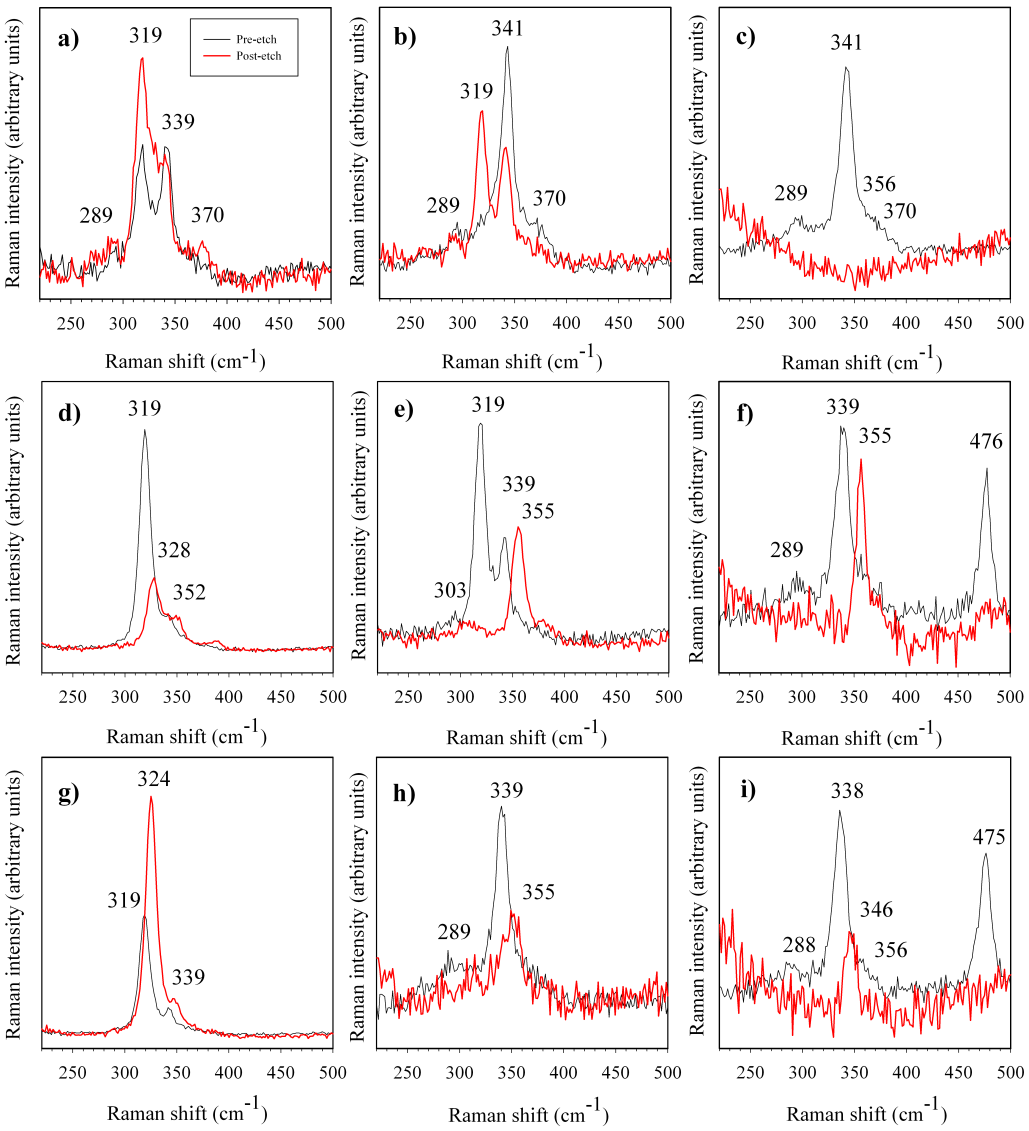

Figure 39: **Raman spectra collected from different regions across the co-sputtered CZTS library with respect to varying compositions, as listed in Table 17 (a - i). The graphs indicate spectra collected after sulphurisation (solid black) and post etching (solid red).**

Composition ratios				
	Sulphurised		Chemically etched	
Region	**Cu/(Zn+Sn)**	**Zn/Sn**	**Cu/(Zn+Sn)**	**Zn/Sn**
a)	0.29	0.84	0.14	2.96
b)	0.45	2.78	0.44	3.08
c)	0.61	2.94	-	-
d)	0.38	0.53	0.51	0.62
e)	0.99	1.01	0.80	1.04
f)	2.10	1.53	0.93	1.18
g)	0.18	0.12	0.39	0.27
h)	0.83	0.50	0.80	0.58
i)	1.30	0.68	0.92	0.65

Table 17: **Summary of sulphurised and post-etched composition ratios corresponding to the selected Raman spectra a) - i) in Figure 39.**

The most prominent Raman peak of kesterite CZTS is located at 338 - 339 cm^{-1} which is present in almost all regions, although there are minor shifts towards 341 cm^{-1} in these modes for regions b) and c) and varying intensity depending on the overall composition. Importantly, a second accompanying peak at 287 - 289 cm^{-1} associated with strong 338 - 339 cm^{-1} peak responses also arises. A further low intensity feature at 370 cm^{-1} is also likely attributable to kesterite. This confirms the successful crystallisation of CZTS under these growth conditions.

	Pre-etch
Region	**Raman shift (cm^{-1}) / Assigned phases**
a)	289 (CZTS), 319 ($Cu_2SnS_3 - orth$), 339 (CZTS)
b)	289 (CZTS), 341 (CZTS), 370 (CZTS)
c)	289 (CZTS), 341 (CZTS), 356 ($Cu_2SnS_3 - cubic$), 370 (CZTS)
d)	319 ($Cu_2SnS_3 - orth$), 352 (ZnS)
e)	319 ($Cu_2SnS_3 - orth$), 339 (CZTS), 355 ($Cu_2SnS_3 - cubic$)
f)	289 (CZTS), 339 (CZTS), 355 ($Cu_2SnS_3 - cubic$), 476 (CuS)
g)	319 ($Cu_2SnS_3 - orth$), 339 (CZTS)
h)	289 (CZTS), 339 (CZTS)
i)	288 (CZTS), 338 (CZTS), 356 ($Cu_2SnS_3 - cubic$), 475 (CuS)

Table 18: **Assigned phases to the observed Raman shifts prior to etching treatment, for each composition region of interest as in Figure 39.**

	Post-etch
Region	**Raman shift (cm^{-1}) / Assigned phases**
a)	289 (CZTS), 319 ($Cu_2SnS_3 - orth$), 339 (CZTS), 370 (CZTS)
b)	289 (CZTS), 319 ($Cu_2SnS_3 - orth$), 340 (CZTS)
c)	-
d)	328 (CZTS), 352 (ZnS)
e)	303 ($Cu_2SnS_3 - cubic$), 355 ($Cu_2SnS_3 - cubic$)
f)	355 ($Cu_2SnS_3 - cubic$)
g)	324 (CZTS), 339 (CZTS)
h)	355 ($Cu_2SnS_3 - cubic$)
i)	346 (CZTS)

Table 19: **Assigned phases to the observed Raman shifts post etching treatment, for each composition region of interest as in Figure 39.**

Detection of shoulder-like features within the wave number region 355 - 357 cm^{-1} and around 303 cm^{-1} are characteristic of the high temperature ($>$ 400 °C) cubic Cu_2SnS_3, however the intensities are particularly small which suggests this phase is not clearly present and/or the excitation wavelength is too short. Interestingly, there is no definitive evidence to show the formation of cubic ZnS (within the range 348 - 352 cm^{-1} and 275 cm^{-1} in order of decreasing intensity), although these shifts would be in the vicinity of the Cu_2SnS_3 peaks making it difficult to distinguish. Irrespective of whether Cu_2SnS_3 and ZnS can independently be identified, the Raman technique consolidates the presence of the kesterite structure crystallising under these synthesis conditions. Surprisingly, the intensity of the 338 cm^{-1} mode is relatively low in the near-stoichiometric region (Zn/Cu $\approx$ 1.01 and Cu/(Zn+Sn) $\approx$ 0.99) and is completely dominated by a strong 319 cm^{-1} peak associated with the orthorhombic Cu_2SnS_3 phase suggesting unsuccessful reaction (or partial reaction) into the kesterite phase. The SnS and SnS_2 binaries as identified by XRD are only detectable at a lower wavenumber range (namely between 160 and 219 cm^{-1} for SnS, and 215 and 314 cm^{-1} for SnS_2 [119]), thus cannot be confirmed using this Raman set up. Once the library is subjected to KCN etching, the expected CuS phase at 475 - 477 cm^{-1} is eliminated but in some instances the film quality deteriorates substantially or the film de-laminates as demonstrated by the "noisy" post-etch response in Figure 39c. This is further consolidated as demonstrated from the SEM images in the following section of different compositional spaces across the library before and

after KCN etching in Figures 42 and 43, respectively. Furthermore, chemical treatment causes the kesterite structure to completely diminish in certain regions leaving behind only secondary and/or ternary phases, in particular ZnS and Cu_2SnS_3. The etching conditions would need further experimentation for complete optimisation in order to reduce the deterioration of the film (indicative by the changes in peak intensity).

Special attention should be paid to the depth capability provided by the Raman excitation wavelength and the overall quality of the film which may significantly vary undermining the identification of any existing peaks. Estimations by a previous study [109] have concluded that using a wavelength range of 488 - 633 nm would penetrate the CZTS film by approximately 140 - 170 nm, thus in this instance only a fraction of the 1.5 μm layer would be interrogated. This analysis could suggest that both CZTS and CuS form within the upper region of the layer, which is particularly evident in Cu-rich conditions. Without a comprehensive analysis of the complete film depth, it is unclear whether this is holds true.

The lattice parameters a and c, and unit cell volume, V, of CZTS libraries were obtained from the XRD data and calculated using a graphics based profile fitting program known as TOPAS. This program uses Rietveld analysis to fit X-ray diffractograms with precision when the crystal structures of each phase are known. It has been found that the lattice parameters, a and c, are in moderately close agreement as reported in Table 14 of single crystal measurements. In fact, both values are slightly higher than most reported in the literature [120] and show a clear correlation with changing Cu content, as shown in Figure 40.

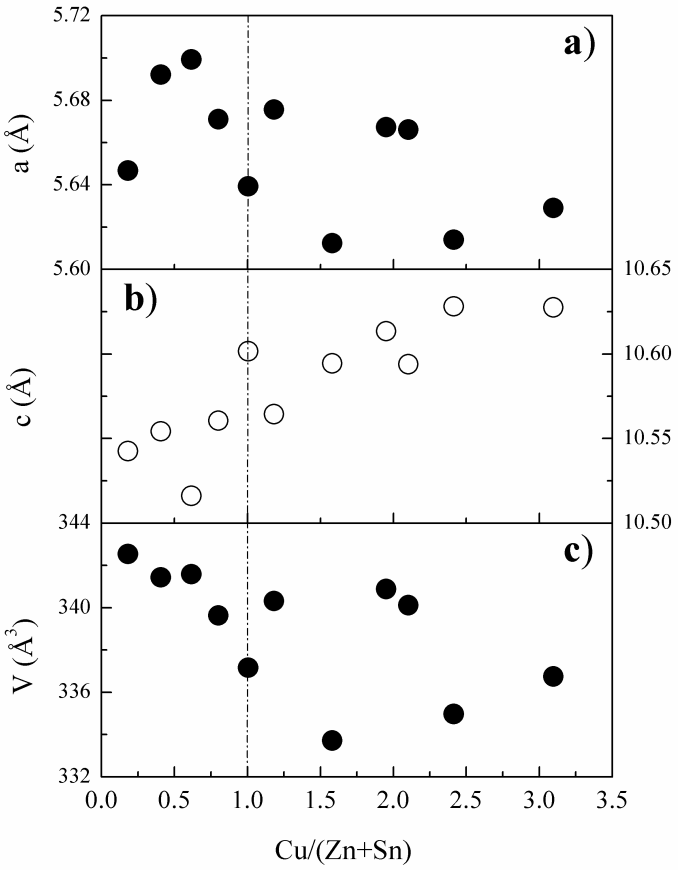

Figure 40: **Lattice parameters a and c, and the unit cell volume V, as a function of Cu/(Zn+Sn). The dashed line indicates the stoichiometric region (Cu/(Zn+Sn) = 1).**

The lattice parameter a shows a general decline in value with increasing Cu/(Zn+Sn) ratio values, whereas parameter c shows a clear increase. The unit cell, V, also shows a decrease in value. A recent study by Trimmel et al., who synthesised stoichiometric CZTS crystals by heating metal salts and thioacetamide, observed a moderate change in lattice parameters with respect to different annealing temperatures and found that at lower temperatures ($<$ 250 °C), both a and c increased leading to an expansion of the unit cell [118]. This was attributable to cation disorder within the CZTS material. The changes in this study can be attributed to compositional changes, rather than processing conditions. A study by Bonazzi et al. showed very similar results although, the unit-cell volume V increased linearly with increasing Zn concentration rather than Cu as in this research [119]. A further in-depth study

is required to fully ascertain the reason associated with the change in values.

8.1.2 The effects of sulphurisation and etching on film morphology and composition

An RBS spectrum was obtained from the near-stoichiometric point of the sulphurised co-sputtered library as shown in Figure 41 to confirm the composition

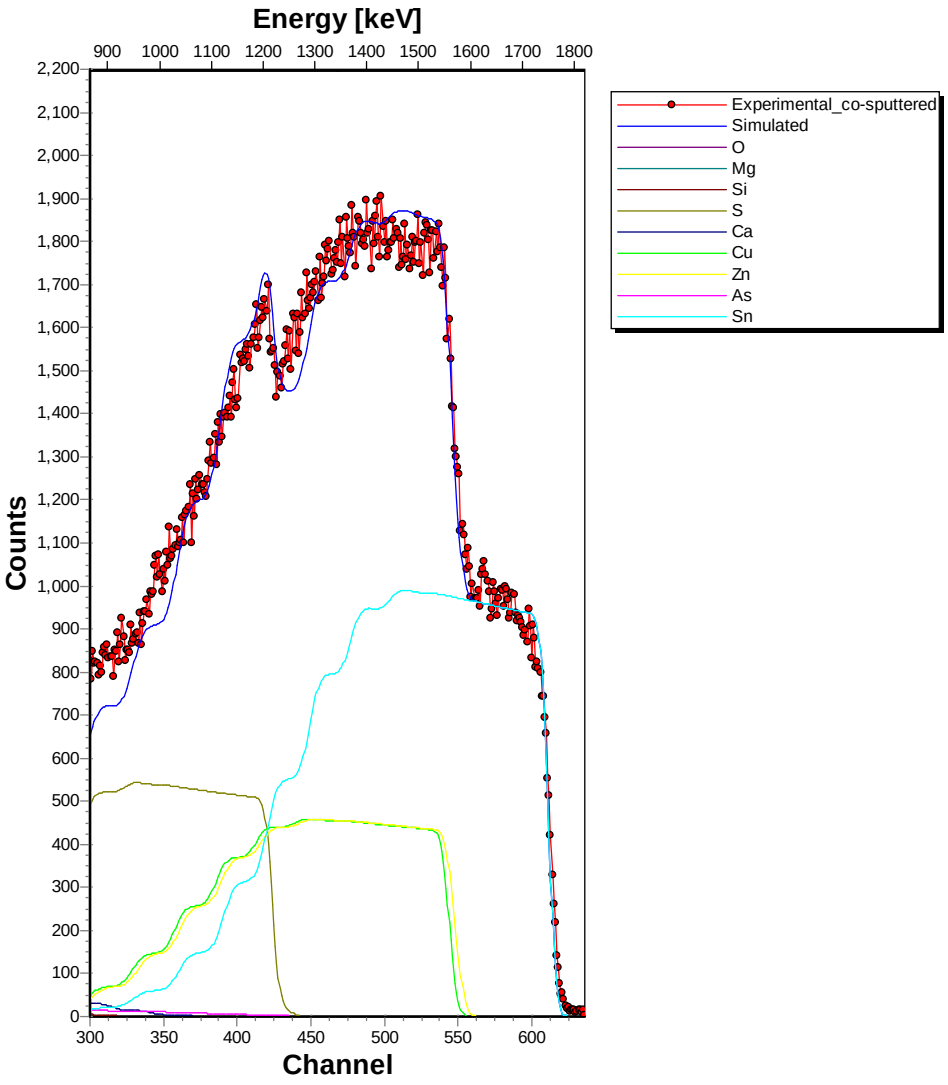

Figure 41: **RBS spectrum of a co-sputtered CZTS layer onto glass (near-stoichiometric region of library). The sample structure and the thicknesses of the layers (in atoms/cm ^{2}) are shown in Table 20.**

The model is summarised in Table 20 and shows a Cu- and Sn-poor (slightly

	Concen. (at. %)				t, (10^{15} atoms/cm^2)
Layer	**Cu**	**Zn**	**Sn**	**S**	**CuZnSnS**
1	23	13	11	53	4200
Total	$\mathbf{Cu_{23}Zn_{13}Sn_{11}S_{53}}$				**4200**
R_S, (10^{15} atoms/cm^2)					**2200**

Table 20: **Summary of RBS parameter's obtained from the SIMNRA simulation model: elemental atomic concentration (at. %); layer thickness, t (10^{15} atoms/cm^2); and surface roughness, R_S (10^{15} atoms/cm^2).**

Zn- and S-rich) film. The film thickness is approximately twice as thick as the deposited precursor layer (2220 x 10^{15} atoms/cm^2) which is satisfactory since the sulphur layer is twice as thick as the precursor layer when initally deposited. There is no variation with depth factored into the RBS simulation model. However, there is clear indication of the complete intermixing of all elements indicating a homogeneous film with respect to depth, but it is likely that there will be material loss during the annealing process as mentioned previously. The surface roughness is significantly larger confounding highly accurate RBS measurements.

In figure 42, SEM images are shown of morphological characteristics corresponding to different compositions: Cu-rich, near stoichiometric and Sn-rich. There was little change in the morphology with respect to the variation in Zn content and therefore was excluded from this study. Within Cu-rich regions, as in Figure 42a, there are many distributed CuS crystallites on the film surface varying in size typically in the range of 2 - 10 μnm. The near-stoichiometric region (Figure 42b) shows large surface features that could be attributed to the excess sulphur as confirmed from the RBS analysis. The Sn-rich region on the other hand, shows smaller and more compact grains. Upon treating the samples in chemical etchant as shown in Figure 43, many of the CuS crystallites are removed successfully as expected, although the quality of the film either delaminates and/or deteriorates substantially leaving behind large void-like features and surface cracks. Many regions of the film experience substantial stress-induced de-lamination. This effect was noticed with the Raman measurements in Figure 39. The near-stoichiometric and Sn-rich show almost identical surface topographies.

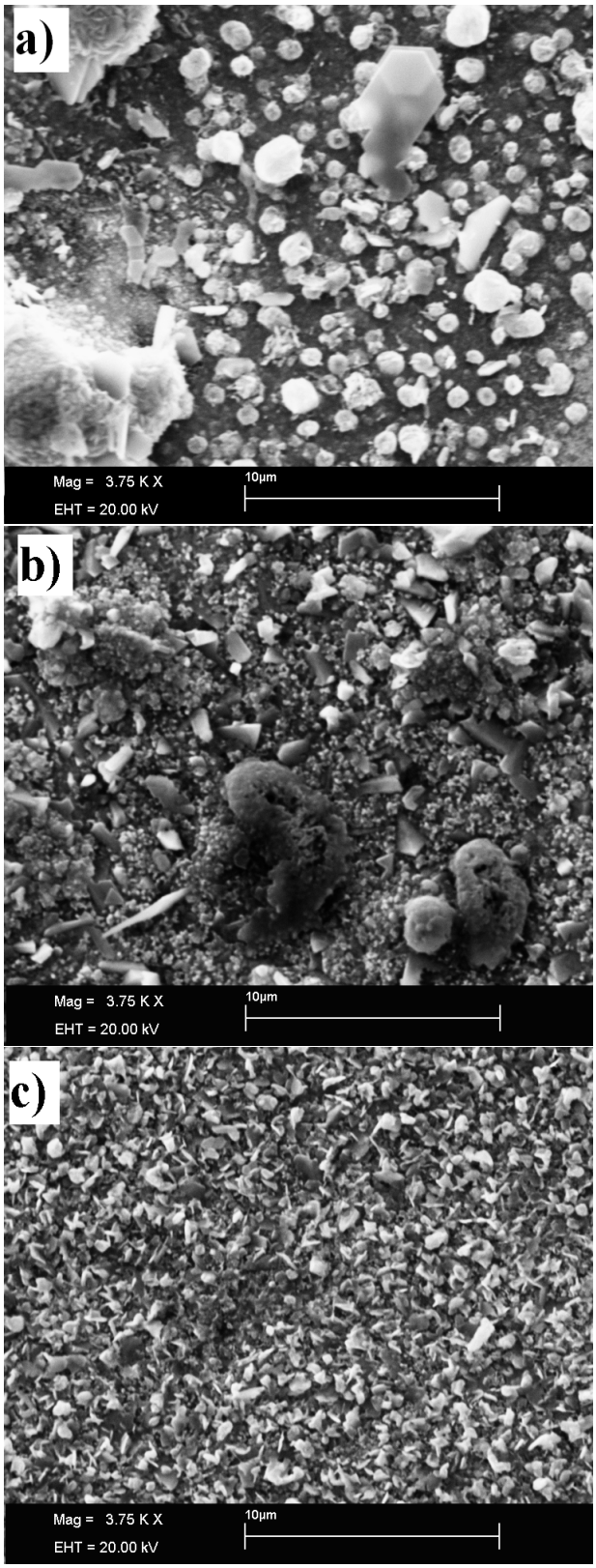

Figure 42: **Surface SEM micrographs of sulphurised co-deposited precursors: a) Cu-rich, b) near-stoichiometric, c) Sn-rich.**

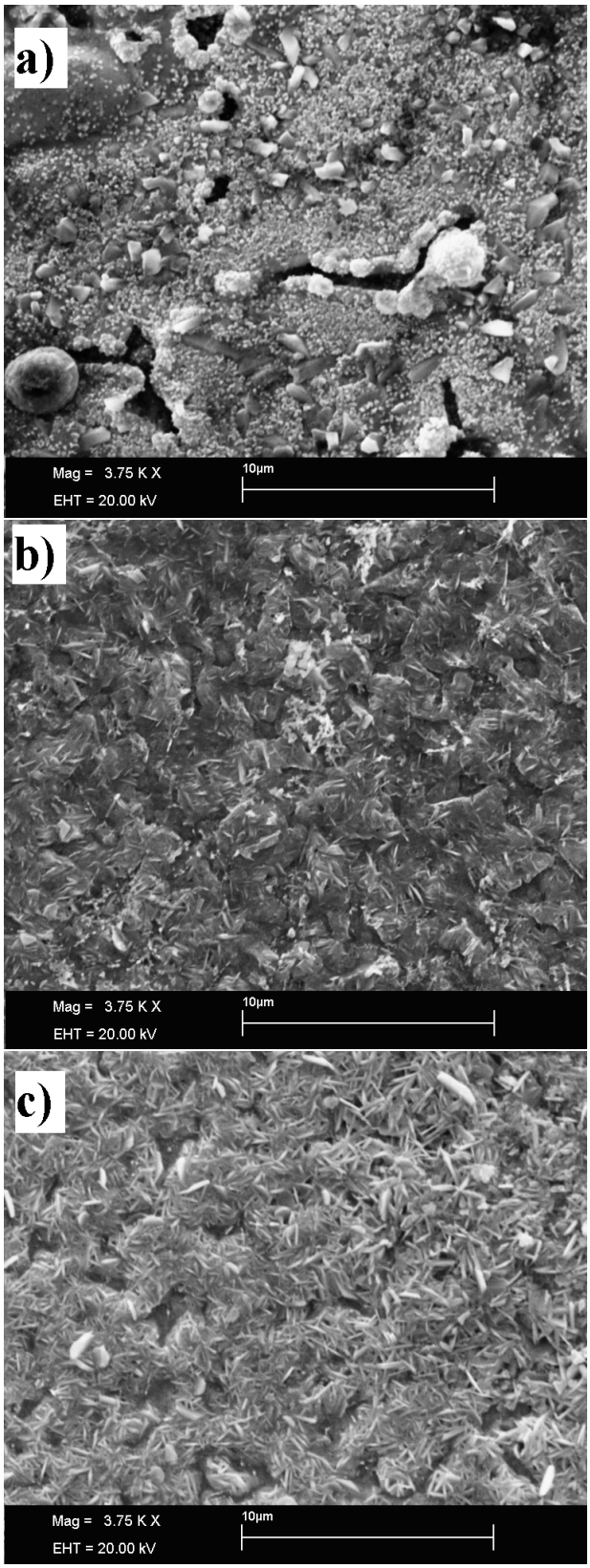

Figure 43: **Surface SEM micrographs of co-sputtered CZTS post-etching treatment: a) Cu-rich, b) near-stoichiometric, c) Sn-rich.**

8.2 Sulphurised stack order: precursor sequence Sn/Cu/Zn

8.2.1 Phase analysis and crystal structure

This section evaluates the properties of the crystal structure of the Sn/Cu/Zn stacked CZTS library. Figure 44 shows very similar diffractograms as with the co-sputtered library.

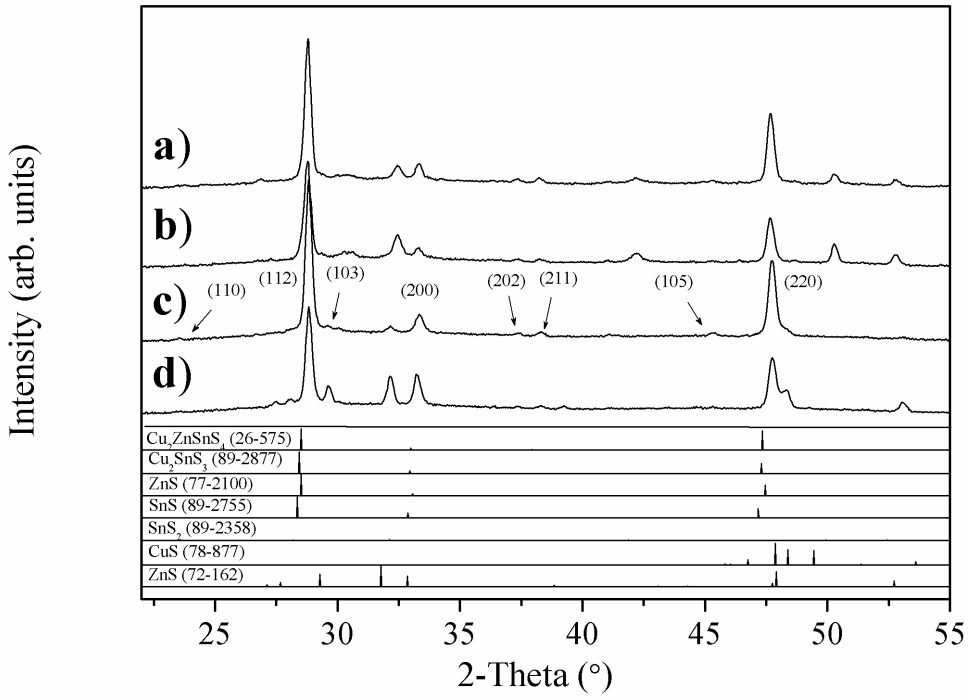

Figure 44: **Diffractograms of sulphurised stacked (Sn/Cu/Zn) precursor metals at 500 °C indicating the evolution of crystalline phases with respect to selected composition ratios Zn/Sn and Cu/(Zn+Sn), as given in Table 21.**

Composition ratios				
	Precursor		Sulphurised	
Region	Cu/(Zn+Sn)	Zn/Sn	Cu/(Zn+Sn)	Zn/Sn
a)	0.36	0.56	0.61	0.76
b)	0.75	0.65	0.87	0.91
c)	0.73	0.68	1.01	1.03
d)	1.34	1.22	1.54	1.09

Table 21: **Summary of precursor and sulphurised composition ratios corresponding to the selected diffractograms a) - d) in Figure 44.**

In Figure 45, the peak intensity changes are less drastic compared to those observed with the co-sputtered library, but are at their highest at near-stoichiometric compositions. Again the Zn concentration has little effect on the structure of the film.

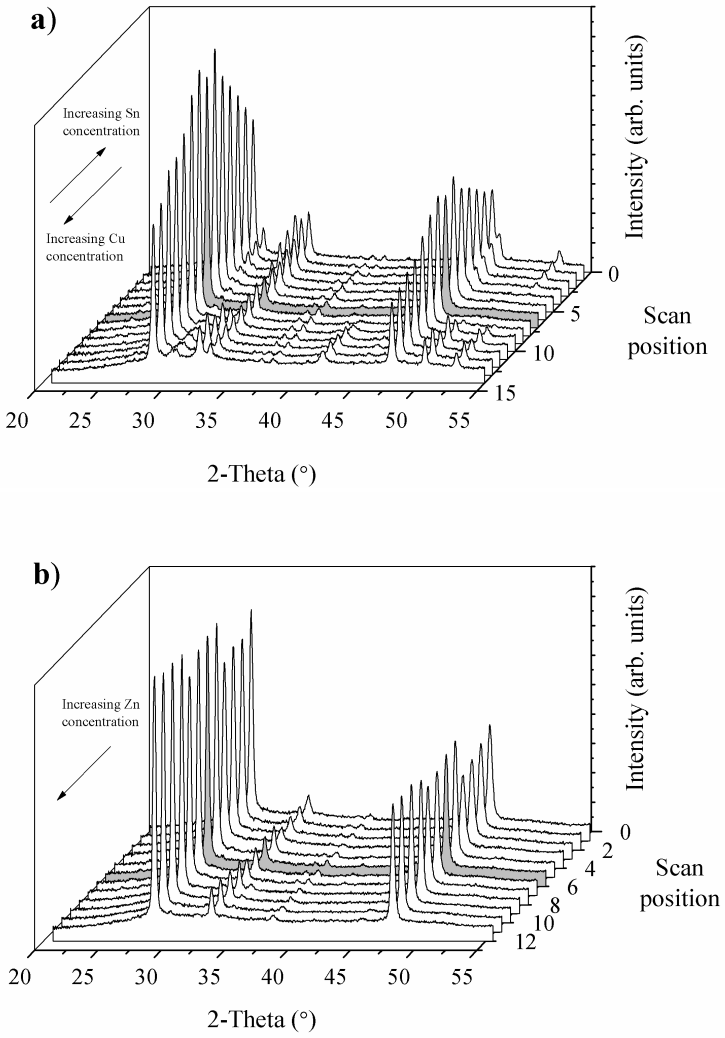

Figure 45: **Diffractograms with respect to position across the CZTS stacked library: a) Change of Cu and Sn concentration, and b) change of Zn concentration. Shaded region indicates stoichiometric point (centre of library).**

One distinct change compared to the co-sputtered library is the presence of an additional ZnS (PDF 72-162) phase as shown in Figure 44. The formation of this additional ZnS crystal structure would, however, require a further in depth investigation. Figure 46 shows collectively all of the points acquired across the

stacked library as quasi-ternary phase diagram.

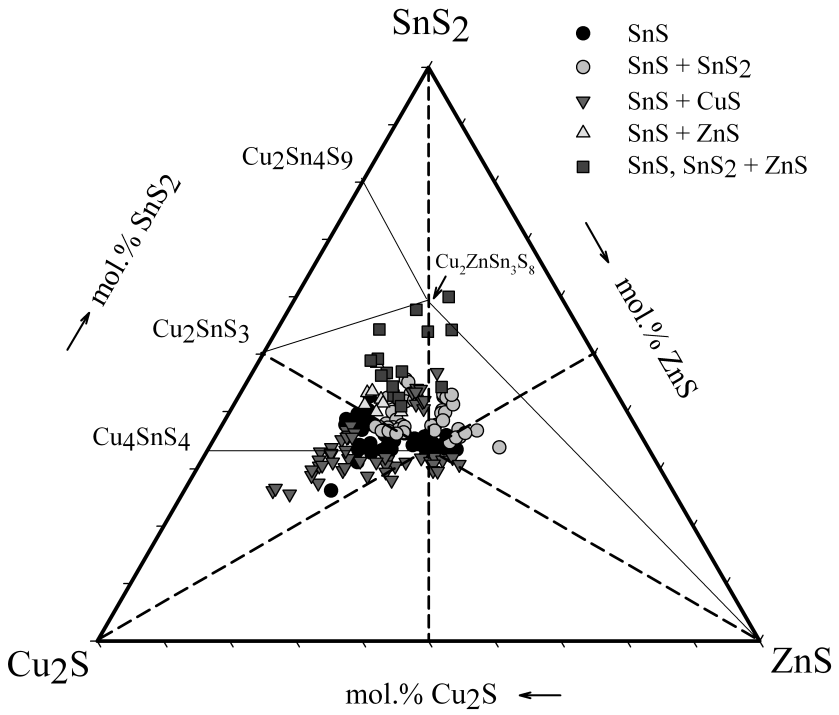

Figure 46: **Sulphurised phase-composition plot for the Sn/Cu/Zn stacking order superimposed onto the quasi-ternary Cu_2S-ZnS-SnS_2 equilibrium phase diagram [91]. Intersection of the dashed lines denotes the stoichiometric precursor ratio (Cu:Zn:Sn =2:1:1). The kesterite Cu_2ZnSnS_4, ZnS and Cu_2SnS_3 phases are assumed at each point.**

8.2.2 The effects of sulphurisation and etching on film morphology and composition

The point of near-stoichiometry is assessed by RBS as illustrated in Figure 47 and Table 22. Elemental ratios and thickness values are very similar to the co-sputtered film, although stacking proves to yield a much smoother film. This may be inherent with the stacking configuration as each layer is grown sequentially with sufficient control in thickness, hence allowing successive nucleation of atomic layers. It was mentioned previously that there was no depth variation in the RBS simulation for the co-sputtered CZTS library

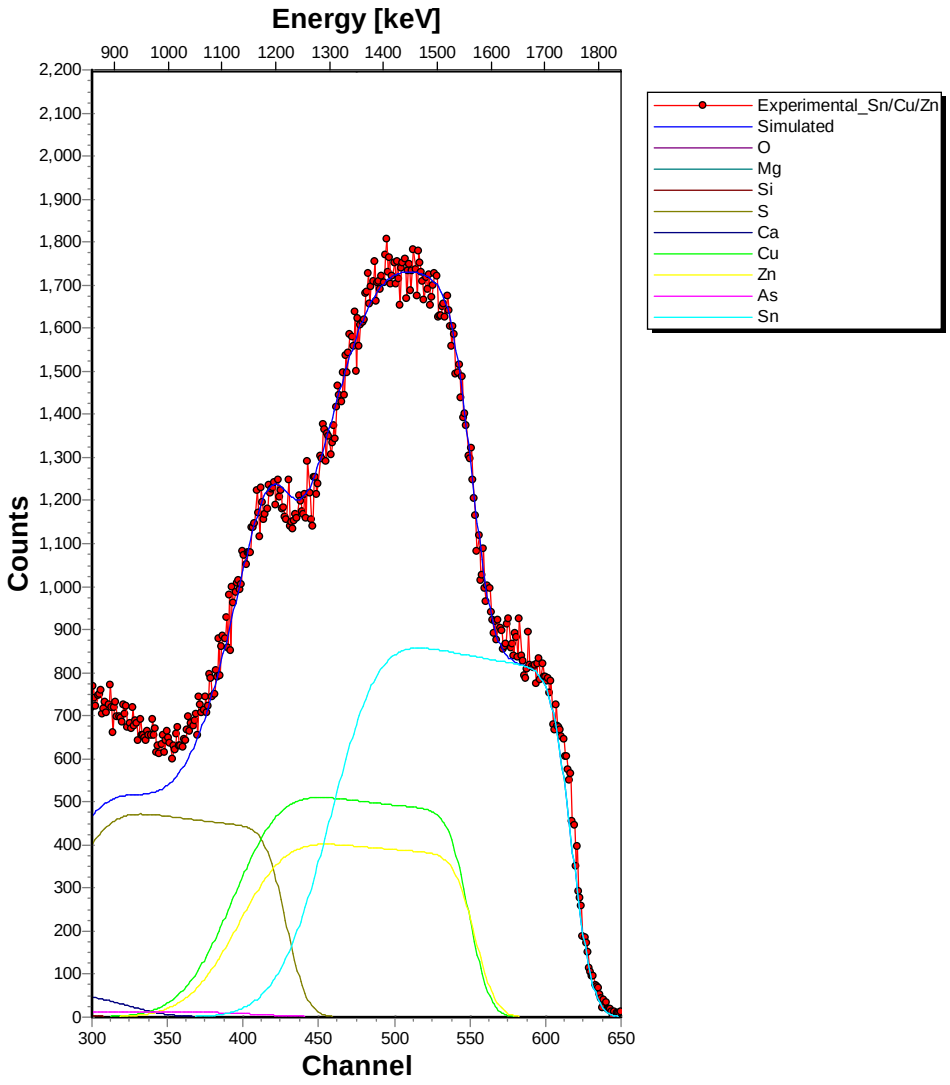

Figure 47: **RBS spectrum of the stacked CZTS layer onto glass (near-stoichiometric region of library). The sample structure and the thicknesses of the layers (in atoms/cm ^{2}) are shown in Table 22.**

	Concen. (at. %)				t, (10^{15} atoms/cm^2)
Layer	**Cu**	**Zn**	**Sn**	**S**	**CuZnSnS**
1	22	14	11	53	4530
Total	$Cu_{21}Zn_{15}Sn_{11}S_{53}$				4530
R_S, (10^{15} atoms/cm^2)					1123

Table 22: **Summary of RBS parameter's obtained from the SIMNRA simulation model: elemental atomic concentration (at. %); layer thickness, t (10^{15} atoms/cm^2); and surface roughness, R_S (10^{15} atoms/cm^2).**

Again, large CuS crystallites (> 5 μm) are evident in the Cu-rich region as shown in Figure 48a. The region of stoichiometry shows improved morphology, although it does present some holes and roughness. The Sn-rich region, interestingly, shows dentrite-like crystals growing on the surface of the film. Upon etching, as in Figure 49, The Sn-rich regions shows clear "crater-like" features appearing on the surface after chemical treatment. This would suggest the presence and collapse of liquid Sn during the annealing and recrystallisation process of the film. This was noticed in [98], where bubble like features are present in the bottom region of the film exposing the underlying substrate.

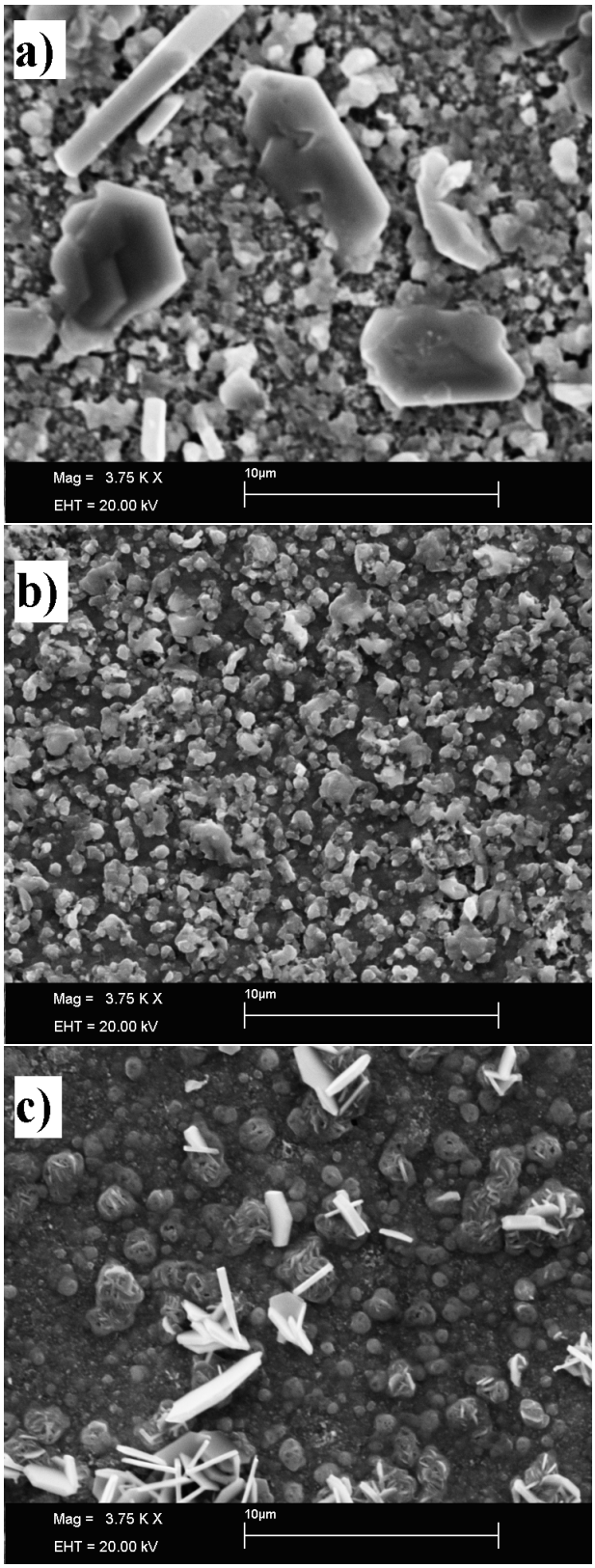

Figure 48: **Surface SEM micrographs of Sn/Cu/Zn stacked CZTS after sulphurisation: a) Cu-rich, b) near-stoichiometric, c) Sn-rich.**

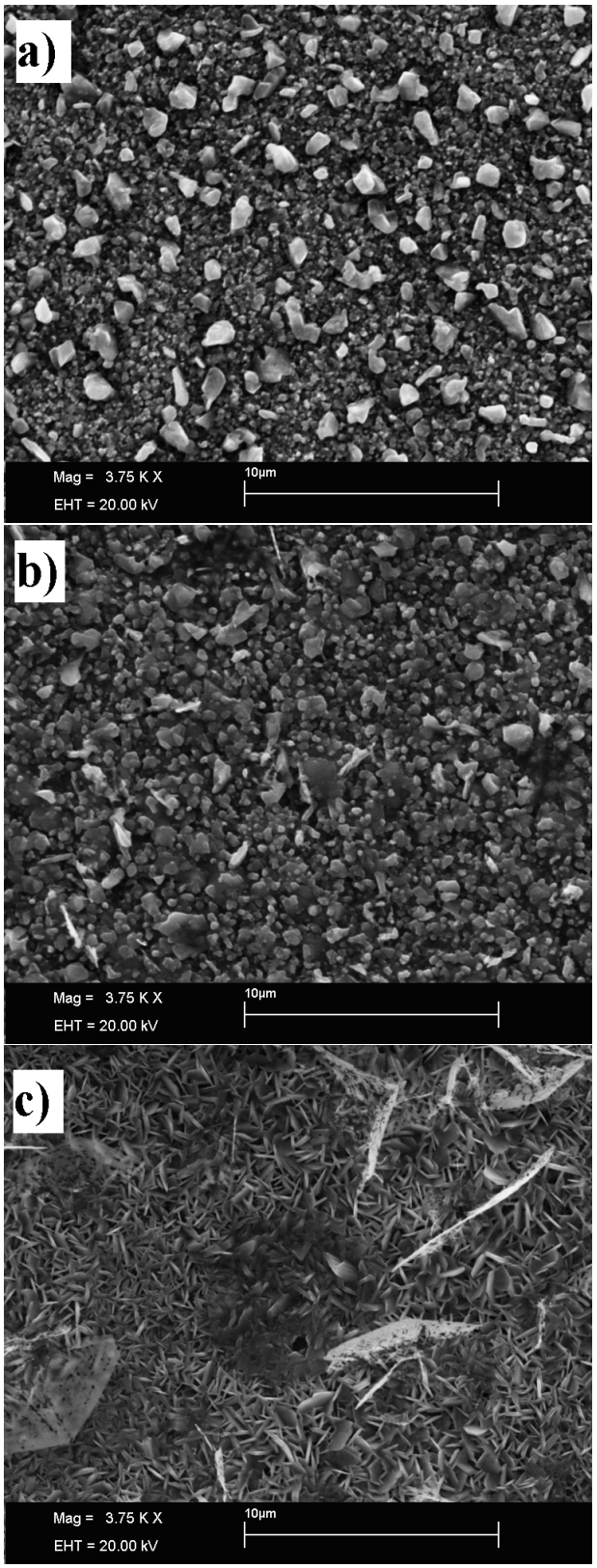

Figure 49: **Surface SEM micrographs of Sn/Cu/Zn stacked CZTS post-etching treatment: a) Cu-rich, b) near-stoichiometric, c) Sn-rich.**

8.3 Conclusions relating to fully sulphurised percursor metals

To conclude, this chapter has shown the successful growth of CZTS libraries using a co-sputtered and a discrete stacking (with different ordering of elements) approach. Interestingly, some stacking configurations were not successfully synthesised into the semiconductor layer as outlined in the following subsection.

8.3.1 Sulphurised stacking orders: Cu/Zn/Sn and Sn/Zn/Cu

The stacking orders Cu/Zn/Sn and Sn/Zn/Cu experienced little success during the sulphurisation process in terms of adhering to the underlying substrate. In fact, much of the material was lost during the annealing process, thus no measurements could be obtained. At this stage, the findings can only be based on the stacking order effect, but it is likely that there are many intertwining factors contributing to this behaviour. A very brief discussion on some of the possible explanations as to why this may have occurred and why these deposition configurations are unsuitable for the fabrication of CZTS layers is given.

Some studies have concluded that the characteristics of CZTS-based thin films using stacked precursor metals are strongly dependent on the stacking orders in the precursor thin films. Yoo et al. [120] RF-sputtered precursor metals with varying stacking orders and subsequently sulphurised the films at 570 °C. They found, interestingly, that the glass/Mo/Sn/Zn/Cu and glass/Mo/Cu/Zn/Cu/Sn configurations possessed substantially more voids than other stacking orders. They postulated that the reason for the first precursor configuration is the separation of Cu and Sn by Zn. When Cu is not adjacent to Sn, it is difficult to form Cu_2SnS_3 which is a fundamental reactant in order to produce CZTS with ZnS. This seems a sensible explanation for the glass/Sn/Zn/Cu configuration in this study. Furthermore, and perhaps surprisingly, a multi-layer stack of 12 thin layers (Sn/Zn/Cu order repeated three times) was purposely adopted to initiate intimate mixing of the metallic elements prior to sulphurisation, but this does not seem to occur as one might expect particularly at low deposition temperatures. In the second instance, it is believed that Cu at the bottom of the stack creates void-like features via "Cu-migration" to the upper surface (Kirkendall-type mechanism of vacancy diffusion) [121]. This again, can ex-

plain the behaviour of the second Cu/Sn/Zn configuration. Thus, we can conclude to some extent that the deposition of the precursor metallic system is crucial to the understanding of the growth mechanics and importantly how this relates to the overall quality of CZTS film layers. It should be noted that not all combinations of layered CZTS structures were discussed in this chapter and are referred to briefly in the appendix only.

8.3.2 XRD and Raman phase analysis

A comprehensive and systematic study into crystal growth and phase identification of co-sputtered and stacked CZTS libraries has been carried out using the powerful and non-invasive XRD and Raman analytical techniques. A discussion on the difficulty associated with identifying the desired kesterite structure with other extraneous phases such as ZnS, SnS and $Cu_2SnS_3$with XRD alone has been outlined. The use of Raman confirmed the presence of the kesterite structure post-sulphurisation with dominant peaks arising at 338 - 339 cm^{-1}. Importantly, which is also well documented in CZTS literature, is the accompanying peaks at 287 - 289 $cm^{-1}$and 370 cm^{-1} of lower itensity which consolidates the crystallisation of the kesterite structure. This was evident for both the co-sputtering and stacked library configurations, although the similar Raman results for the stacked library are not presented in this thesis. Even though the presence of kesterite has been confirmed, accurately separating ZnS from the terary Cu_2SnS_3 proves somewhat more challenging but some Raman spectra collected for certain composition regions have shown that orthorhombic Cu_2SnS_3 is likely to be the more dominant phase occurring at 319 cm^{-1}. Binary CuS and SnS_2 can be confidently confirmed with XRD but distinguishing the SnS phase with Raman poses further problems such that a lower wavenumber range between 160 and 219 cm^{-1} is required. It is clear from these results that although the kesterite structure forms under these synthesis conditions using a two-stage approach, it is difficult to ascertain whether ZnS, SnS and Cu_2SnS_3 are also present The desired CZTS kesterite structure has been confirmed by XRD and Raman measurements to crystallise under these synthesis conditions. Achieving phase pure kesterite, however, remains a challenge. Interestingly, some

8.3.3 Proposed model for CZTS growth

An investigation into the reaction kinetics in one particular study [116] for CZTS formation shows that at a temperature of 500 °C a 2 μm thick evaporated kesterite layer, which are similar conditions to this study, should be rapidly synthesised within a short timeframe in the order of tens of seconds. This may hold true in this instance, but with the evaporated sulphur 'cap' used for this investigation prior to heating, it is likely sufficiently longer annealing times are required to accommodate the prolonged sulphur incorporation into the deposited metallic precursors. One concern, as already addressed, is phase segregation during sulphurisation with respect to film depth. This will almost certainly be related to a combination of factors including the initial precursor composition and configuration, the method of incorporating the sulphur during the reaction and the annealing conditions. Based on the observed phases forming from both XRD and Raman analyses, it is likely that elemental precursors initially react with the present chalcogen to form binary compounds such as SnS_x, ZnS and CuS prior to the complete conversion of CZTS. It may be possible to predict and adapt the reaction process(s) for the synthesis of kesterite CZTS as postulated theoretically by Herbert and Hock [122]. It follows two simultaneous solid state reaction processes, with the first being a single step (equation 15) and the second via a dual assisted route (equation 16, then 17) with the ternary CTS and binary ZnS forming CZTS compound forming:

$$2CuS(s) + ZnS(s)(cubic) + SnS(s)(-SnS(s) + SnS_2(s)) \rightarrow Cu_2ZnSnS_4(s)(+\frac{1}{2}S_2(g)) \quad (15)$$

$$2CuS(s) + SnS(s)(-SnS(s) + SnS_2(s)) \rightarrow Cu_2SnS_3(s)(cubic)(+\frac{1}{2}S_2(g)) \quad (16)$$

$$Cu_2SnS_3(s)(cubic) + ZnS(s)(cubic) \rightarrow Cu_2ZnSnS_4(s) \quad (17)$$

Further studies are required in order to clarify whether the CZTS is formed by reaction of SnS_2 and/or SnS or whether SnS is only a decomposition product. The reaction pathways correlate well with both the XRD and Raman data for all compo-

sition regions studied across the phase diagram. It is also worth mentioning to what extent the sulphurisation conditions play in the final phase formation. Only a finite quantity of elemental sulphur, albeit in excess, is introduced and enclosed within the ampoule. If a substantial amount of sulphur is consumed during the reaction process of CZTS, which is expected, the sulphur vapour pressure will continue to decrease in conjunction to the onset of the irreversible decomposition of CZTS. So it is important to consider the following conditions during the film growth: the optimum quantity and vapour pressure of sulphur, the maximum annealing temperature and the overall duration of the reaction process. Under a low sulphur vapour pressure estimated at ≈ 2 mbar and a relatively long anneal time of 30 minutes for this study, it may be that the binary SnS_x and CuS compounds undergo sublimation due to having a low evaporation limit causing poor film adhesion and fracture/void structures. A recent study by Momose et al. [30], using similar deposition techniques for the formation of a 1.4 μm thick CZTS film, reported on the relationship between sulphur pressure and sulphurisation conditions. They found that in order to avoid the re-evaporation of binary phases such as CuS and SnS_x and thus the formation of voids, a rapid thermal heating approach under high sulphur vapour pressures ($\approx$ 1.5 atm) is beneficial. In fact, longer annealing times with a low vapour pressure was detrimental to film quality and overall solar cell efficiency.

9 Opto-electronic and electrical properties

9.1 Room temperature photoconductivity

Photoconductivity (PC) was realised in 1873 by W. Smith [123] who observed a decreasing change in resistivity of photoconductive selenium when illuminated with incident monochromatic light. The process in its simplest terms can be described as the intrinsic absorption of photons with energy greater than the band gap, E_g, that create mobile charge carriers (electron and holes in the conduction and in the valence bands, respectively). Hence, there is an increase in the conductivity of the material.

Enhanced conductivity can further originate extrinsically caused by the presence of doped impurities or imperfections. In this instance, electrons from the impurity atoms are excited to the conduction band and contribute to the conduction process. However, the required ionisation energy is very small thus low temperatures are needed which is not a requirement for intrinsic processes [124].

This chapter reports on the spectral characteristics of the photoconductive response of CZTS thin films at room temperature. Some correlations between the photoconductivity characteristics, composition and film structure are also established.

9.1.1 Basic concepts of photoconductivity

The photoconductivity gives very useful information about the fundamental opto-electronic properties of a semiconductor material. The following calculations are based on a homogeneous semiconductor under normal AM1.5 illumination conditions for solar cells.

The intrinsic conductivity σ, is given by:

$$\sigma = e(p\mu_p + n\mu_n) \tag{18}$$

where p (holes) and n (electrons) are the carrier concentrations, μ_p and μ_n are the carrier mobilities, and e is the electronic charge. An increase in the carrier

concentrations, μ_p and μ_n, gives a change in photoconductivity $\Delta\sigma$, such that:

$$\triangle\sigma = e(\triangle p\mu_p + \triangle n\mu_n) \tag{19}$$

The photocurrent generated can be assumed to be proportional to both $\Delta\sigma$ and to the field intensity (if small in magnitude), if the distribution of charge carriers remain homogenous [125].

9.1.2 Metal-semiconductor contacts

In order to measure the photoconductive properties of any material, it is almost a prerequisite to use electrodes that form an ohmic contact with the semiconductor sample. Ideal electrodes should be chemically inert, allow complete flow of current (no resistance in either direction), and unaffected by variations in illumination and temperature. However, from a practical viewpoint, this has proved very difficult for many material systems especially in the case of new compounds.

The choice of material contact will ultimately govern which barrier is formed between the semiconductor-metal interface. In the case of a *p*-type semiconductor, such as CZTS and CIGS, an ohmic contact is obtained if the work function of the metal φ_m, is greater than that of the host semiconductor, φ_s. The reverse scenario will induce an undesirable rectifying barrier. A voltage applied across the metal-semiconductor interface will be mainly concentrated at the barrier and not across the specific volume of semiconductor due to the highly resistive barrier. Thus, in order to make photoconductivity measurements, such barrier contacts should be avoided. It should be further noted that the presence of surface states on the semiconductor itself may also contribute to creating an intrinsic surface barrier prior to any contact with a metal [126].

With this criterion in mind, molybdenum (Mo) is selected as a metal contact to the CZTS surface for this study. Molybdenum is by far the most common metal currently used for back contacts in CIS, CIGS and CZTS device structures. This is primarily due to its higher work function ($\varphi_m > \varphi_s$) thus suitable for many *p*-type thin film absorber layers. Furthermore, its stability at processing temperatures in excess

of 500 °C, excellent adhesion and durability properties and resistance to alloying with Cu, In, Zn and Sn is also advantageous. It has been realised experimentally that Mo forms an ohmic contact via the formation of a thin intermediate MoS_2 layer formed at high temperatures during the CZTS and CIGS deposition [127]. However, the work of Shafarman et al. [128], who analyzed the Mo/CIS interface separately from the solar device, shows the contact to be ohmic. Although this setup is very different to the back contact configuration i.e. no high annealing temperatures are required, it would still therefore seem sensible in this case to use Mo contacts for the photoconductivity experiments. Whether this is entirely the most suitable material to use would require a further and comprehensive investigation.

9.1.3 Band gap measurements

A curve of photoconductivity versus energy (or wavelength) has a distinctive profile: it begins with a level region at higher energies before rising to a maximum peak prior to the absorption edge. Finally, the response decreases exponentially through the band gap at lower energies. In this study, the theorem' proposed by Moss [129] is used to calculate band gap energy values. The sensitivity S(E) is assumed to vary due to the distribution of energy levels in the valence band from which the electrons come from, and is given by:

$$S(E) = \frac{1}{1 + \exp\{\beta\,(E_0 - E)\}} = \frac{1}{2} \tag{20}$$

where E is the energy of the incoming radiation, E_0 is a threshold energy and β is a constant. From this model, the optical band gap energy E_g is determined from the spectral photoresponse curve at that point where the sensitivity exponentially falls to half its maximum value.

There are many techniques used to detect photoconductivity but all of them are reliant on several fundamental factors: experimental setup and instrumental noise; the preparation of the sample surface; semiconductor thickness and importantly the contact material and configuration. When a photosignal is weak, it can be separated from the dark current by modulating a light signal and further amplified using a

phase-sensitive amplifier. A lock-in amplifier is essentially a filter with an arbitrary narrow bandwidth tuned to the chopping frequency. This filter will prevent most unwanted noise to allow the signal to be measured. The experiment requires a set frequency in a relatively quiet part of the noise spectrum, thus the lock-in can then detect the response in a very narrow bandwidth at that excitation frequency. In this case, a mechanical chopper is used to square-wave modulate the intensity of optical signals. An important consideration is which frequency to select and it is worth noting that conventional symmetrical square modulation of radiation relies on the fact that the duration of incident light on the sample needs to be sufficient to allow for the photocurrent to attain its steady state. Too high a frequency will cause a weak photosignal to be detected. Thus, for this investigation a frequency of 27 Hz is selected. A study based on photoconductivity effects in CdTe crystals used similar values at 25 Hz [130].

9.2 Experimental method

9.2.1 Library and contact preparation

All libraries underwent KCN etching prior to photoconductivity measurements. An array of equally spaced and 1 μm thick Mo ohmic spot contacts were subsequently sputtered directly onto the sample surface using a stainless steel template as illustrated in Figure 50 below.

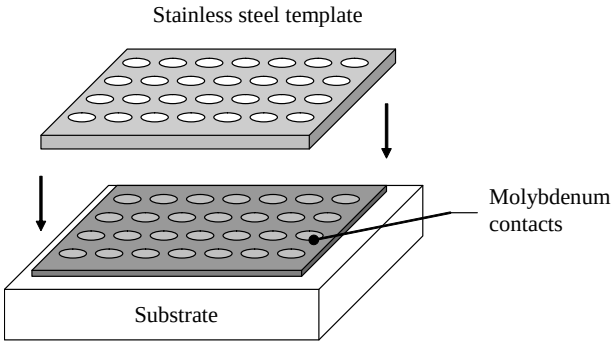

Figure 50: **Masking configuration used to sputter molybdenum ohmic contacts in preparation for photoconductivity measurements.**

When depositing Mo layers typically via sputtering, film stress plays a large role

in determining the quality and overall properties. Films deposited under tensile stress have good adhesion but high resistivity. Under compressive stress, however, the opposite effect occurs. The adhesion of Mo films to the substrate and the sheet resistivity is highly dependent on the sputter deposition conditions. The relationship between the microstructure and stress of Mo films under different sputtering conditions are well established. Salome et al. [131] reported on an in-depth investigation into the effects of sputtering conditions on Mo coatings and how a bilayer structure can yield sufficient properties of good adhesion and low resistivity (and hence higher conductivity). They concluded that optimal conditions were achieved by depositing a single first layer (around 500 nm) at roughly 10 x 10^{-3} mbar and then a second layer deposited at 1 x 10^{-3} mbar with a thinner nominal thickness of 300 nm. Reported results indicated a sheet resistivity between 0.5 and 0.8 Ω with excellent adhesion on soda lime glass. For this study, a similar approach was taken whereby Mo contacts were deposited on top of the CZTS absorber layer. The calibration data for the Mo target is presented in the Appendix section. In general the Mo films sputter-deposited at low process pressures tend to be dense, having low resistivity and compressive stress. As the Ar process gas pressure increases, the film stress switches from being compressive to tensile. The conditions for the Mo contact deposition in preparation for the measurements are summarised in Table 23. When sputtering the 800 nm thick bilayer, the bottom layer is deposited first at 10 x 10^{-3} mbar and subsequently changed to 4 x 10^{-3} mbar. This was left for approximately five minutes to stabilise prior to sputtering the second top layer. Film thickness is monitored in-situ using a QCM.

Layer	Power (W)	Rate (nm/s)	Gas pressure (10^{-3} mbar)	Thickness (nm)
a	200	0.521	10	100
b	200	0.567	5	700

Table 23: **Deposition conditions used to sputter the molybdenum bilayer structure composing of two single layers, *a* and *b*.**

9.2.2 Photoconductivity measurements

The light source, monochromator and optics are described in this section. Light from a 100 W tungsten halogen lamp was directed into a 1/8m monochromator (Oriel, Cornerstone) with exit slits equivalent to 15 nm bandwidth, and coupled into a bifurcated quartz fibre bundle. This directed half of the beam onto a reference silicon photodiode, with the remaining light focused onto the library surface via a mechanical optical chopper (Stanford Research, SR540 - 6/5 slot blade) operating at 27 Hz. The photocurrent resulting from an applied constant voltage supply of 9 V was detected by a phase-sensitive lock-in amplifier (Stanford Research, SR510) and normalised to the output of the reference photodiode measured using a Keithley 2000 digital multi-meter. Instrumentation and data acquisition were controlled and fully automated by LabView software [132]. All equipment was housed within a Faraday cage to elininate ambient light and external noise interference. The experimental set up is schematically shown in Figure 51.

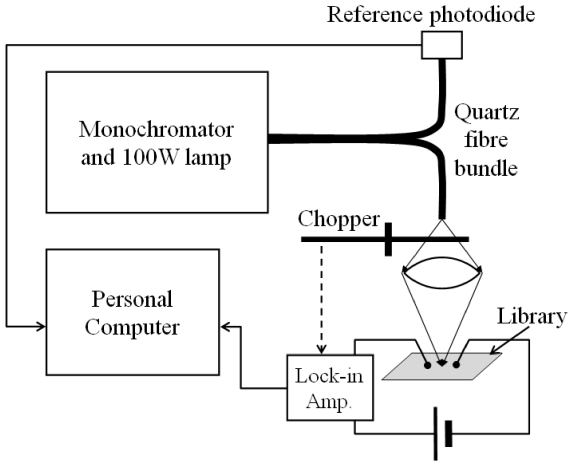

Figure 51: **Experimental setup for room temperature photoconductivity measurements.**

The time constant of the Lock-in amplifier was set just sufficient to give an acceptable signal to noise ratio of the output. For any time constant, the wavelength scan rate of the monochromator was chosen so not to produce undue relative lag of output signal to wavelength. The photoconductivity spectral response was normalized per photon at each wavelength as measured with a calibrated silicon detector.

Spectral dependence of the photoconductivity was measured under light illumination in the spectral region 400 - 1100 nm. The spectral dependence of the lamps intensity is shown in Figure 52a.

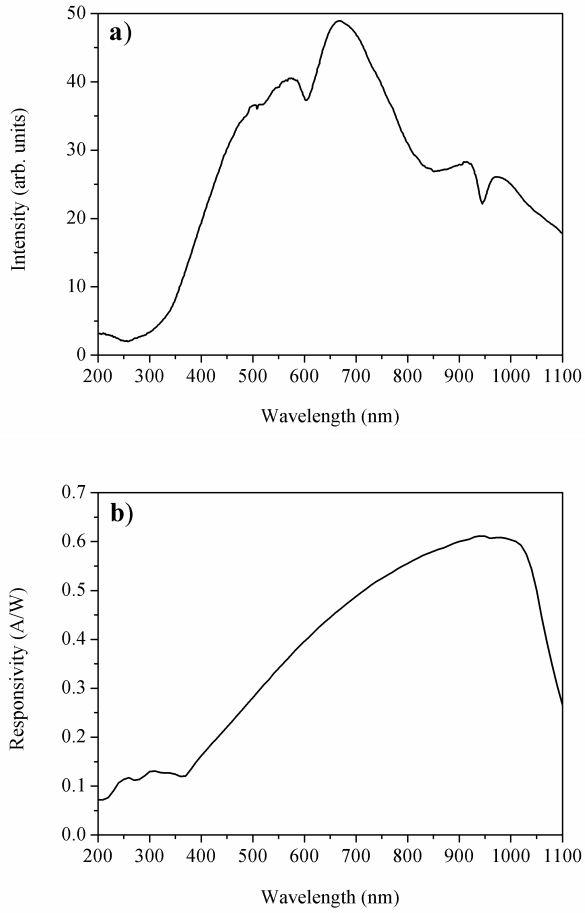

Figure 52: **Experimental setup: a) Lamp output intensity as a function of wavelength, and b) Responsivity of the silicon photodiode detector as a function of wavelength (without any external attenuator).**

The set up used in this study uses a specific measurement technique. The reponsivity of the photodiode, R_{PD}, as shown in Figure 52b, is given by:

$$R_{PD} = \frac{I_{PD}}{\triangle P} \tag{21}$$

where $\triangle P$ is the power and I_{PD} is the measured photodiode current. Also, the change in conductivity $\triangle\sigma$ of a solid can be given by:

$$\triangle\sigma = \frac{\triangle I}{E} \tag{22}$$

where $\triangle I$ is the change in Lock-in current. Dividing the two equations (21 and 22) and rearranging such that:

$$\frac{\triangle\sigma}{\triangle P} = \frac{\triangle I}{EI_{PD}}(R_{PD}) \tag{23}$$

This is essentially the photocurrent that will be measured. The curve associated with the photoconductivity response as a function of the energy is fitted with an inverse tangent function and the band gap measurements are made in accordance with the Moss criterion.

9.2.3 Results and Discussion

This section reports on the photoconductivity results collected at room temperature for the synthesised CZTS libraries after KCN chemical etching. The photoconductive response (taken to have arbitrary units) variation with respect to photon energy (eV) is presented for both the co-sputtered and stacked (with varying orders) configurations.

1. Photoductivity measurements: co-deposited CZTS libraries

Photoconductivty measurements of the co-sputtered library are illustrated in Figure 53 as a function of selected compositional ratios across the sample. These compositions, as represented by the ratios Cu/(Sn+Sn) and Zn/Sn, are chosen to give an overall insight into the highest and lowest performing material and how this is related to the changes from Cu-poor/Zn-rich to Cu-rich/Zn-poor. The region of near-stoichiometry is also included as a reference much like the phase analysis in previous chapter's. The highest photoconductive response arises from curve a) associated with Zn-rich and Cu-poor compositions (Zn/Sn = 2.96 and Cu/Zn+Sn = 0.49) which is substantially higher than that of the near-stoichiometric and the Cu-rich/Zn-poor region. Band gap energy values as summarised in Table 24 range from 1.42 - 1.53 eV for the absorber layer which are ideal for solar cell applications.

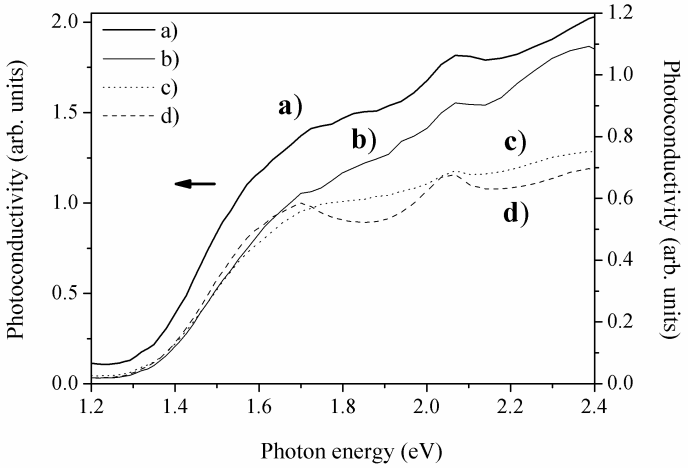

Figure 53: **Spectral dependence of room temperature photoconductivity with respect to four different compositions (a-d) across the co-sputtered library (as listed in Table 24).**

Composition			
Sample	**Zn/Sn**	**Cu/(Zn+Sn)**	**Estimated E_g, (eV)**
a)	2.96	0.49	1.48
b)	1.21	0.67	1.50
c)	1.02	0.97	1.51
d)	0.97	1.103	1.49

Table 24: **A list of the highest performing compositions across the co-sputtered CZTS library, as measured with the photoconductivity set up. An estimated band gap value is also given.**

2. Photoductivity measurements on a stacked CZTS library: order Sn/Cu/Zn

Similarly, photoconductivity measurements on the stacked configurations were also taken under the same conditions. For the library with precursor order glass/Sn/Cu/Zn as shown in Figure 54, a very similar pattern emerges such that the highest response (and hence the best performing composition) is associated with Zn-rich/Cu-poor regions with a gradual decline towards Zn-poor/Cu-rich compositions as listed in Table 25. An important point to note is that the overall magnitude of the response(s) is less than that as observed with the co-sputtered library.

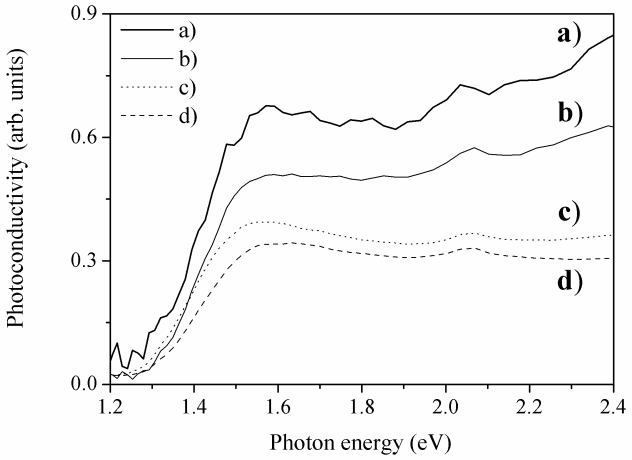

Figure 54: **Spectral dependence of room temperature photoconductivity with respect to four different compositions (a-d) across the Sn/Cu/Zn stacked library (as listed in Table 25).**

Composition			
Sample	**Zn/Sn**	**Cu/(Zn+Sn)**	**Estimated E_g, (eV)**
a)	1.21	0.56	1.43
b)	1.14	0.76	1.41
c)	1.05	0.98	1.38
d)	0.75	1.08	1.42

Table 25: **A list of the highest performing compositions across the Sn/Cu/Zn stacked CZTS library, as measured with the photoconductivity set up. An estimated band gap value is also given.**

3. Photoductivity measurements on a stacked CZTS library: order Zn/Sn/Cu

Although the evaluation of the CZTS library with stacking order glass/Zn/Sn/Cu has been somewhat excluded from this thesis but some of the composition and phase analysis results are collated in the Appendix section. However, the opto-electronic properties as obtained from the photoconductivity setup yield some very interesting results which is worth bringing to light and mentioning in this section. Figure 55(a) - (d) illustrates the photoconductive response curves which are all associated with varying degrees of Zn-rich/Cu-poor ratios as well as near-stoichiometric as a reference (Table 26). Of particular interest is the intensity of the photoconductivity response curves compared to all other sample libraries which are some degrees of

magnitude higher.

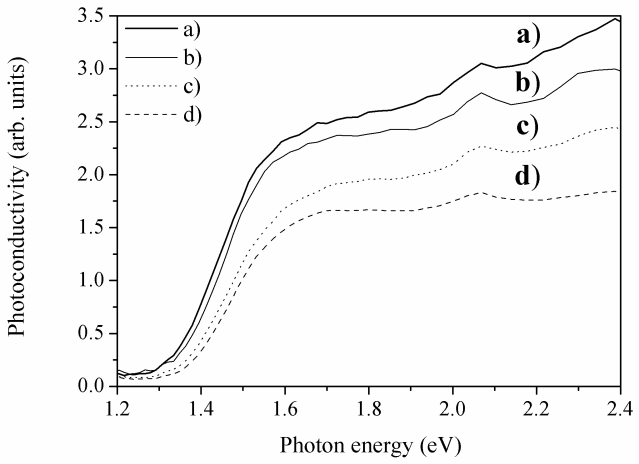

Figure 55: **Spectral dependence of room temperature photoconductivity with respect to four different compositions (a-d) across the Zn/Sn/Cu stacked library (as listed in Table 26).**

Composition			
Sample	**Zn/Sn**	**Cu/(Zn+Sn)**	**Estimated E_g, (eV)**
a)	2.43	1.32	1.43
b)	1.76	1.12	1.46
c)	1.54	1.03	1.43
d)	1.04	0.96	1.47

Table 26: **A list of the highest performing compositions across the Zn/Sn/Cu stacked CZTS library, as measured with the photoconductivity set up. An estimated band gap value is also given.**

For all results, the spectra show similar behaviour in terms of the shape of the curves but distinct changes in the magnitude of the photoconductive response. Furthermore, there is also a gradual shifting from the onset of the absorption edge. The cut-off in all curves can be assigned to the electronic band gap energy, E_g, and is determined by using the Moss criterion as described. All measured band gaps exhibit values close to the expected CZTS value of 1.5 eV [23-25], which is optimal for high performing solar cell operation. The photoresponse and the band gap are clearly dependent on the final elemental composition of the CZTS material. In general, as the ratio Zn/Sn increases and Cu/(Zn+Sn) decreases a higher response in photoconductivity is observed. The highest performing library was the stacked

Zn/Sn/Cu configuration closely followed by the co-sputtered. On the other hand, the stacked library with precursor order glass/Sn/Cu/Zn, showed particularly poor spectral response values in comparison. However, it must be noted that poor photoconductive results are not solely reliant on the compositional nature of samples. Other factors to take into account are inconsistent ohmic contacting and/or the uncertainty in the band-gap value extrapolation. Electrical and optical properties have been extensively studied for CZTS absorber material [133, 135], as well as the photoconductivity technique which has recently been explored yielding positive results [134]. To the authors knowledge there is no published literature based on room temperature photoconductivity using this particular experimental arrangement.

9.3 Electrical measurements: hot point probe

9.3.1 Basic concept of the hot point probe

The widely used hot point probe technique provides a simple, rapid and efficient way to determine whether a semiconductor sample is either n- or p-type.

The physics behind the concept is relatively straightforward and can be categorised into a three-step mechanism process as follows:

1. The application of thermal energy is required to excite the free charged carriers by attaching a hot and cold probe to a semiconductor surface. The hot probe is connected to the positive terminal of an eletrometer while the cold probe is connected to the negative terminal.

2. A temperature gradient causes a diffusion process of the excited majority carriers to begin from the heated electrode to the cooler electrode (due to there being a lower density of hot carriers at the cooler region). As a consequence, a built-in electric field is created and a voltage readout can be obtained. This is called the thermoelectric or Seebeck effect. The electrical potential sign of the measured voltage is governed by the majority carriers. For instance, in an n-type semiconductor there would be a positive voltage readout indicating the majority carriers are electrons, and for a p-type a negative readout is obtained (majority carriers are holes). The semiconductor material itself and the cooler

electrode begin to warm up over time preventing the diffusion process. This is known as the steady state [136, 137].

3. The steady state will continue until the heat source is removed. Once removed, however, recombination processes of the charged carriers are induced.

9.4 Experimental method

For this experiment, one probe is heated via a soldering iron and the multi-meter is switched to measure voltage change as opposed to photocurrent. All lighting and further electronics have also been excluded. The negative and positive terminals of a Keithley 2000 multi-meter were connected to the molybdenum electrodes on the CZTS surface. A voltage readout of zero is collected at room temperature prior to any application of heat (steady state). The contact connected to the positive terminal was then subsequently heated by a soldering iron maintained at a stable temperature of 200 °C and left for 60 seconds. Once a steady state was reached after this time, the soldering iron was removed allowing the semiconductor to cool back to room temperature. LabView software recorded the voltage readout as a function of time.

9.4.1 Results and Discussion

In order to test the experimental setup, hot probe characteristics were collected for a pure crystalline silicon wafer as a function of changing temperatures as indicated in Figure 56. The voltage readouts show a positive polarity between the two electrodes concluding this sample is *n*-type material (majority carriers are electrons) as expected.

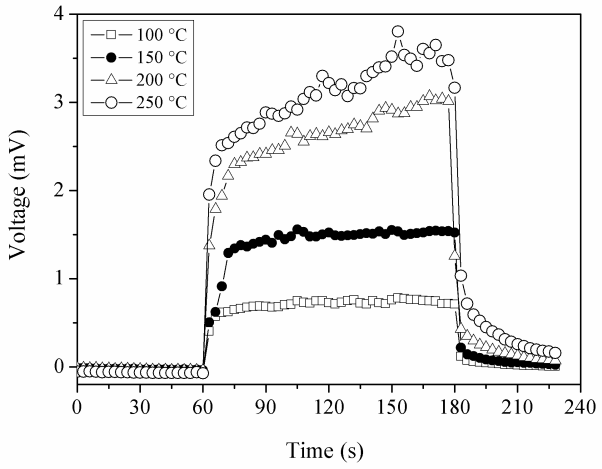

Figure 56: **Hot point probe characteristics over time for an n-type silicon wafer as a function of temperature.**

One noticeable feature is the similarity of the curves with a gradual rise in voltage as the temperature is increased. Furthermore, upon the application of heat there is an immediate incline in voltage response before reaching a steady state. The voltage at this point slowly continues to rise and is more emphasised at higher temperatures, which is likely to be caused by the cool electrode slowly heating up. However, over time it is likely there would be a voltage drop off as a gradual heating of the cooler contact would tend to reduce the voltage and not increase it. Once the heat is taken away via the hot probe, the voltage shows a dramatic decline back to its original stable state near a zero voltage.

1. Stacked library: Sn/Cu/Zn

Figure 57 and Table 27 present selected hot point probe measurements made across the Sn/Cu/Zn stacked CZTS library with respect to a range of elemental compositions. All points measured at 200 °C resulted in a negative voltage readout implying p-type conductivity. It is therefore clear that the conductivity type does not change with regards to elemental composition. All curves showed very similar behaviour, albeit moderate changes in the voltage readout.

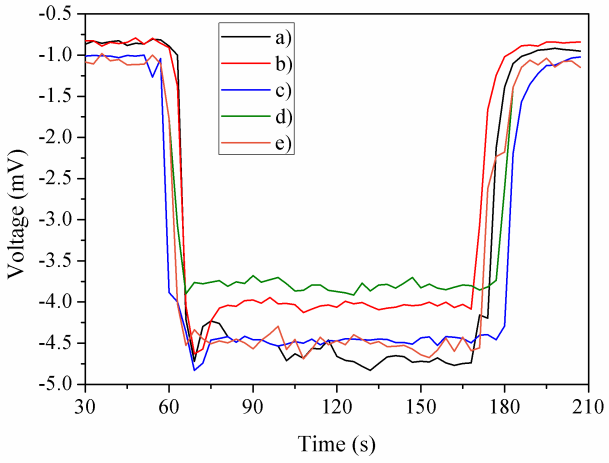

Figure 57: **Hot point probe characteristics for *p*-type CZTS (stacking configuration Sn/Cu/Zn) as a function of composition, measured at 200 °C.**

Sample	Zn/Sn	Cu/(Zn+Sn)	S/metal
a	2.41	0.51	0.96
b	1.41	0.82	1.04
c	1.03	1.02	0.97
d	0.83	1.14	1.17
e	0.41	1.54	0.94

Table 27: **Summary of selected elemental composition ratios corresponding to curves a) - e) in Figure 57.**

Results for other configuration libraries (i.e. co-sputtered and the remaining stacked libraries), although not presented, showed very similar results yielding *p*-type conductivity. It is important to note that all Cu-rich regions underwent delamination after KCN etching, hence measurements in this region of the phase-composition diagram could not be achieved.

10 CZTS device fabrication

> *"I have no doubt that we will be successful in harnessing the sun's energy. If sunbeams were weapons of war, we would have had solar energy centuries ago."* - George Porter, Nobel Prize winner in Chemistry (1967)

Reports on some milestone CZTS device efficiencies were outlined in Section 2.3.2, concluding that a high performing device generally constitutes a Zn-rich/Cu-poor absorber layer. This chapter presents results on how the composition and configuration structure of the CZTS thin film directly influences overall device performance. The first section gives a brief overview on the background of device physics, before moving onto the motivation behind selecting specific compositions to be incorporated into a device. Finally, the device fabrication/characteristics are described and performance parameters are presented with proposals to why such results may be occurring.

10.1 Characteristics of solar cell devices: a brief theoretical background

The performance of photovoltaic cells can be modelled as a current source in parallel with a diode. Put simply, under no illumination there is no current generated and the PV cell behaves like a diode [40]. When the cell is subjected to illumination, current is generated by the PV cell. If a typical current-voltage (I-V) curve of a *pn*-junction diode in the dark and under illumination is considered, as illustrated in Figure 58, three key solar cell parameters can be defined: short circuit current (I_{SC}), open-circuit voltage (V_{OC}) and the fill factor FF.

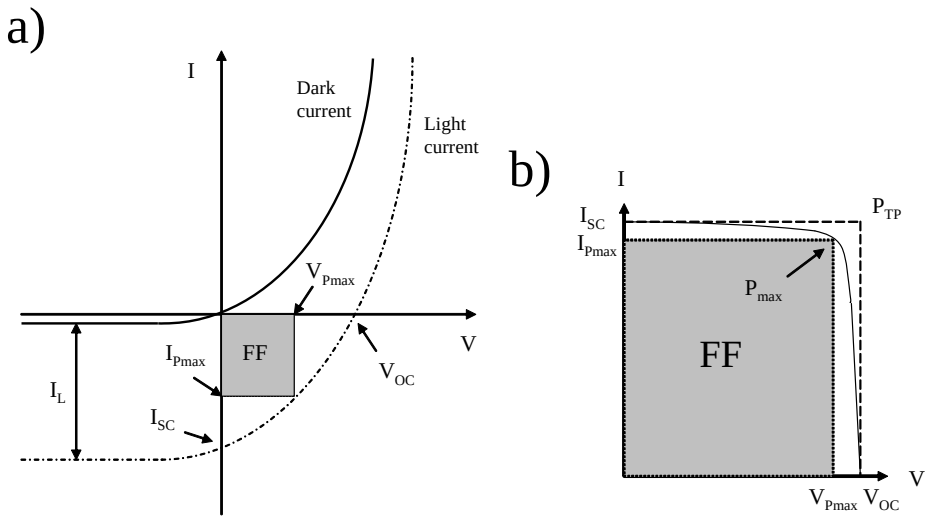

Figure 58: **Current-voltage (I-V) characteristics of an ideal *pn*-junction both in the dark and under illumination: (a) The three main solar cell parameters and light-generated current ($\mathbf{I_L}$) are defined: short-circuit current ($\mathbf{I_{SC}}$), open-circuit voltage ($\mathbf{V_{OC}}$) and fill factor (FF), and; (b) The FF value is obtained by the maximum rectangle given by $\mathbf{I_{Pmax}}$ and $\mathbf{V_{Pmax}}$.**

Each parameter is defined as follows:

- Short circuit current, I_{SC} (or J_{SC})

The short circuit current, I_{SC}, corresponds to the condition when the impedance is low and is calculated when the voltage, V, equates to zero: $I_{V=0} = I_{SC}$. When this condition is satisfied, then the short circuit current is equal to the light-generated current: $I_{SC} = I_L$. As indicated in Figure 58(a), I_{SC} occurs at the beginning of the forward-bias sweep and is the maximum current value in the power quadrant (see Figure 58(b)). For an ideal cell, this maximum current value is the total current produced in the solar cell by photon excitation.

- Open circuit voltage, V_{OC}

The open circuit voltage, V_{OC}, occurs when there is no current (I = 0) passing through the cell such that: $V_{I=0} = V_{OC}$. For an ideal diode:

$$V_{OC} = \frac{kT}{q} \ln\left(\frac{I_L}{I_S} + 1\right) \tag{24}$$

where kT/q is the thermal voltage and I_S is the saturation current.

The voltage and current at which power output is a maximum (P_{max}), are known as V_{Pmax} and I_{Pmax}, respectively as illustrated in Figure 58b. With this information, the final solar cell parameter can be defined known as the fill factor (FF).

- Fill Factor, FF

Often represented as a percentage, the fill factor FF, is essentially a measure of the quality or performance of the device and is determined by the fraction of the total power of incident light that can be converted into electrical power. Under illumination, the *pn* junction is forward biased and the external load resistance determines an operating point on the I-V curve. The ideal diode behaviour is given by:

$$P = I_{Pmax}\frac{KT}{q}\ln\left(1+\frac{I_{Pmax}+I_L}{I_S}\right) \tag{25}$$

In general, the device will operate under conditions favourable towards maximum power output. FF can also be interpreted graphically as the ratio of the rectangular areas depicted in Figure 58(b). A larger fill factor is desirable, and corresponds to an I-V sweep that is more square-like. Typical fill factors range from 0.5 to 0.82. In practice, the FF will never reach its theoretical maximum and will be lower due to the presence of parasitic resistive losses. The value of FF is therefore most commonly determined from measurement of the IV curve and is defined as the maximum power divided by the product of V_{OC} and I_{SC}. The maximum possible area for a given I-V curve determines the fill factor defined by:

$$FF = \frac{V_{Pmax}I_{Pmax}}{V_{oc}I_{sc}} \tag{26}$$

- Conversion efficiency, η

Efficiency, η, is the ratio of the electrical power output P_{out}, compared to the solar power input, P_{in}, into the PV cell. P_{out} can be taken to be P_{max} since the solar cell can be operated up to its maximum power output to get the maximum efficiency. A thorough and detailed explanation relating to the theory of semiconductors and device structures can be found in the following reference [41].

10.2 Selecting CZTS absorber layer compositions

The fabrication of CZTS-based solar devices consisted of a systematic approach based on the photoconductivity and hot-point probe results. As outlined in Chapter 9, room temperature photoconductivity responses were obtained for various compositions and absorber layer configurations. In order to test the validity of both techniques, only high performing responses were selected from each configuration to be incorporated within a device structure. More specifically, the two highest photoconductivity responses were chosen. The range of p-type samples after KCN etching which correspond to the chosen structure and composition are listed in Table 28.

		Composition	
Sample	**Configuration**	**Cu/(Zn+Sn)**	**Zn/Sn**
A	Co-sputtered	0.49	2.96
B	Co-sputtered	0.67	1.21
C	Sn/Cu/Zn	0.56	1.21
D	Sn/Cu/Zn	0.76	1.14
E	Zn/SnCu	1.32	2.43
F	Zn/Sn/Cu	1.12	1.76

Table 28: **A list of p-type compositions (after KCN etching) and configurations as selected by high performing photoconductivity responses**.

10.3 Device fabrication and characterisation

The device structure used in this study is akin to that of standard CIGS/CIS and CZTS configurations. Directly deposited onto Mo-coated glass (SLG) substrates, the device order is depicted in Figure 59 and is as follows: CZTS/CdS/ZnO:Al/ITO/Al/Ni.

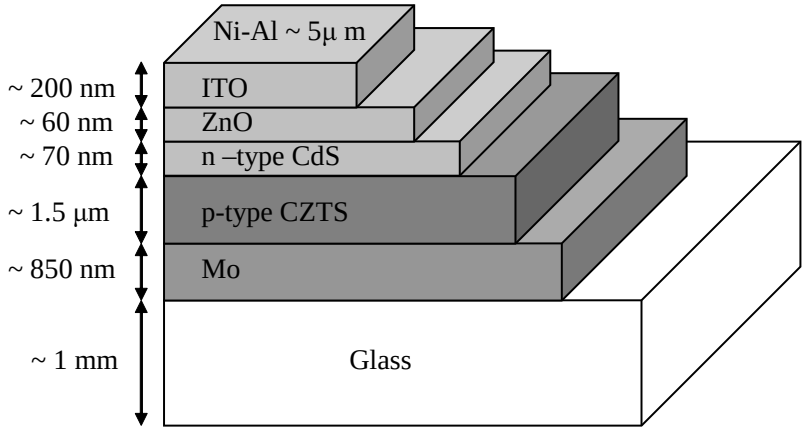

Figure 59: **Schematic cross-section of the CZTS device structure used for this study.**

During the CZTS deposition, two samples were fabricated simultaneously under identical conditions with the first being used as a "control measure" for materials characterisation immediately after synthesis, and the second kept in preparation for complete device fabrication. The stages of device fabrication are outlined as follows:

1. Mo back contact - a 850 nm thick Mo layer deposited using RF sputtering (Nordiko 2000) directly onto glass (SLG) substrates. Sputter power and deposition time were 300 W and 120 minutes, respectively.

2. CZTS absorber layer deposition - a uniform Cu-Zn-Sn precursor layer ($\approx$ 500 nm) was either co-deposited or stacked onto the Mo-coated substrates using DC magnetron sputtering. Substrates were placed onto a rotating table to ensure uniformity. The samples subsequently underwent sulphurisation at 500 °C for 30 minutes yielding a total CZTS layer thickness of approximately 1.5 µm. All samples were subjected to KCN etchant and dried in N_2 gas flux.

3. Chemical bath deposition (CBD) of CdS buffer layer - a 70 nm CdS buffer layer was deposited using the chemical bath deposition (CBD) method. An aqueous solution was formed containing 0.1456 g of cadmium sulfate ($CdSO_4$), 31.8 g of ammonium hydroxide (NH_4OH), 0.333 g of thiourea and was subsequently transferred into a glass jar with a double walled water jacket and placed in the centre of an ultrasonic bath. The Mo/CZTS samples were then securely mounted onto a glass holder (up to eight samples could be deposited in a

single run) and subsequently immersed into the solution. The solution was continuously stirred at a constant rate during the film deposition process for 20 minutes at 65 °C (uniformity was within 10%).

4. ZnO window layer - a pulse RF sputtered (Teer coatings UDP350) *i*-ZnO layer approximately 50 nm in thickness (0.2 A for 35 min).

5. Indium tin oxide (ITO) - a 200 nm layer deposited using RF sputtering at 150 °C (200 W for 120 minutes).

6. The cells were completed using sputtered Ni/Al contacts - 50 nm layer of Ni by RF magnetron sputtering (120 W for 60 minutes). A 4000 nm layer of Al was further deposited by e-beam evaporation (TecVac ECU700).

Current–voltage (I-V) measurements were recorded at 25.8 °C under standard AM 1.5 (100 mW cm^2) illumination using a solar simulator (Abet-technologies Sun 2000), with uniform output over a 4 x 4 inch area. Several new aspects and the synthesis of thin film layers are introduced here such as the *n*-type CdS layer crucial for the formation of the *p*-*n* junction with CZTS. However, the underlying physics and properties are not described in detail. As these parameters are not critical parts of this thesis, they have been excluded and only a brief overview of how each individual layer is fabricated is given. The reader is referred to reference [41] for further information.

10.4 Properties and performance of CZTS devices

The CZTS solar cell performance parameters with different metallic composition and configurations are presented and discussed in this section. The key parameters as outlined in the beginning of this chapter, namely the V_{OC}, J_{SC}, FF and conversion efficiencies, are obtained from the 24 individual cells fabricated across one sample substrate and have been labelled from A to F for ease of comparison. It should be noted that the highest performing cell has only been presented. Figures 60 - 62 illustrate the J-V curved for the devices corresponding to Table 29.

Device	Configuration	V_{OC} (mV)	J_{SC} (mA/cm^2)	FF (%)	η (%)
A	Co-sputtered	218	3	29.96	0.23
B	Co-sputtered	77	20	28.44	1.29
C	Sn/Cu/Zn	69	3	24.46	0.05
D	Sn/Cu/Zn	8.3	0.91	24.23	0.003
E	Zn/SnCu	40	0.18	24.44	0.02
F	Zn/Sn/Cu	39	2.40	23.86	0.03

Table 29: **CZTS cell parameters: V_{OC}, J_{SC}, FF and η for the highest performing cells of each configuration and compositional region.**

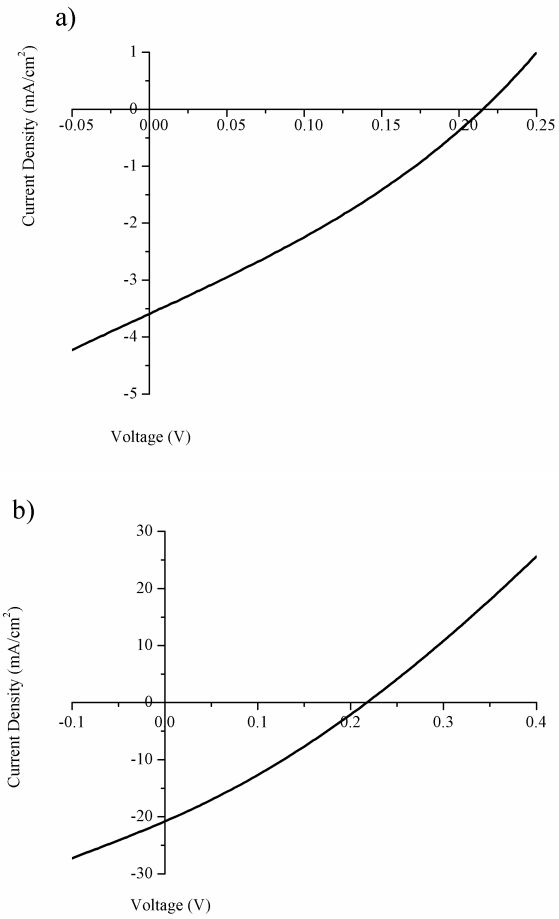

Figure 60: **J-V curves of the highest performing co-sputtered CZTS device structures: (a) - Device A and, (b) - Device B.**

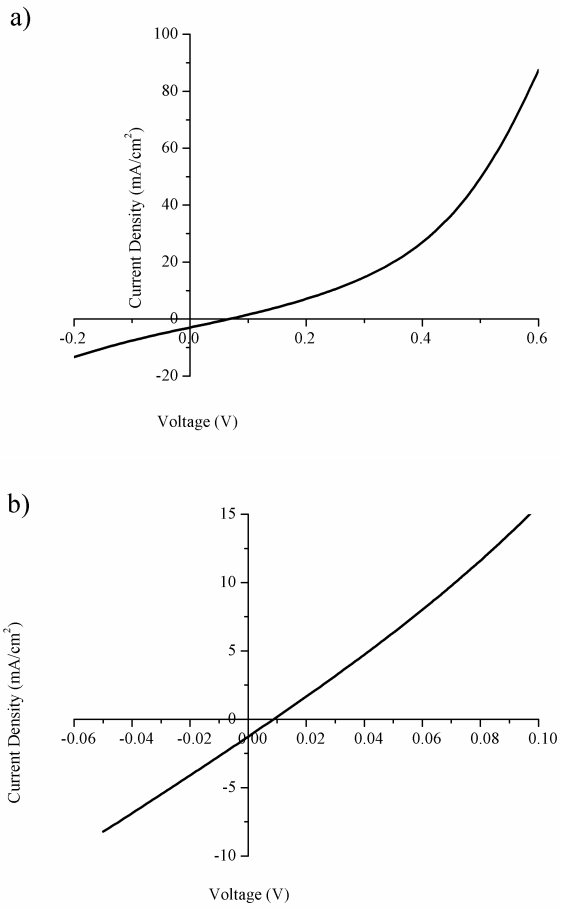

Figure 61: **J-V curves of the highest performing CZTS (stacking order Sn/Cu/Zn) device structures: (a) - Device C and, (b) - Device D.**

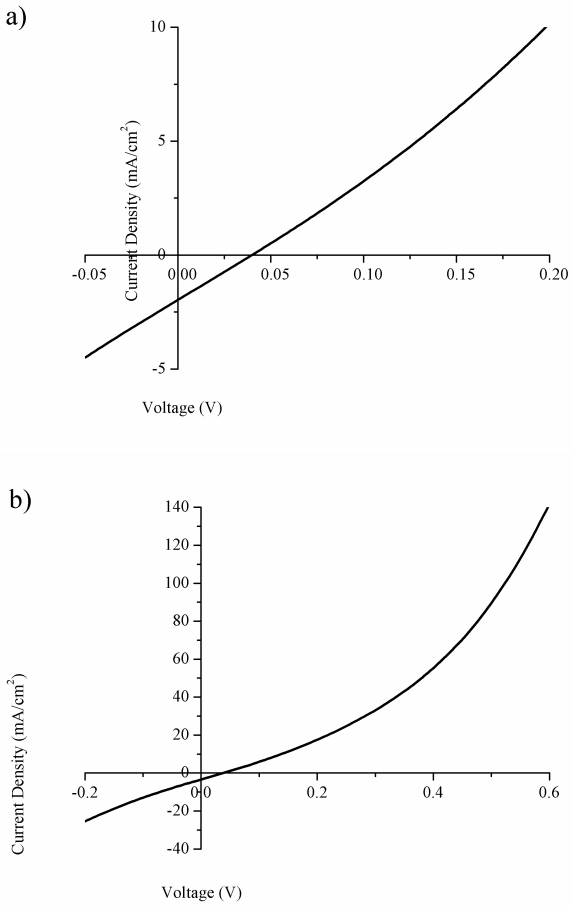

Figure 62: **J-V curves of the highest performing CZTS (with stacking order Zn/Sn/Cu) device structures: a) - Device E and, (b) - Device F.**

In summary, the overall performance of CZTS-based devices in this investigation is very poor and far from ideal. The FF is below 30% for all devices, which is predominately down to shunting and series resistance. The highest efficiency attained in this work corresponds to device B (η = 1.29 %), which consists of a co-sputtered absorber layer with metallic ratios: Cu/(Zn+Sn) = 0.67 and Zn/Sn = 1.21. This is somewhat promising as the layer is moderately photo-active and Cu-deficient/Zn-rich which ties in well with the literature on CZTS device efficiencies in Section 2.4. Furthermore, it is particularly encouraging that a Cu-poor/Zn-rich final composition is the highest performing which consolidates the accuracy to some degree of the photoconductivity technique.

11 Conclusions and future outlook

The main objective of this thesis was to demonstrate the novel and powerful use of the combinatorial approach to explore new and exciting materials like CZTS. This tool provided successful formation of the Cu-Zn-Sn-S library into the desired kesterite phase, although there were clear composition-dependent phases that also formed. The first part of this study, which included Chapter's 3, 4 and 5, importantly focussed on devising and setting up the combinatorial synthesis protocol in order to fabricate compositionally graded metallic thin films. The precursor layers Cu-Zn-Sn were DC magnetron sputtered directly onto a single glass substrate to create a composition-spread library with the point of stoichiometry near the centre. The primary goal at this stage was to accurately and reproducibly yield the correct stoichiometry (Cu:Zn:Sn = 2:1:1 ratio) towards the centre of the library with a deviation in composition spanning a wide spatial region within the Cu-Zn-Sn ternary phase diagram. Two different deposition configurations were explored: co-sputtering and discrete stacking of metallic layers (of which the elements were alternated to assess any effects the stacking order would have on the properties of the CZTS material). Chapter 6 then presented results on the composition and phase analysis of the precursor libraries, which are important to understand as ultimately these phases are likely to dictate the metal-sulphur phases that form during the sulphurisation/annealing process. Only co-sputtered and one stacked library with order (Sn/Cu/Zn) are presented in this thesis for comparative purposes although much of the data for the other stacking orders are given in the appendices.

The second part of this investigation concerned the suphurisation process as outlined in Chapters 7 and 8, whereby the metallic precursor libraries were subsequently heated at 500 °C in an atmosphere of S vapour for the metal-chalcogen conversion process. The idea was to then create a complete library that would cover a wide region within the Cu_2S-ZnS-SnS_2 phase diagram as devised by Olekseyuk et al. [97]. KCN etching treatment after sulphurisation was implemented as a means of eliminating unwanted CuS phases, although this caused severe damage to the film causing complete delamination in some instances.

Chapter 9 and 10 then focussed on the opto-electronic and electrical characterisitcs of CZTS libraries for a select range of compositions and configurations. Based on the results obtained from room temperature photoconductivity and the hot point probe, certain high performing compositions were used to fabricate CZTS-based device structures. However, even though all regions showed p-type conductivity as ascertained using the hot point probe and were photo-active, the device characteristics were significantly poor with the highest achieving device yielding a power conversion efficiency of around 1.26 % (FF close to 30%).

To conclude this investigation, we will discuss the key observations made during the analysis of the CZTS libraries and finally make some recommendations for further work. As outlined in the Chapter 1 and 2, the main objective of this thesis is to primarily focus on the role of metallic precursor composition and how this ultimately affects the formation and properties of CZTS. It is worth noting that this investigation principally focusses on the CZTS material as a single layer, so the work carried out in making device structures is fairly limited and would require further work to understand the behaviour as reported in Chapter 10. The photoconductivity and device performance of certain compositions are purely there as a measure of how well the material has formed, its compatibility to operate as a p-n junction and which compositions dictate the overall performance. Throughout this study, the composition ratios were defined as Cu/(Zn+Sn) and Zn/Sn and are normally described as "Cu-poor" and/or "Zn-rich" (and vice versa). We can draw some very interesting and important conclusions from this sudy as follows:

- Phase analysis as carried out by XRD on the precursor libraries grown at room temperature indicated several phases forming and were shown to be composition-dependent. There was clearly no evidence to suggest formation of any elemental Zn and Cu, ternary or Zn_xSn_y binary phases. Only Cu_xSn_y, Cu_xZn_y and Sn formed. In the regions of near-stoichiometry, where we would expect the precursor material to form phase-pure kesterite material when subjected to the sulphurisation process, there is a noticeable improvement in crystallinity which is particularly evident with the co-sputtered library. Furthermore, for the co-sputtered library only Cu_xZn_y phases were found to be present

in the stoichiometric region, but in the case of the stacked library (Sn/Cu/Zn) both Cu_xZn_y and Cu_xSn_y phases co-existed. Elemental Sn only precipitated at elevated Sn concentrations (and low Cu content). Thus, at an early stage it would seem sensible to assume that the co-sputtered precursor library would facilitate a more favourable reaction pathway for the kesterite structure to form with the potential precipitation of secondary phases depending on the compositon.

- Upon sulphurisation of the libraries, both XRD and Raman spectroscopy confirmed the existence of the desired kesterite crystal structure in all configurations. However, there was also evidence of many extraneous phases forming including ZnS, SnS and Cu_2SnS_3 which proved challenging to distinguish as they each had very similar crystal structures to that of kesterite and each other. Based on the observed phases formed, it was found that elemental precursors initially react with the present chalcogen to form binary compounds such as SnS_x, ZnS and CuS prior to the complete conversion of CZTS.

- In this investigation, the effects of Cu, Zn and Sn content were studied. If we begin by giving an overview on the Cu content it was clear the secondary phase of CuS in the most Cu-rich regions could be confirmed comfortably with both XRD and Raman and visualised with SEM imaging (via the formation of large CuS surface crystallites). Interestingly, Cu-rich regions tend to have better crystallinity suggesting improved film growth but CuS phases can segregate to the the upper region of the film as seen in this study. They can be removed by KCN etching but this proved an unfavourable method in this work as the post-etching morphology was particularly poor as a result. In some instances, it caused complete film delamination and further measurements could not be obtained. For Zn-rich regions, it is expected that ZnS should almost definitely form alongside CZTS. However, XRD and Raman could not conclusively identify this as mentioned in the previous paragraph. This phase is effectively insulating, having a band gap of around 3.6 eV, so the effects on the opto-electronic prperties is expected to be negligible. Finally for Sn-rich

regions, the binary SnS_x has been shown to form together with the ternary Cu-Sn-S compound, which is expected to be detrimental to device performance. However, SnS could not be cofirmed with either XRD and Raman using this current setup and would require further investigation. It is important to stress that each of the elements are strongly dependent on one another and a slight shift in one would lead to a shift in others thus causing different phases to form. Therefore, the growth conditions of CZTS are imperative in order to control which (or neither) phases form alongside CZTS.

- With respect to the opto-electronic and electrical measurements, the hot point probe indicated *p*-type conductivity for all regions assessed irrespective of composition or layer configuration. Room temperature photoconductivity generally showed a significant improvement in photoconducive response for Cu-poor/Zn-rich regions and a decline for Cu-rich/Zn-poor which ties in well with the literature. The underlying mechanism behind the idea that Cu-poor/Zn-rich compositions are better performing is perhaps unsurprising. As postulated by Chen et al. [135], under Zn-rich and Cu-poor conditions the substitution of Cu at Zn sites gives rise to deep acceptors compared to the shallow acceptors for isolated Cu vacancies. Thus, under these conditions the dominant defect is *p-t*ype and should be ideal, provided the ZnS phase is absent, for improved opto-electronic properties and ultimately maximising solar cell performance. Furthermore, much work is required to fully understand the behaviour of different compositions with respect to the photoconductive responses and hence the device structures.

- We can now, at least in part, select the positions of the potential devices on the phase diagram that are likely to be the "best." It has been shown that the best performing devices are not in the narrow single kesterite phase region (located in the centre of the phase diagram). This was further reinforced with the photoconductivity measurements. As mentioned previously, Cu-rich/Zn-poor regions are also undesirable due to the formation of Cu-S and Cu-Sn-S (and potentially SnS_x) phases. Although efforts have been made in this study

to reduce these phases such as subjecting the sample to KCN etching, the film has been shown to significantly deteriorate in quality thus hindering the formation of a good p-n junction. Adhesion problems have also arisen which could be attributed to the fact Cu is at the bottom in contact with the Mo back layer thus promotoing void formation. This is particularly true with stacked layers of precursors when the Cu layer is at the bottom. However, it seems that a moderate deviation from the point of stoichiometry can initiate the formation of secondary/ternary phases so it proves very difficult to control the formation of the pure kesterite phase.

- One final comment should be made about the different configurations used to deposit the CZTS absorber layer and how it plays a pivotal role in determining which phases form. We have revealed that the co-sputtered library shows improved crystallinity and less extraneous phase formation in conjunction to the kesterite structure. Even though the stacked layers were deposited using a twelve layer system of alternating elements, the growth conditions at room temperature are unfavourable and promote phase segregation when undergoing the conversion process. With application of heat during the precursor deposition, we would expect a significant improvement in film homogenity with repsect to layer depth. This perhaps leads onto one other question that arises when fabricating CZTS materials such that which is the best fabriction method to use. This study has used a two stage combinatorial approach to rapidly assess the effects of compositional variation on the properties of CZTS and has proved useful in the fact it has consolidated the current literature in terms of which is the best performing compositonal range i.e. Cu-poor/Zn-rich. However, this two stage method may not be the most desirable to prevent the precipitation of additional phases. It is clear that further work needs to be carried out in order to optimise and understand the fundamentals of single layer performance, as well as the behaviour of CZTS-based device structures. Furthermore, this methodology could also be used in future work to explore which other fabrication method may work in order to fabricate high quality pin-hole free CZTS material as well as assessing the impact of compositional

variation and/or elemental loss.

The progress in the development of CZTS(Se) absorber layers and devices are somewhat promising and offer an exciting alternative to the well established thin film materials already currently being used; efficiencies are steadily improving to around 10 % and we can expect this to continue as many more groups move into and focus on this field. Research carried out on the related CIS and CIGS materials, in terms of their chemistry and opto-electronic properties, has very much provided a plaform for this progression. However, like CIGS there are many challenges ahead in terms of controlling the film stoichiometry, defects and secondary/ternary phases that precipitate alongside the desired kesterite phase. Based on the work carried out in this study and the above concluding remarks, some recommendations for future CZTS research could be as follows:

1. Attention should be paid to the exact nature of the configuration used and how best to improve film homogenity with respect to depth. It would be particularly interesting to sputter (co-deposition or stacked) combinatorial CZTS libraries in-situ using RF sources (using compound sources such as ZnS, CuS, Sn...etc) and annealing each library within the chamber, although the temperature will have to be sufficiently low as not to cause any elemental evaporation due to high vapour pressures of Zn and Sn. This may reduce the amount of phase segregation, and hence delamination, experienced with most libraries.

2. The sulphurisation process must be fully investigated for a wide range of compositions. This study only used a fixed temperature, pressure and duration. The effect of composition on these different variables would be particularly interesting and give a very useful insight into the stability of the absorber layer under different conditions.

3. The photoconductivity set up is potentially very useful in terms of collecting further information about the CZTS defect chemistries. The variation in band gap should be an area of interest and studied in greater detail.

4. Having proved how useful the combinatorial approach can be in terms of de-

positing a diverse range of structurally and chemically similar samples, it would be possible to explore the Cu_2S-ZnS-SnS_2 phase equilibria in greater detail in terms of covering the same or similar composition regions at a wide range of synthesis temperatures.

5. Another interesting avenue to explore would be to pursue the idea of fabricating CZTS device libraries, once a more comprehensive study of the single absorber layer is achieved. Ultimately, this is a very complex and challenging route to take but on the other hand it is very beneficial as a wide range of devices with different composition and/or thickness can be incorporated in a single run/substrate.

References

[1] UNFPA, State of World Population report, People and Possibilities in a World of 7 Billion (2011).

[2] Markvart T., (2000) Solar Electricity, Technology & Engineering: John Wiley & Sons.

[3] Statistical Review of World Energy (2009), BP.

[4] Yang, Z. G., (2009), "Materials in Clean power systems; Advanced materials for a sustainable, clean energy future." *Journal of the Minerals, Metals and Materials Society*," 61(4), pp. 35.

[5] European Photovoltaic Industry Association (EPIA), Market Report 2011.

[6] Peter, L.M. (2011), "Towards sustainable photovoltaics: the search for new materials." *Phil. Trans. R. Soc. A*, 369(1942), 1840-1856.

[7] Green, M.A. (2006), "Consolidation of Thin-film Photovoltaic Technology: The Coming Decade of Opportunity." *Prog. Photovolt: Res. Appl*. 14, pp. 383–392.

[8] Alferov, Zh. I., Andreev, V. M., Kagan, M. B., Protasov, I. I., Trofim, V. G. (1970), "Solar-energy converters based on *p-n* $Al_xGa_{12x}As$-GaAs heterojunctions." Fiz. Tekh. Poluprovodn. 4, 2378 *Sov. Phys. Semicond.,* 4, 2047.

[9] Chopra, K. L., Paulson, P. D., Dutta, V. (2004), "Thin-film Solar Cells: an overview." *Prog. Photovolt: Res. Appl*. 12, 69–92.

[10] First Solar press release 2011, http://investor.firstsolar.com.

[11] Jackson, P., Hariskos, D., Lotter, E., Paetel S., Wuerz, R., Menner, R., Wischmann, W., and Powalla, M. (2011), "New world record efficiency for Cu(In,Ga)Se_2 thin-film solar cells beyond 20%." *Prog. Photovolt: Res. Appl,* 19, 894–897.

[12] Wolden, C. A., Kurtin, J., Baxter, J.B., Repins, I., Shaheen, S.E., Torvik, J.T., Rockett, A.A., Fthenakis, V.M., and Aydil, E.S. (2011), "Photovoltaic manufacturing: Present status, future prospects, and research needs." *J. Vac. Sci. Technol. A,* 29, 030801.

[13] Green, M.A., Emery, K., Hishikawa, Y., Warta, W., and Dunlop, E.D. (2011), "Solar cell efficiency tables (Version 38)." *Prog. Photovolt: Res. Appl;* 19, 565–572.

[14] King, R.R., (2008), "Multijunction cells: Record breakers." *Industry Perspective, Nature Photonics*, 2, 284 - 286.

[15] Conibeer G. (2009), "Progress on hot carrier cells." *Solar Energy Materials & Solar Cells,* 93, 713–719.

[16] Luque, A., Marti, A. (2011), "Photovoltaics: Towards the intermediate band." *Nature Photonics,* 5, 137–138.

[17] Leem, D-S., Edwards, A., Faist, M., Nelson, J., Bradley, D.DC., de Mello, J.C. (2011), "Efficient Organic Solar Cells with Solution-Processed Silver Nanowire Electrodes." *Adv. Mater.*, 23, 4371–4375.

[18] Taylor, S.R., McLennan, S.M. (1985), "The continental crust: its composition and evolution - an examination of the geochemical record preserved in sedimentary rocks." Blackwell Scientific Publication, Oxford, pp. 1-312.

[19] Mitzi, D.B., Gunawan, O, Todorov, T.K, Wang, K, Guha, S. (2011), "The path towards a high-performance solution-processed kesterite solar cell." *Solar Energy Materials & Solar Cells*, 95(6) 1421–1436.

[20] Jung, Y., Agarwal, R., Yang, C-Y. (2011) "Chalcogenide phase-change memory nanotubes for lower writing current operation." *Nanotechnology,* 22, 254012.

[21] Nair, P. K., Huang L., Nair M. T. S., Hailin Hu, Meyers E. A. , Zingaro, R. A. (1997) "Formation of *p*-type Cu_3BiS_3 absorber thin films by annealing chemically deposited BiS_3– CuS thin films." *J. Mater. Res.*, 12(3).

[22] Colombara, D., Peter, L.M., Rogers, K.D., Hutchings, K. (2012) "Thermochemical and kinetic aspects of the sulfurization of Cu–Sb and Cu–Bi thin films." *Journal of Solid State Chemistry,* 186, 36–46.

[23] Chen, S., et al. (2009), "Crystal and electronic band structure of Cu_2ZnSnX_4 (X = S and Se) photovoltaic absorbers: First-principles insights." *Appl. Phys. Lett.,* 94, 041903.

[24] Katagiri, H., Saitoh, K., Washio, T., Shinohara, H., Kurumadani, T., Miyajima, S (2001), "Development of thin film solar cell based on Cu_2ZnSnS_4 thin films." *Solar Energy Materials and Solar Cells*, 65(1-4), pp. 141–148.

[25] Seol, J.S., Lee, S.Y., Lee, J.C., Nam H.D., Kim, K.H. (2003), "Electrical and optical properties of Cu_2ZnSnS_4 thin films prepared by rf magnetron sputtering process." *Sol. Energy Mater.*, 75, p. 155.

[26] Hall, S.R., Szymanski, J.T., Stewart, J.M. (1978), "Kesterite, $Cu_2(Zn,Fe)SnS_4$and stannite, $Cu_2(Fe,Zn)SnS_4$, structurally similar but distinct minerals." *Can. Mineral.,* 16, 131–137.

[27] Schorr S. (2011), "The crystal structure of kesterite type compounds: A neutron and X-ray diffraction study." *Solar Energy Materials & Solar Cells*, 95, 1482–1488.

[28] Ito K, Nakazawa T. (1988), "Electrical and optical properties of stannite-type quaternary semiconductor thin films." *Jpn. J. Appl. Phys.,* 27, 2094–2097.

[29] Tanaka, T., et al. (2005), "Preparation of Cu_2ZnSnS_4 thin films by hybrid sputtering." *Journal of Physics and Chemistry of Solids*, 66, 1978–1981.

[30] Momose, N. et al. (2011), "Cu_2ZnSnS_4 Thin Film Solar Cells Utilizing Sulfurization of Metallic Precursor Prepared by Simultaneous Sputtering of Metal Targets." *Jpn. J. Appl. Phys. 50*, 01BG09.

[31] Fernandes, P.A., Salomé P. M. P., da Cunha, A. F. (2009), "Precursors' order effect on the properties of sulfurized Cu_2ZnSnS_4 thin films." *Semicond. Sci. Technol.,* 24, 105013.

[32] Araki, H. et al. (2008), "Preparation of Cu_2ZnSnS_4 thin films by sulfurization of stacked metallic layers." *Thin Solid Films,* 517, 1457–1460.

[33] Prabhakar, T., Nagaraju, J. (2010), "Ultrasonic spray pyrolysis of CZTS solar cell absorber layers and characterisation studies." Photovoltaic Specialists Conference (PVSC), 35th IEEE.

[34] Moritake, N. et al. (2009), "Preparation of Cu_2ZnSnS_4 thin film solar cells under non-vacuum condition." *Phys. Status Solidi C,* 6(5), 1233– 1236.

[35] Zhou, Z., et al. (2010), "Fabrication of Cu_2ZnSnS_4 screen printed layers for solar cells." *Solar Energy Materials & Solar Cells* 94, 2042–2045.

[36] Todorov, T. K, Reuter, K. B, Mitzi, D. B. (2010), "High-Efficiency Solar Cell with Earth- Abundant Liquid-Processed Absorber." *Advanced Materials*, 22, E156-159.

[37] Guo, Q, Hillhouse, H. W, Agrawal, R. (2009), "Synthesis of Cu_2ZnSnS_4 Nanocrystal Ink and Its Use for Solar Cells." *Journal of the American Chemical Society*, 131, 11672-11673.

[38] Scragg, J. J, Dale, P. J, Peter, L. M. (2008), "Towards sustainable materials for solar energy conversion: Preparation and photoelectrochemical characterization of Cu_2ZnSnS_4." *Electrochemistry Communications*, 10, 639-642.

[39] Chapin, D.M., Fuller, C.S., Pearson G.L. (1954), "A new *p-n* junction photocell for converting solar radiation into electrical power." *Journal of Applied Physics*, 25, 676-677.

[40] J. Nelson, The Physics of Solar Cells, Imperial College Press (2003).

[41] Friedlmeier, T. M., Wieser, N., Walter, T., Dittrich, H., Schock, H. W. (1997), "Heterojuncitons based on Cu_2ZnSnS_4 and $Cu_2ZnSnSe_4$ thin films." Proceedings of the 14th European Conference of Photovoltaic Solar Energy Conference and Exhibition, Bedford, p. 1242.

[42] Katagiri, H., Jimbo, K., Moriya, K., Tsuchida, K. (2003), "Solar cell without environmental pollution by using CZTS thin film," in Proceedings of the 3rd World Conference on Photovoltaic Energy Conversion, pp. 2874–2879, Osaka, Japan.

[43] Katagiri, H., et al., (2008), "Enhanced conversion efficiencies of Cu_2ZnSnS_4-based thin film solar cells by using preferential etching technique." *Applied Physics Express*, 1(4) 041201.

[44] Wang, H. (2011), "Progress in Thin Film Solar Cells Based on Cu_2ZnSnS_4." *Review article: International Journal of Photoenergy,* Volume 2011, 801292.

[45] Barkhouse, D. A. R., Gunawan, O., Gokmen, T., Todorov, T. K., Mitzi, D. B. (2012), "Device characteristics of a 10.1% hydrazine-processed $Cu_2ZnSn(S, Se)_4$solar cell." *Prog. Photovolt: Res. Appl.*, 20, pp. 6–11.

[46] Guo, Q., Ford, G. M., Yang, W. C., Walker, B. C., Stach, E. A., Hillhouse, H. W., Agrawal, R. (2010), "Fabrication of 7.2% efficient CZTSSe solar cells using CZTS nanocrystals." *Journal of the American Chemical Society*, 132, 17384–17386.

[47] Wang, K., Gunawan, O., Todorov, T., Shin, B., Chey, S. J., Bojarczuk, N. A., Mitzi, D., Guha, S. (2010), "Thermally evaporated Cu_2ZnSnS_4 solar cells." *Applied Physics Letters*, 97, 143508.

[48] Shockley, W., Queisser, H. J. (1961), "Detailed Balance Limit of Efficiency of *p-n* Junction Solar Cells." *Journal of Applied Physics*, 32, 510-519.

[49] Ahmed, S., Reuter, K. B., Gunawan, O., Guo, L., Romankiw, L. T., Deligianni, H. (2012), "A High Efficiency Electrodeposited Cu_2ZnSnS_4 Solar Cell." *Advanced Energy Materials*, 2(2), pp. 253–259.

[50] http://www.solar-frontier.com/news/64, October 2010.

[51] Rajeshmon, V. G., Sudha Kartha, C., Vijayakumar, K. P. (2010), "Spray Pyrolysed Cu_2ZnSnS_4 Solar Cell Using Cadmium Free Buffer Layer." *AIP Conf. Proc.*, 1349, pp. 683-684.

[52] Li, W., Cohen, S., Gartsman, K., Caballero, R., van Huth, P., Popovitz-Biro, R., Cahen, D. (2012), "Chemical compositional non-uniformity and its effects on CIGS solar cell performance at the nm-scale." *Solar Energy Materials & Solar Cells*, 98, pp. 78–82.

[53] Chirilă, A., et al. (2011), "Highly efficient $Cu(In,Ga)Se_2$ solar cells grown on flexible polymer films." *Nature Materials,* 10, 857–861.

[54] Tanaka, T., Yoshida, A., Saiki, D., Saito, K., Guo, Q., Nishiro, M., Yamaguchi, T. (2010), "Influence of composition ratio on properties of Cu_2ZnSnS_4 thin films fabricated by co-evaporation." *Thin Solid Films,* 518(21), pp. S29–S33.

[55] Suresh Babu, G., Kishore Kumar, Y.B., Uday Bhaskar, P., Sundara Raja, V. (2010), "Effect of Cu/(Zn+Sn) ratio on the properties of co-evaporated $Cu_2ZnSnSe_4$ thin films." *Solar Energy Materials & Solar Cells,* 94, 221–226.

[56] Tanaka, K., Fukui, Y., Moritake, N., Uchiki, H. (2011), "Chemical composition dependence of morphological and optical properties of Cu_2ZnSnS_4 thin films deposited by sol-gel sulfurization and Cu_2ZnSnS_4 thin film solar cell efficiency." *Solar Energy Materials & Solar Cells*, 95(3), pp. 838–842.

[57] Kishore Kumar, Y.B., Uday Bhaskar, P, Suresh Babu, G., Sundara Raja, V. (2010), "Effect of copper salt and thiourea concentrations on the formation of Cu_2ZnSnS_4 thin films by spray pyrolysis." *Phys. Status Solidi A,* 207(1), 149–156.

[58] Platzer-Bjorkman, C., Scragg, J. J., Flammersberger, H., Kubart, T., Edoff, M. (2012), "Influence of precursor sulfur content on film formation and compositional changes in Cu_2ZnSnS_4 films and solar cells." *Solar Energy Materials & Solar Cells,* 98, pp. 110–117.

[59] Tisza, M. (2001), "Physical metallurgy for engineers." *ASM International - Technology & Engineering.*

[60] Massalski, T. B., Murray, J. L., Bennett, L. H., Baker, H. (1986), "Binary Alloy Phase Diagrams." *American Society for Metals*, 1st edisition, Metals Park, OH.

[61] Argawal, N. (2003), "Microstructural and microhardness Studies of Microwave Sintered Cu-12Sn Bronze Alloys." *Transactions of PMA1*, 2.

[62] Chou, C.Y., Chen, S. W. (2006), "Phase equilibria of the Sn-Zn-Cu ternary system." *Acta Materialia*, 54(9), pp. 2393-2400.

[63] Geysen, H. M., Schoenen, F., Wagner D., Wagner, R. (2003), "Combinatorial compound libraries for drug discovery: an ongoing challenge." *Nature Reviews Drug Discovery,* 2, pp. 222-230.

[64] Gao, K., Yuan, L., Wang, L. (2006), "High-Throughput Selection for Heterogeneous Catalysts." *J. Comb. Chem.*, 8(2), pp. 247–251.

[65] Hanak, J. J. (1970), "The multiple-sample concept in materials research: Synthesis, compositional analysis and testing of entire multicomponent systems." *J. Mater. Science*, 5(11), pp. 964-971.

[66] Krishna, R, (2005), "Materials informatics." *Materials Today*, 8(10), pp. 38–45.

[67] Xiang, X. et al., (1995), "A Combinatorial Approach to Materials Discovery." *Science*, 268(5218), pp. 1738-1740.

[68] Kennedy, K., Stefansky, T., Davy, G., Zackay, V., Parker, . R. (165), J. Appl. Phys. 1965, 36, 3808.

[69] Perkins, J.D., van Hest, M. F. A. M., Teplin, C. W., Dabney, M. S., Ginley, D. S. (2007), *"*In Situ Etch Rate Measurements of Thin Film Combinatorial Libraries*"*. *Applied Surface Science,* 254(3), pp. 687-691.

[70] Kuykendall, T., Ulrich, P., Aloni S., Yang, P. (2007), "Complete composition tunability of InGaN nanowires using a combinatorial approach." *Nature Materials*, 6, pp. 951-956.

[71] Friebe, C., Wild, A., Perelaer, J., Schubert, U. S. (2012), "Inkjet Printing of Zinc(II) Bis-2,2´:6´,2˝-Terpyridine Metallopolymers: Printability and Film-Forming Studies by a Combinatorial Thin-Film Library Approach." *Macromol. Rapid Commun.,* 33(6-7), pp. 503-509.

[72] Haber, J. A., Gerein, N. J., Hatchard, T. D., Versavel, M. Y., (2005), "Combinatorial discovery of new thin film photovoltaics." *Photovoltaic Specialists Conference*, Conference Record of the Thirty-first IEEE, pp. 155-158.

[73] Teeter, G., Du, H., Leisch, J. E., Young, M., Yan, F., Johnston, S. W., Dippo, P., Kuciauskas, D., Romero, M. J., Newhouse, P., Asher, S. E., Ginley D. S. (2010), "Combinatorial study of thin film Cu_2ZnSnS_4 synthesis via metal precursor sulfurization." Photovoltaic Specialists Conference (PVSC), Conference Record of the Thirty-fifth IEEE, pp. 650-655.

[74] Ohring, M. (2002), "Materials Science of Thin Films: Deposition and Structure." second edition, Academic Press.

[75] Wang, Z. A., Chu, J. B., Zhu, H. B., Sun, Z., Chen, Y. W., Huang, S. M. (200), "Growth of ZnO:Al films by RF sputtering at room temperature for solar cell applications." *Solid-State Electronics,* 53, pp. 1149–1153.

[76] Kolasinski, R. D., Polk, J. E., Goebel, D., Johnson, L. K. (2007), "Sputtering yield measurements at glancing incidence using a quartz crystal microbalance." *J. Vac. Sci. Technol.,* A 25(2).

[77] http://www.inficonthinfilmdeposition.com/en/ic6.html

[78] Sigmund, P., (1981), "Sputtering by ion bombardment: Theoretical concepts." *In: Behrisch, R. (Ed.), Topics in Applied Physics. In: Sputtering by Particle Bombardment I*, 47. Springer-Verlag, Berlin. ch. 2.

[79] Cassidy, T. A., Johnson, R. E. (2005), "Monte Carlo model of sputtering and other ejection processes within a regolith." *Icarus,* 176, pp. 499–507.

[80] Sobbia, R., Browning, P. K., Bradley, J. W. (2008), "Numerical investigation via three-dimensional Monte Carlo modeling of sputtering and deposition processes in a direct current unbalanced magnetron discharge." J. *Vac. Sci. Technol., A* 26, 103.

[81] Goldstein, J., Newbury, D., Joy, D., Lyman, C., Echlin, P., Lifshin, E., Sawyer, L., Michael, J. (2003),"Scanning Electron Microscopy and X-ray Microanalysis." 3rd edition, Springer, New York.

[82] Zhang, S., Li, L., Kumar, A. (200), "Materials Characterisation Techniques." CRC, Boca Raton.

[83] Cullity, B. D., Stock, S. R. (2001), "Elements of X-ray Diffraction." 3rd Edition, Prentice Hall.

[84] Smith, E., Dent, G. (2005), "Modern Raman spectroscopy: a practical approach." John Wiley and Sons.

[85] Lewis, I. R., Edwards, H., Edwards, H. G. M. (2001), "Handbook of Raman Spectroscopy: From the Research Laboratory to the Process Line." Volume 28, CRC Press.

[86] Tesmer, J. R., Nastasi, M. A. (1995), "Handbook of modern ion beam materials analysis." Materials Research Society.

[87] Mayer, M. (1997), SIMNRA User's Guide, *Report IPP 9/113*, Max-Planck-Institut fur Plasmaphysik, Garching, Germany.

[88] Lee, I. H., Jeong, J-W., Chang, K. J. (1997), "Invariant-molecular-dynamics study of the diamond-to-b-Sn transition in Si under hydrostatic and uniaxial compressions." *Physical Review B*, 55(9), 5689-5693.

[89] Srinivasa, Rao S., Anamtharaman, T.R., (1969), Z. Metallkd., 60, 312.

[90] Brandon, J.K., Brizard, R.Y., Chieh, P.C., McMillan, R.K., Pearson, W.B. (1974), Acta Crystallogra., Sec B, 1412, 30.

[91] Westgreen, A. (1928), Z.Anorg.Allg.Chem., 175, 80.

[92] Larsson, A. K., Stenberg, L., Liden, S. (1994), Acta Crystallogra., Sec B, 50B, 636-6.

[93] Lee, J.A., Raynor, G.V. (1954), Proc. Phys. Soc., London, 67, 737.

[94] Liao, C. N., Wei, C. T. (2006), "An isochronal kinetic study of intermetallic compound growth in Sn/Cu thin film couples." *Thin Solid Films*, 515, pp. 2781-2785.

[95] Beattie, S. D., Dahn, J. R. (2003), "Single-bath electrodeposition of a combinatorial library of binary $Cu_{1-x}Sn_x$ alloys." *Journal of the Electrochemical Society*, 150(7), C457-460.

[96] Huang, C. W., Lin, K. L. (2004), "Interfacial reactions of lead-free Sn–Zn based solders on Cu and Cu plated electroless Ni–P/Au layer under aging at 150 °C." *J. Mater. Res.*, 19(12).

[97] Olekseyuk, I. D., Dudchak, I. V., Piskach, L. V. (2003), "Phase equilibria in the Cu_2S-ZnS-SnS_2 system." *Journal of Alloys & Compounds*, 368, pp. 135-143.

[98] Scragg, J. J. (2010), "Studies of Cu_2ZnSnS_4 films prepared by sulfurisation of electrodeposited precursors." Thesis (Doctor of Philosophy, PhD). University of Bath.

[99] Cheng, A. J., Manno, M., Khare, A., Leighton, C., Campbell, S. A., Aydil, E. S. (2011), "Imaging and phase identification of Cu_2ZnSnS_4 thin films using confocal Raman spectroscopy." *J. Vac. Sci. Technol.,* A 29, 051203.

[100] Sarswat, P. K., Free, M. L., Tiwari, A. (2011), "Temperature-dependent study of the Raman A mode of Cu_2ZnSnS_4 thin films." *Phys. Status Solidi B* 248(9), pp. 2170–2174.

[101] Schafer, N., (1974), Mater. Res. Bull., 9, 645.

[102] Palatnik, L. S., Komnik, Y. F., Belova, E. K., Adroschenko, L. V., (1961), Dokl. Akad. Nuak SSSR, 137, 68.

[103] Jumpertz, E. A., (1955), Z. Elektrochem., 59, 419.

[104] Evans, Jr., H. T., McKnight, E. T., (1959), Am. Mineral., 44, 1210.

[105] Kazinets, M. M., (1970), Kristallogratiya, 14, 704.

[106] Badachhape, S. B., Goswami, A. (1962), J. Phys. Soc. Jpn. Suppl., 17, 251.

[107] Natl. Bur. Srud (U.S.) Monogr. (1971), 25, 9, 57.

[108] Himmrich, M., Haeuseler, H. (1991), Spectrochem. Acta, 47A(7), 933.

[109] Fernandes, P. A., Salomé, P. M. P., da Cunha, A. F. (2011), "Study of polycrystalline Cu_2ZnSnS_4 films by Raman scattering." *Journal of Alloys & Compounds,* 509, pp. 7600–7606.

[110] Fernandes, P. A., Salomé, P. M. P., da Cunha, A. F. (2010), "A study of ternary $Cu_2SnS_3$and Cu_3SnS_4 thin films prepared by sulfurizing stacked metal precursors." *J. Phys. D: Appl. Phys.*, 43, 215403.

[111] Fernandes, P. A., Salomé, P. M. P., da Cunha, A. F. (2010), "Cu_xSnS_{x+1} (x = 2, 3) thin films grown by sulfurization of metallic precursors deposited by dc magnetron sputtering." *Phys. Status Solidi C,* 7(3–4), pp. 901-904.

[112] Serrano, J., Cantarero, M., Cardona, M., Garro, N., Lauck, R., Tallman, R. E., Ritter, T. M., Weinstein, B. A. (2004), "Raman scattering in β-ZnS." *Physical Review* B, 69, 014301.

[113] Munce, C. G., Parker, G. K., Holt, S. A., Hope, G. A. (2007), "A Raman spectroelectrochemical investigation of chemical bath deposited Cu_xS thin films and their modification." *Colloids and Surfaces A: Physicochem. Eng. Aspects*, 295, pp. 152–158.

[114] Parkin, I. P., Price, L. S., Hibbert , T. G., Molloy, K. C. (2001), "The first single source deposition of tin sulfide coatings on glass: aerosol-assisted chemical vapour deposition using [$Sn(SCH_2CH_2S)$]." *Journal of Materials Chemistry*, 11, pp. 1486-1490.

[115] Price, L. S., Parkin, I. P., Hardy, A., Clark, R. (1999), *Chem. Mater.*, 11, 1792.

[116] Schurr, R., Hölzing, A., Hock, R. (2010), "Real-time investigations on the formation reactions during annealing of sulfurized Cu–Sn precursors." *Thin Solid Films*, 519, pp. 7412–7415.

[117] Maeda, T., Nakamura, S., Kou, H., Wada, T., Inoue, K., Yamaguchi, Y. (2009), *Tech. Dig. PVSEC-19*, CIG-O-44.

[118] Fischereder, A., et al. (2010), "Investigation of Cu_2ZnSnS_4 Formation from Metal Salts and Thioacetamide." *Chem. Mater.*, 22, pp. 3399–3406.

[119] Bonazzi, P., Bindi, L., Bernardini, G. P., Menchetti, S. (2003), "A model for the mechansim of incorporaion of Cu, Fe and Zn in the stannite series, Cu_2FeSnS_4 – Cu_2ZnSnS_4." *The Canadian Mineralogist*, 41, pp. 639-647.

[120] Yoo, H., Kim J. H. (2010), "Growth of Cu_2ZnSnS_4 thin films using sulfurization of stacked metallic films." *Thin Solid Films*, 518, pp. 6567–6572.

[121] Weber, A., Mainz, R., Unold, T., Schorr, S., Schock, H. W. (200), "In-situ XRD on formation reactions of Cu_2ZnSnS_4 thin films." *Physica Status Solidi C*, 6, pp. 1245–1248.

[122] Hergert, F., Hock, R. (2007), "Predicted formation reactions for the solid-state syntheses of the semiconductor materials Cu_2SnX_3 and Cu_2ZnSnX_4 (X = S, Se) starting from binary chalcogenides." *Thin Solid Films*, 515, pp. 5953-5956.

[123] Smith, W. (1873), J. Soc. Telegraph Eng., 2, pp. 31.

[124] Joshi, N. V. (1990), "Photoconductivity: Art, Science and Technology." Marcel Dekker.

[125] Gorlich, P. (1967), "Photoconductivity in Solids." Dover Publications.

[126] Bube, R. (1960), "Photoconductivity of Solids." John Wiley and Sons, Inc.

[127] Bär1, M., Nishiwaki, S., Weinhardt, L., Pookpanratana, S., Shafarman, W. N., Heske, C. (2008), "Electronic level alignment at the deeply buried absorber/Mo interface in chalcopyrite-based thin film solar cells." *Appl. Phys. Lett.*, 93, 042110.

[128] Shafarman, W. N., Phillips, J. E. (1996), "Direct current-voltage measurements of the Mo/$CuInSe_2$ contact on operating solar cells." Photovoltaic Specialists Conference (PVSC), Conference Record of the Twenty-fifth IEEE, Washington, DC, USA., pp. 917-919.

[129] Moss, T. S. (1994), "Handbook of Semiconductor's." Vol. 2: Optical Properties of Semiconductors, Elsevier, Amsterdam.

[130] Franc, J. et al. (2005), "Photoconductivity spectroscopy of deep levels in CdTe." *IEEE Transactions on Nuclear Science,* 52(5).

[131] Salome, P. M. P., Malaquias, J., Fernandes P. A., da Cunha, A. F. (2010), "Mo bilayer for thin film photovoltaics revisited." J. *Phys. S: Appl. Phys*., 43, 345501.

[132] http://www.ni.com/labview/

[133] Seol, J. S., Lee, S. Y., Lee, J. .C, Nam, H. D., Kim, K. H. (2003), "Electrical and Optical Properties of Cu_2ZnSnS_4Thin Films Prepared by RF Magnetron Sputtering Process." *Solar Energy Materials & Solar Cells*, 75, pp. 155–162.

[134] Moriya, K., Tanaka, K., Uchiki, H. (2005), "Characterization of Cu_2ZnSnS_4 Thin Films Prepared by Photo-Chemical Deposition." J*apanese Journal of Applied Physics*, 44, pp. 715-717.

[135] Chen, S., Gong, X. G., Walsh, A., Wei, S. H. (2010), "Defect physics of the kesterite thin-film solar cell absorber Cu_2ZnSnS_4." *Applied Physics Letters,* 96, 021902.

[136] Golan, G., Axelevitch, A., Gorenstein, B., Manevych, V. (2006), "Hot-Probe method for evaluation of impurities concentration in semiconductors." *Microelectronics Journal,* 37, pp. 910-915.

[137] Van Zeghbroeck, B. (2008), "Principle of Semiconductor Devices." Prentice Hall, Englewood Cliffs, NJ.

A Appendix

A.1 Precursor stack order: Cu/Zn/Sn

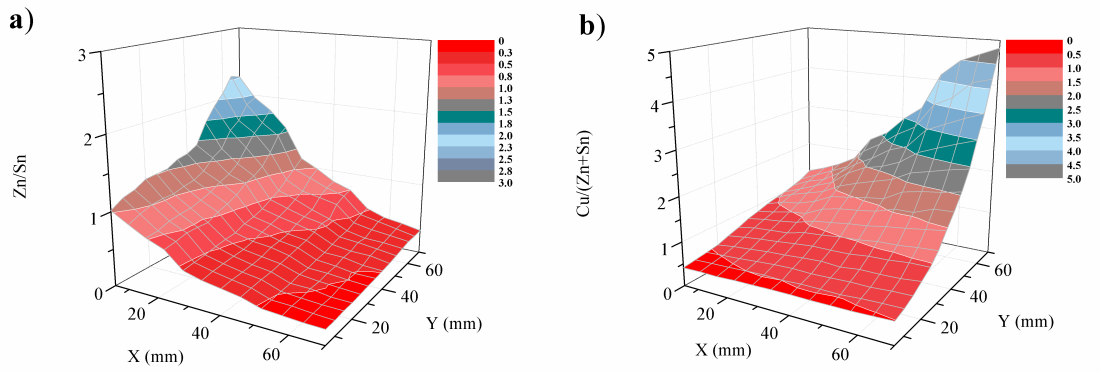

Figure 63: **Elemental ratio contour plots for sequential stacking order Cu/Zn/Sn as a function of position: a) Zn/Sn and b) Cu/(Zn+Sn).**

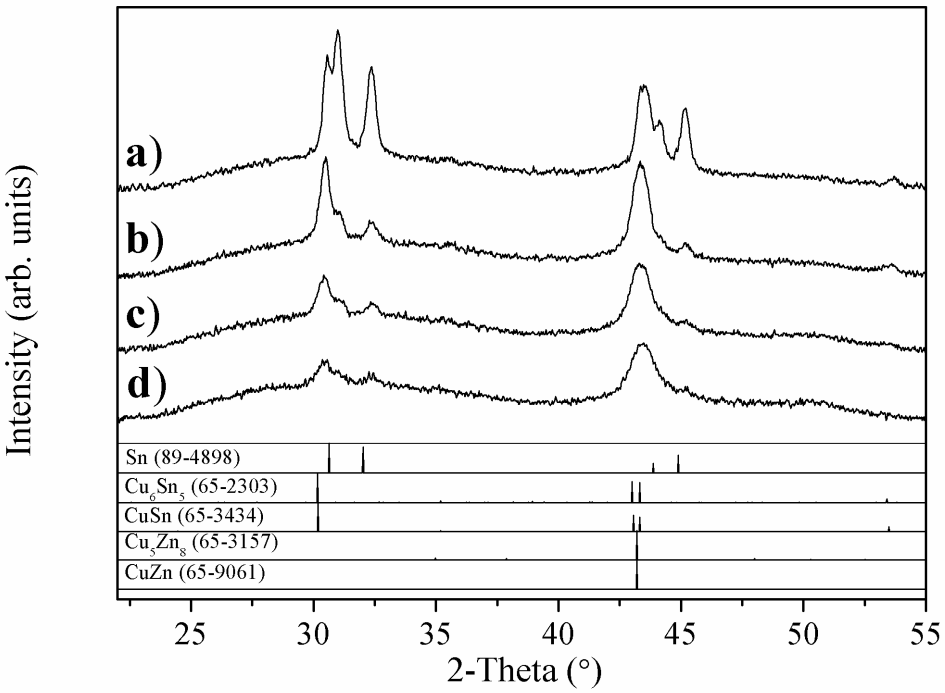

Figure 64: **Diffractograms of stacked (Cu/Zn/Sn) precursor metals indicating the evolution in crystalline phases with respect to selected composition ratios Zn/Sn and Cu/(Zn+Sn) across the library.**

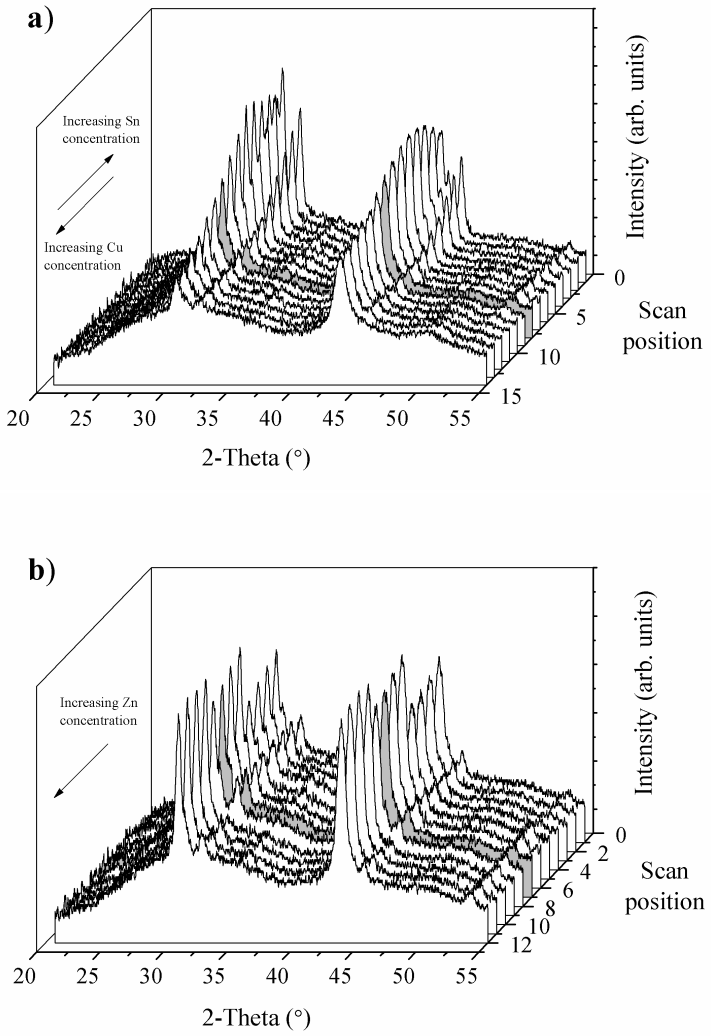

Figure 65: **Diffractograms with respect to two scan positions across the multilayer Cu/Zn/Sn sample. a) Change of Cu and Sn composition and, b) change of Zn concentration. Shaded region indicates stoichiometric point (centre of library).**

A.1.1 Sulphurised stack order: Cu/Zn/Sn

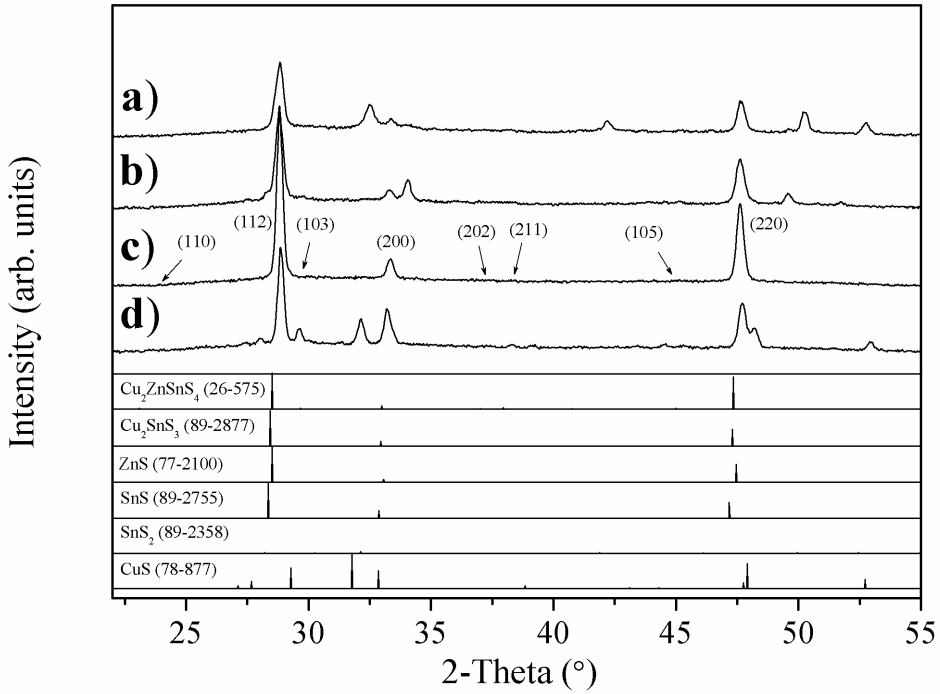

Figure 66: **Diffractograms of sulphurised precursor metals with stacking order Cu/Zn/Sn at 500 °C indicating the evolution of crystalline phases with respect to selected composition ratios Zn/Sn and Cu/(Zn+Sn).**

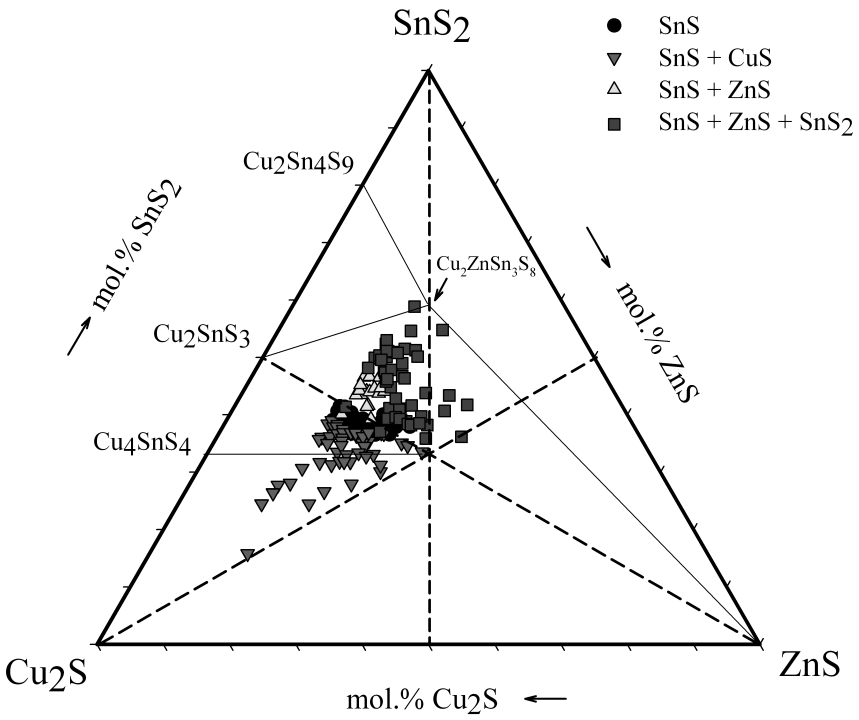

Figure 67: **Sulphurised phase-composition plot for the Cu/Zn/Sn stacking order superimposed onto the quasi-ternary Cu_2S-ZnS-SnS_2 (400 °C) equilibrium phase diagram [91]. Intersection of the dashed lines denotes the stoichiometric precursor ratio (Cu:Zn:Sn =2:1:1).**

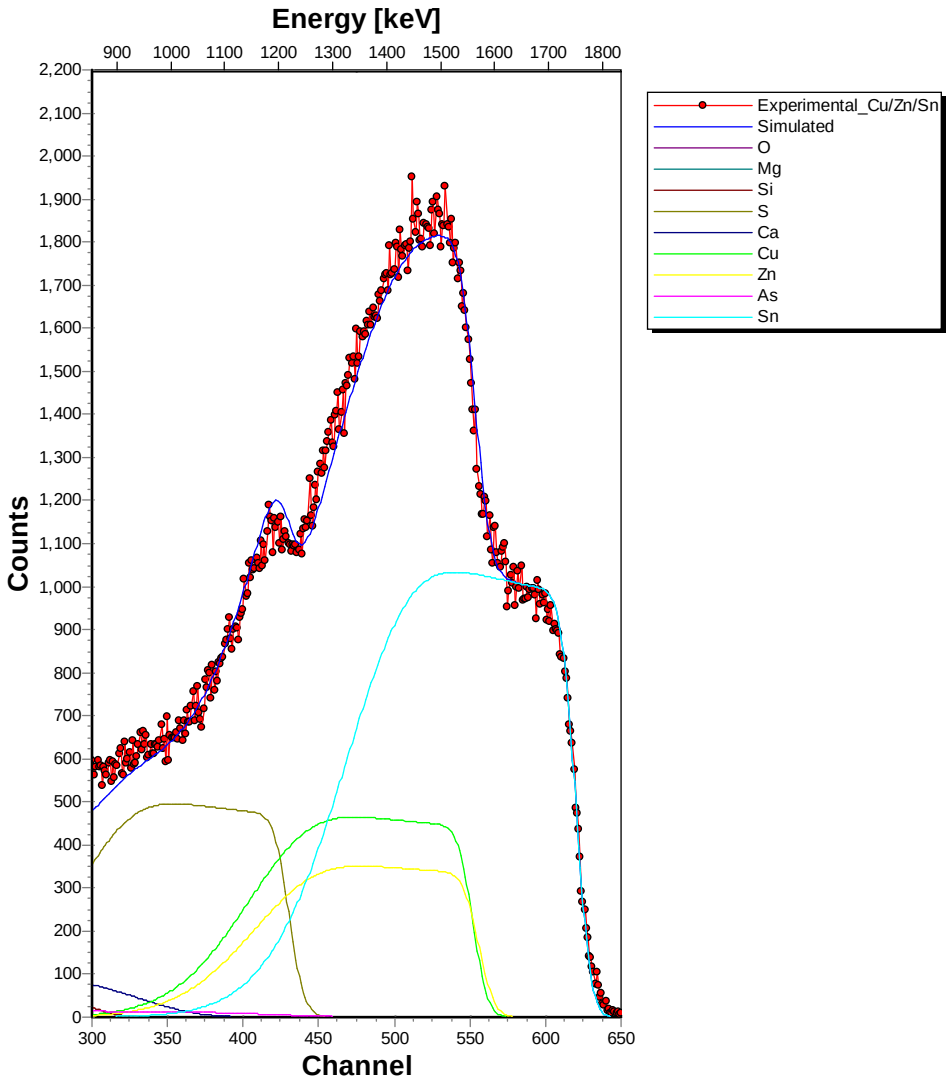

Figure 68: **RBS spectrum of a Cu/Zn/Sn stacked near-stoichiometric CZTS layer onto glass. The sample structure and the thicknesses of the layers (in atoms/cm 2) are also shown schematically.**

A.2 Precursor stack order: Zn/Sn/Cu

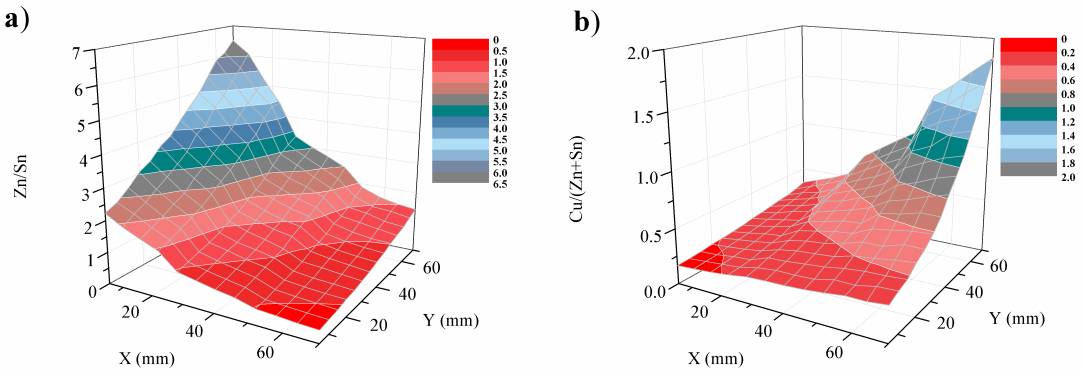

Figure 69: **Elemental ratio contour plots for sequential stacking order Zn/Sn/Cu as a function of position: a) Zn/Sn and b) Cu/(Zn+Sn).**

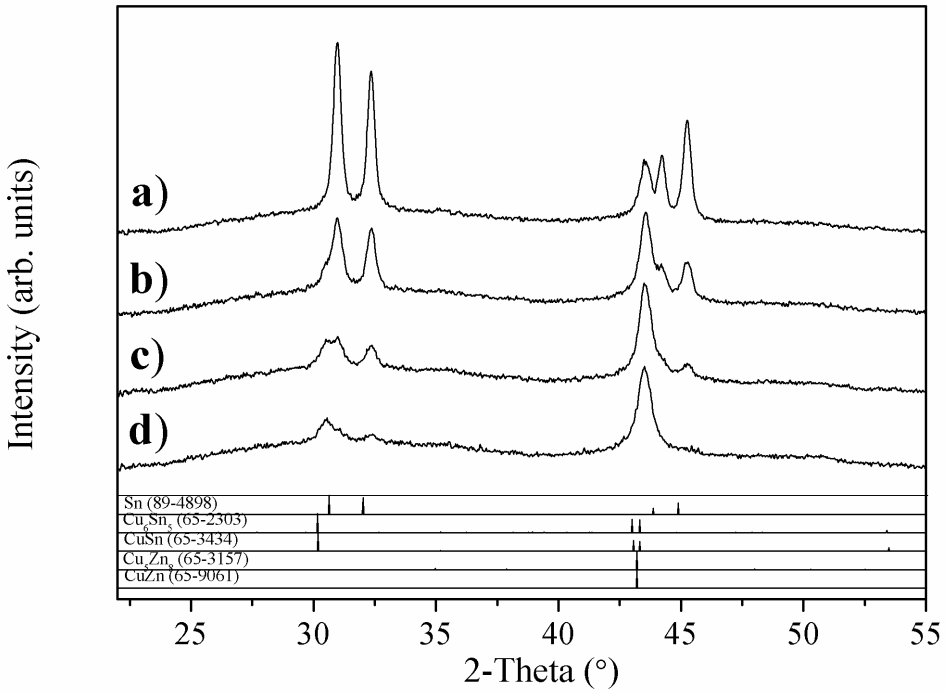

Figure 70: **Diffractograms of stacked Zn/Sn/Cu precursor metals indicating the evolution in crystalline phases with respect to selected composition ratios Zn/Sn and Cu/(Zn+Sn) across the library.**

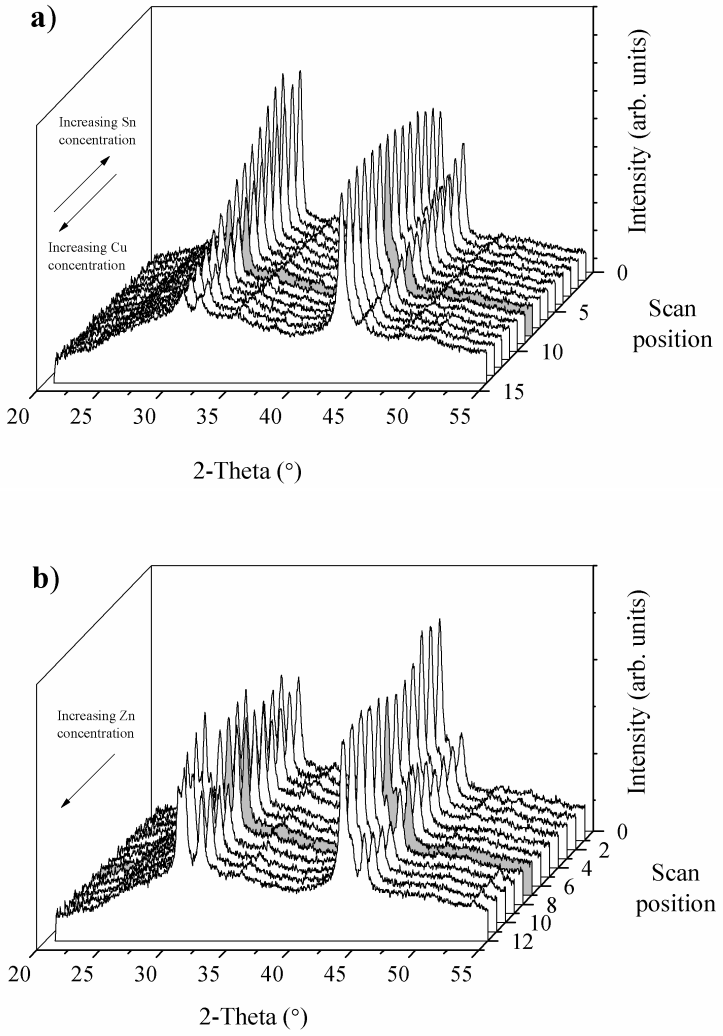

Figure 71: **Diffractograms with respect to two scan positions across the multilayer Zn/Sn/Cu sample. a) Change of Cu and Sn composition and, b) change of Zn concentration. Shaded region indicates stoichiometric point (centre of library).**

A.2.1 Sulphurised stack order: Zn/Sn/Cu

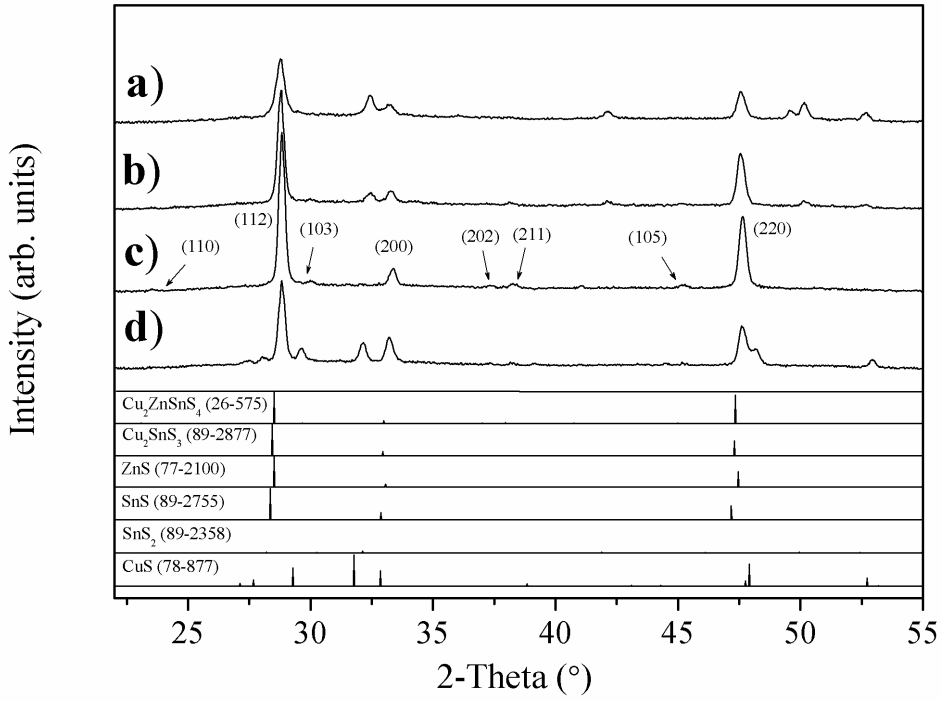

Figure 72: **Diffractograms of sulphurised precursor metals with stacking order Zn/Sn/Cu at 500 °C indicating the evolution of crystalline phases with respect to selected composition ratios Zn/Sn and Cu/(Zn+Sn).**

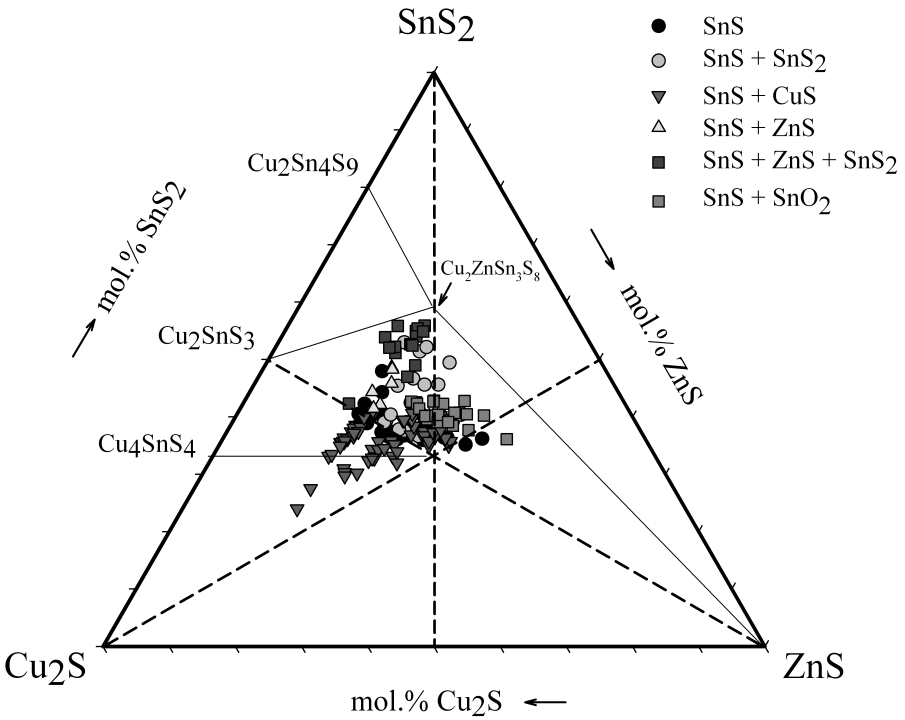

Figure 73: **Sulphurised phase-composition plot for the Zn/Sn/Cu stacking order superimposed onto the quasi-ternary Cu_2S-ZnS-SnS_2 (400 °C) equilibrium phase diagram [91]. Intersection of the dashed lines denotes the stoichiometric precursor ratio (Cu:Zn:Sn =2:1:1).**

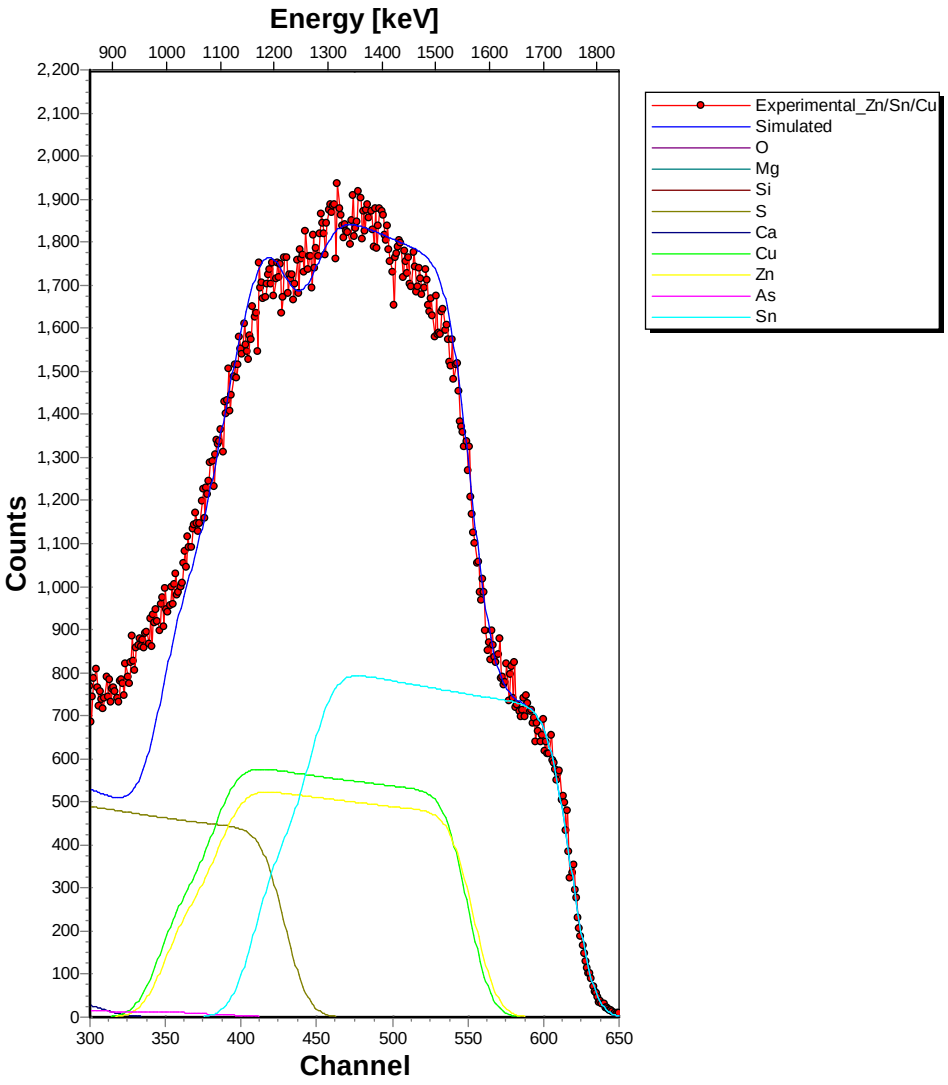

Figure 74: **RBS spectrum of a Zn/Sn/Cu stacked near-stoichiometric CZTS layer onto glass. The sample structure and the thicknesses of the layers (in atoms/cm ^{2}) are also shown schematically.**

A.3 Molybdenum sputtering calibration data

Deposition parameters for the Mo ohmic contacts required for photoconductivity measurements are obtained from the following calibration data.

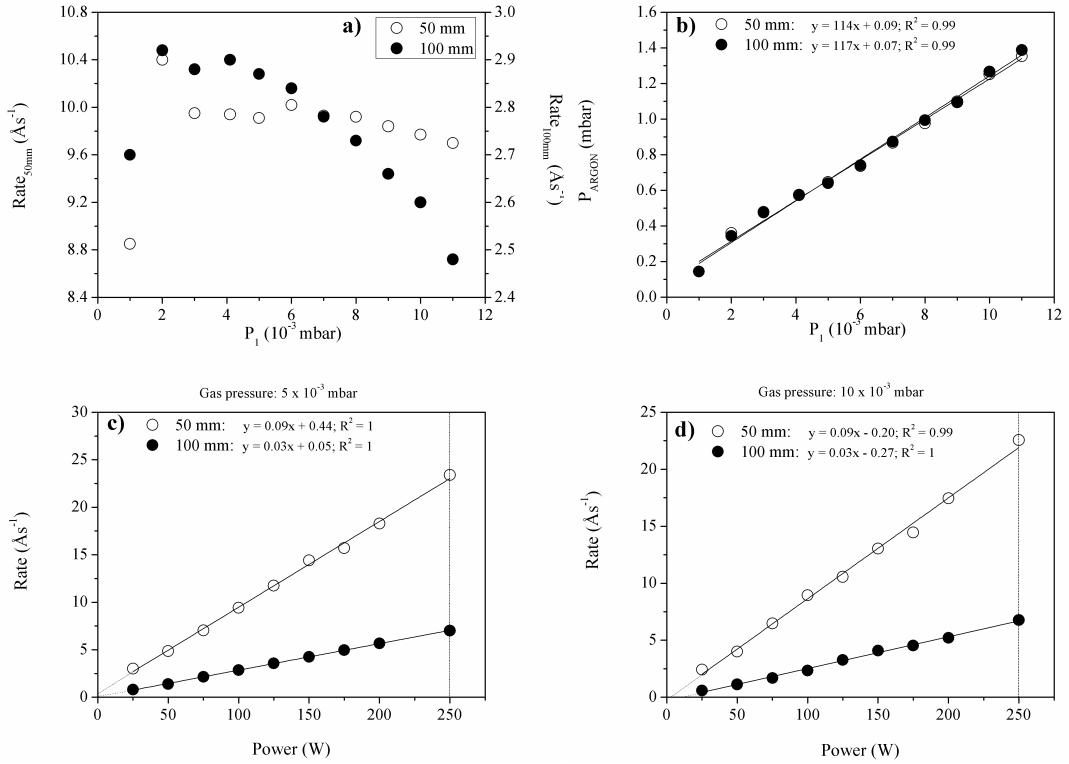

Figure 75: **Calibration data for the molybdenum sputter target as a function of target-substrate distance: a) operating chamber pressure P_1 against sputter rate; b) correlation between operating pressure P_1 and argon working gas P_{argon} and, c) Power versus sputter rate.**